STUDIES ON INTERACTION OF ELECTROMAGNETIC WAVES WITH BARIUM
HEXAFERRITE CERAMICS

A THESIS SUBMITTED TO
THE GRADUATE SCHOOL OF NATURAL AND APPLIED SCIENCES
OF
MIDDLE EAST TECHNICAL UNIVERSITY

BY

NURDAN GÜRKAN

IN PARTIAL FULFILLMENT OF THE REQUIREMENTS
FOR
THE DEGREE OF MASTER OF SCIENCE
IN
METALLURGICAL AND MATERIALS ENGINEERING

JUNE 2008

Approval of the thesis:

STUDIES ON INTERACTION OF ELECTROMAGNETIC WAVES WITH BARIUM HEXAFERRITE CERAMICS

submitted by **NURDAN GÜRKAN** in partial fulfillment of the requirements for the degree of **Master of Science in Metallurgical and Materials Engineering Department, Middle East Technical University** by,

Prof. Dr. Canan Özgen   _____
Dean, Graduate School of **Natural and Applied Sciences**

Prof. Dr. Tayfur Öztürk   _____
Head of Department, **Metallurgical and Materials Engineering**

Prof. Dr. Muharrem Timuçin   _____
Supervisor, **Metallurgical and Materials Engineering Dept., METU**

Assoc. Prof. Dr. Özlem Aydın Çivi   _____
Co-Supervisor, **Electrical and Electronics Engineering Dept., METU**

Examining Committee Members:

Prof. Dr. Macit Özenbaş   _____
Metallurgical and Materials Engineering Dept., METU

Prof. Dr. Muharrem Timuçin   _____
Metallurgical and Materials Engineering Dept., METU

Prof. Dr. Abdullah Öztürk   _____
Metallurgical and Materials Engineering Dept., METU

Assist. Prof. Dr. Arcan Fehmi Dericioğlu   _____
Metallurgical and Materials Engineering Dept., METU

Dr. İbrahim Çam   _____
Central Lab., METU

Date: 24.06.2008

I hereby declare that all information in this document has been obtained and presented in accordance with academic rules and ethical conduct. I also declare that, as required by these rules and conduct, I have fully cited and referenced all material and results that are not original to this work.

Name, Last name: Nurdan GÜRKAN

Signature   :

ABSTRACT

STUDIES ON INTERACTION OF ELECTROMAGNETIC WAVES WITH BARIUM
HEXAFERRITE CERAMICS

Gürkan, Nurdan

M.S., Department of Metallurgical and Materials Engineering

Supervisor   : Prof. Dr. Muharrem Timuçin

Co-Supervisor : Assoc. Prof. Dr. Özlem Aydın Çivi

June 2008, 103 Pages

M-type barium hexaferrite powders doped with titanium and/or cobalt have been synthesized according to the stochiometric formulations $BaFe_{(12 - (4/3)x)}Ti_xO_{19}$, $BaFe_{12-x}Co_xO_{19}$, $BaFe_{12-2x}Ti_xCo_xO_{19}$ (x varying from 0 to 1.5 with an increment of 0.5) by the mixed oxide approach. The powders were used to manufacture small ceramic tiles by sintering each composition at 1250 °C with soaking times ranging from 1 to 16 hours. XRD work revealed formation of the magnetoplumbite crystal structure in all ceramics. The variations in processing parameters led to differences in microstructure and various dielectric and magnetic properties of the ceramic tiles. The interaction of the ceramics with electromagnetic waves was characterized by using a vector network analyzer in the X and Ku bands. The results revealed that, undoped barium hexaferrite ceramics and those doped with low titanium exhibited good microwave absorption properties.

ÖZ

ELEKTROMANYETİK DALGALARIN BARYUM HEGZAFERRİT SERAMİKLERLE
ETKİLEŞİMİ

Gürkan, Nurdan

Yüksek Lisans, Metalurji ve Malzeme Mühendisliği Bölümü

Tez Yöneticisi   : Prof. Dr. Muharrem Timuçin

Ortak Tez Yöneticisi : Doç. Dr. Özlem Aydın Çivi

Haziran 2008, 103 Sayfa

Titanyum ve/veya kobalt ile katkılandırılmış M-tipi baryum hegzaferrit tozları, $BaFe_{(12-(4/3)x)}Ti_xO_{19}$, $BaFe_{12-x}Co_xO_{19}$, $BaFe_{12-2x}Ti_xCo_xO_{19}$ (x = 0'dan x = 1.5'e kadar 0.5'lik aralıklarla değiştirilmiştir) stokiyometrik formulasyonlarına göre oksit karışımı metodu ile sentezlenmiştir. Bu tozlar, her bir kompozisyon 1250 ^{o}C'de 1'den 16 saate kadar değişen pişirme süreleriyle sinterlenerek küçük seramik karoların üretiminde kullanılmıştır. X ışınları kırınım analizleri, magnetoplumbit kristal yapısının bütün seramiklerde oluştuğunu göstermiştir. Üretim parametrelerindeki değişim seramik karoların iç yapısındaki farklılıklara ve değişik dielektrik ve manyetik özelliklere neden olmuştur. Seramiklerin elektromanyetik dalgalarla etkileşimi vektör ağ analiz sistemi kullanılarak X ve Ku bandlarında karakterize edilmiştir. Sonuçlar katkılandırılmamış baryum hegzaferrit ve düşük titanyum ile katkılandırılmış seramiklerin iyi mikrodalga soğurma özellikleri sergilediğini göstermiştir.

Anahtar Kelimeler: Baryum Hegzaferrit, Ti ve/veya Co Katkılandırılması, Radar Soğurucu Malzeme, Dalga Kılavuzu, X ve Ku Bandları.

To My Fiancé
and
To My Family

ACKNOWLEDGMENTS

TABLE OF CONTENTS

LIST OF TABLES

LIST OF FIGURES

xiv

CHAPTER 1

INTRODUCTION

1.1 General Information

Modern living environment is dominated by electromagnetic (EM) waves. Quite a large number of electronic equipment around and the communication devices place human beings literally in a jungle of EM waves. The frequency spectrum of EM waves is shown by the chart in Figure 1. The wide frequency range extending to 10^{24} Hz is divided into several subregions due to the differences in their physical properties. The chart includes both the old and the new designations of the frequency bands encountered in EM nomenclature.
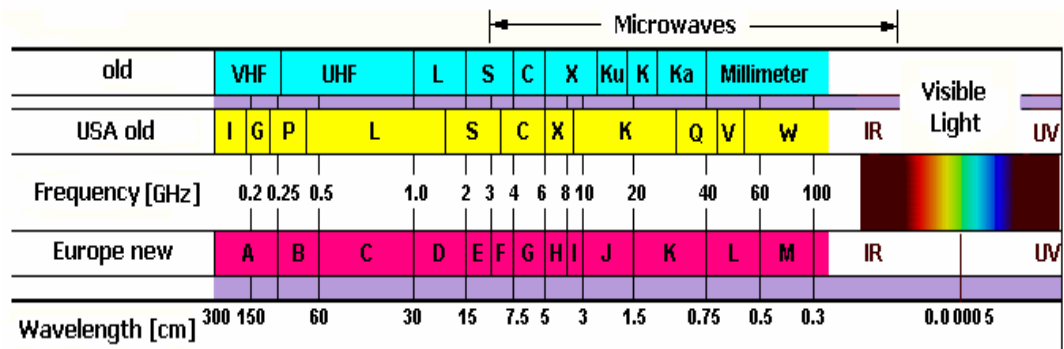
Figure 1 Frequency range and different bands of electromagnetic waves.

The main uses for different bands of EM waves are given in Table 1. Starting from the low frequency bands, the principal uses include communications, navigation, surveillance, direction finding, and tracking of objects [1]. The present thesis study is concerned with the frequency bands designated as X and Ku which extend from 5 GHz (gigahertz) to 18 GHz. This particular region is part of the "Superhigh

Frequency" range and represents the radar waves used in the detection of airborne vehicles.

Table 1 Definition and application areas of the frequency bands [1].

Frequency Band	Definition	Application Areas
3-30 KHz	Very Low Frequency (VLF)	Navigation, sonar, sound waves
30-300 KHz	Low Frequency (LF)	Direction finding with radio waves, Surveillance with radio
300-3000 KHz	Medium Frequency (MF)	AM radio, Direction finding
3-30 MHz	High Frequency (HF)	Telephone, Fax, Short wave radio
30-300 MHz	Very High Frequency (VHF)	FM Radio, TV, Air traffic control, Mobile phones
300-3000 MHz	Ultrahigh Frequency (UHF)	TV, Satellite communication, Wireless data, Microwave owen
3-30 GHz	Superhigh Frequency (SHF)	Airplane radars, Satellite communication
30-300 GHz	Extreme High Frequency (EHF)	Radar, Space exploration

The acronym radar, which stands for "radio detection and ranging", designates the equipment or facility for detecting distant objects using EM waves. The microwave radars were introduced during World War II and since then they have become overwhelming threat to aircrafts due to the fact that they can detect airborne targets independent of weather [2]. The effectiveness of a radar system depends primarily on how much of the EM energy is reflected from the target back to the radar [3]. The parameter of importance which describes the visibility of an aircraft to radar is called as radar cross section (RCS). Techniques developed for making the detection of the aircraft to radar harder are known as the stealth technology.

The stealth technology is based on the use of coatings, which interact with radar and minimize the reflection of the incident EM wave. Earliest forms of such coatings were developed by Germans in World War II to lower the reflectivity of the submarine periscopes so as to evade them from 20-cm radar band the Allies used [4]. The coating interacted with the radar by absorption of the incident energy. Because of their mode of protection, it has become customary to call such coatings as Radar Absorbing Materials, or RAMs.

In principle, the interaction of an EM wave with a material target can be described by the simple diagram as shown in Figure 2.
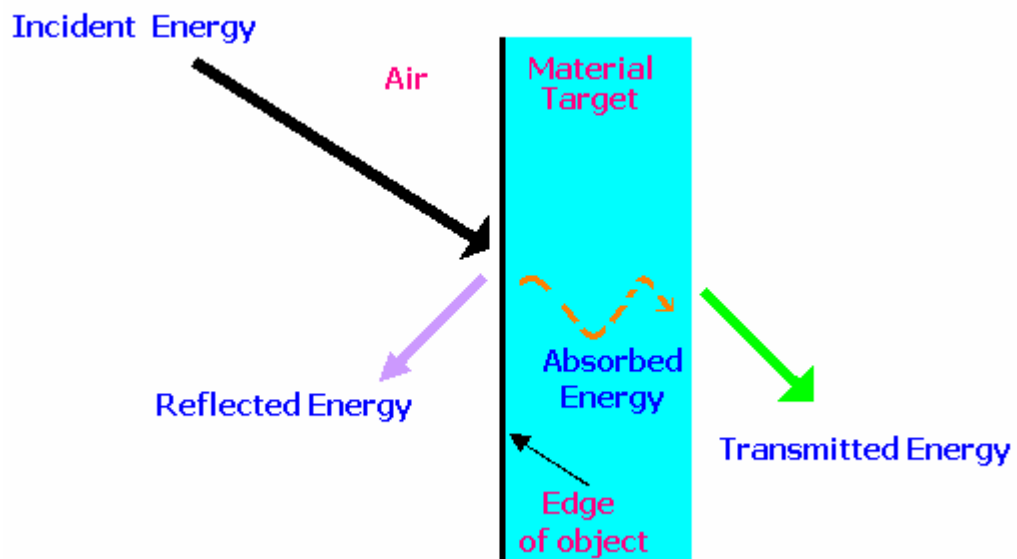
Figure 2 Interaction of a material with EM wave.

The effectiveness of radar evasion depends on how much of the EM energy is absorbed by the RAM, that is by the degree of reduction achieved in RCS due to the use of RAM. EM characteristics of the coating material, its thickness, weight, and environmental stability are among the important factors to be considered in designs based on enhancing the EM absorption of the coating [5].

Starting from 1980's RAMs based on barium hexaferrite have become fashionable due to the ease of their application and the flexibility in their microwave absorption properties. The chemical constitution of barium hexaferrite is represented by the molecular formula $BaO.6Fe_2O_3$. This compound, which can be synthesized by conventional powder processing techniques of ceramic technology, is used quite widely as a hard permanent magnet.

The EM characteristics which play dominant role on the design of RAM include magnetic and dielectric properties of the material. The generally accepted parameter which governs the interaction of RAM with EM wave is the matching impedance Z_m of the coating as defined by [6, 7]:

$$Z_m = \sqrt{\frac{\mu_r}{\varepsilon_r}} = \sqrt{\frac{\mu'_r}{\varepsilon'_r}} \sqrt{\frac{1 + j\tan\delta_\varepsilon - j\tan\delta_\mu + \tan\delta_\varepsilon \tan\delta_\mu}{1 + \tan^2\delta_\varepsilon}} \tag{1.1}$$

Various terms in the above equation are defined as follows:

$$\mu = \mu_r \mu_0 = \left(\mu'_r - j\mu''_r\right)\mu_0 \tag{1.2}$$

$$\varepsilon = \varepsilon_r \varepsilon_0 = \left(\varepsilon'_r - j\varepsilon''_r\right)\varepsilon_0 \tag{1.3}$$

$$\tan\delta_\mu = \frac{\mu''_r}{\mu'_r} \tag{1.4}$$

$$\tan\delta_\varepsilon = \frac{\varepsilon''_r}{\varepsilon'_r} \tag{1.5}$$

where,

μ : magnetic permeability

μ_r : relative magnetic permeability

μ'_r : real part of complex magnetic permeability

μ''_r : imaginary part of complex magnetic permeability

μ_0 : magnetic permeability of free space

ε : dielectric permittivity

ε_r : relative dielectric permittivity

ε'_r : real part of complex dielectric permittivity

ε''_r : imaginary part of complex dielectric permittivity

ε_0 : dielectric permittivity of free space

$\tan\delta_\mu$: magnetic loss tangent

$\tan\delta_\varepsilon$: dielectric loss tangent

An ideal absorber may have a single and thin layer of material having numerically equal values of complex permeability and permittivity and high tangent losses [8]. The former guarentees efficient matching of the incident wave into absorber, and the latter promotes rapid attenuation thereafter [8]. The attenuation paramater called as attenuation constant, α, in nepers per length is defined by the following expression [9]:

$$\alpha = \frac{\pi\sqrt{2\delta'_r}}{\lambda_0}\sqrt{\sqrt{1+\tan^2\delta}-1} \tag{1.6}$$

where, λ_0 is free space wavelength at frequency of operation and,

$$\delta'_r = \mu'_r\varepsilon'_r - \mu''_r\varepsilon''_r \tag{1.7}$$

$$\delta''_r = \mu'_r\varepsilon''_r + \mu''_r\varepsilon'_r \tag{1.8}$$

$$\tan\delta = \frac{\delta''_r}{\delta'_r} \tag{1.9}$$

Another important parameter for designing an absorber is the thickness criterion. Knott [10] stated that although a radar absorbent material has been classically regarded as a quarter-wavelength thick, if the material is dominantly magnetic in character, the required thickness for minimum reflection may even exceed a half-wavelength. Moreover, it was reported that, no general design rules and formula

5

for the optimum EM parameters and matching thickness of the absorbing materials seem to be available [11].

Barium hexaferrite, BaHF, derives its RAM properties from its lossy characteristics; in other words it exhibits high dielectric and magnetic losses in microwave frequency range which make it special for radar absorption [12]. BaHF has uniaxial anisotropy. Therefore, when BaHF is processed as a ceramic or a composite under a strong magnetic field, all grains may be oriented regularly along the c-axis [13]. Due to its high anisotropy field, BaHF can be used at much higher frequencies than spinel ferrites or garnets [14].

The major problem in the microwave absorption is that a given RAM may absorb energy only in a narrow frequency band. In case of BaHFs, however, microwave absorption band may be widened when multilayer structures are generated by combining hexaferrites having different resonant frequencies in a composite structure [13]. In this regard, substitution for the Fe^{3+} or Ba^{2+} site, which can make the material magnetically softer [15], has become a widely used method to vary the radar absorption properties of BaHF. Numerous studies were carried out dealing with the substitution of Fe^{3+} or Ba^{2+} site using replacement couples such as Al-Cr [13, 16, 17], Zn-Ti [18], Mn-Ti [19, 20] Ti-Co [21, 22], Ir-Co [23] and La-Na [24].

The ferric ions in the BaHF can be replaced partially either by Co^{2+} or by Ti^{4+}, or both. Such replacements are considered to change the magnetic anisotropy of undoped BaHF from uniaxial to planar [22]. Moreover, Amin and James [6, 7] showed that, complex dielectric permittivity and complex magnetic permeability of BaHF could be changed by titanium and cobalt replacements. However, they did not disclose the compositions of the ferrites on the curves displaying their data on reflection loss and magnetic permeability as a function of frequency. In addition, they did not provide any explanation on the specific effects of cobalt and titanium substitutions in BaHF.

A large number of earlier studies conducted on the effect of modifications upon microwave absorption properties of substituted BaHF were carried out on

composites made by dispersing the ferrite powders in an insulating matrix [14, 20, 24-27]. The specific interest was placed in investigating the effects of the volume percentage of the ferrite in the composite on absorption properties [12]. It appears that, in the existing literature, no efforts were made to establish correlations between the microwave absorption properties and the processing parameters of BaHF as a bulk ceramic, although tiles of these are available in the market.

Present study was undertaken with the aim of generating information on the interaction of bulk BaHF ceramics with EM waves within a frequency range lying in the X and Ku bands. The data were obtained by a network analyzer with the help of rectangular waveguides. Moreover, the bulk BaHF ceramics modified by Ti and/or Co doping were studied to determine the effects of chemical modifications on absorption properties. The ceramics were manufactured in the form of small tiles and machined to the size compatible with the dimensions of the waveguide. The ceramic tiles were produced as isotropic materials. No special effort was spent to induce anisotropy since textured ceramics will be the subject of a further study.

CHAPTER 2

LITERATURE REVIEW

This chapter contains information on the origin of magnetism and the response of ferrite ceramics to external magnetic fields with reference to microwave absorption.

2.1   Origins of Magnetic Moments

Magnetic fields are produced by moving electrical charges. Ampére, Biot, Savart and Oersted were among the first to prove that conductors carrying currents produced magnetic fields and exerted 'Lorentz' forces in each other [28]. This Lorentz force $\vec{F}$ is related according to:

$$\vec{F} = q\left(\vec{E} + \vec{\upsilon} \times \vec{B}\right) \tag{2.1}$$

where $\vec{\upsilon}$ is defined as the velocity of a moving charge q in a magnetic induction $\vec{B}$ and in an electric field $\vec{E}$.

Both orbital and spin motions of the electrons cause magnetic moment $\vec{\mu_m}$. Ampére suggested that the origin of the magnetic effect in materials lies in small circulating currents associated with each atom [28]. Thus, if e is the charge on the electron, c the velocity of light, h Planck's constant, and m mass of the electron, the orbit and spin magnetic moments of electrons can be expressed by [29]:

$$\mu_{(orbit)} = n \cdot \left(\frac{e \cdot h}{4 \cdot \pi \cdot m \cdot c}\right) \tag{2.2}$$

8

$$\mu_{(spin)} = \frac{e \cdot h}{4 \cdot \pi \cdot m \cdot c} = 0.927 \times 10^{-20} \text{ erg} \Big/ \text{Oe} \qquad (2.3)$$

where $\mu_{(orbit)}$ is the magnetic moment in the nth Bohr orbit, and $\mu_{(spin)}$ represents the magnetic moment due to the spinning.

From Equation (2.2) and Equation (2.3); it can be observed that magnetic moment due to spin is equal to that due to orbital motion for electrons in the first orbital where n=1. This particular quantity of magnetic moment is defined as Bohr magneton, μ_B; which equals to $0.927 \times 10^{-20} erg \cdot Oe^{-1}$. The total magnetic moment of an atom is the vector sum of all its electronic spin and orbital moments [29].

There is a relationship between magnetic dipole moment μ_m and the angular momentum L for a moving particle of mass m and the charge Q as follows [28]:

$$\mu_m = \gamma \cdot L \qquad (2.4)$$

in which $\gamma = Q/2m$ is the gyromagnetic ratio.

2.2   Magnetization from the Macroscopic Viewpoint

Magnetic induction, or magnetic flux density, $\vec{B}$, and magnetic field intensity, or magnetic field strength, designated as $\vec{H}$ are related for a linear, isotropic and homogeneous medium by means of the following expression:

$$\vec{B} = \mu \vec{H} \qquad (2.5)$$

where μ is the magnetic permeability of the medium. In vacuum, expression in Equation (2.5) changes to:

$$\vec{B}_0 = \mu_0 \vec{H} \qquad (2.6)$$

9

where μ_0 is the permeability of a vacuum having a value of $4\pi \times 10^{-7}$ H/m and $\vec{B}_0$ represents the flux density within vacuum.

Magnetic parameters of the solids may be described with several parameters. One of these parameters is the ratio of the permeability in a material to the permeability in vacuum, thus;

$$\mu_r = \frac{\mu}{\mu_0} \tag{2.7}$$

where μ_r is defined as the relative magnetic permeability, and is unitless.

Another field quantity is the magnetization $\vec{M}$ which is the ratio of the magnetic moment to the unit volume, and it is defined by the following expression [30]:

$$\vec{B} = \mu_0 \vec{H} + \mu_o \vec{M} \tag{2.8}$$

The magnetic moments within a material tend to become alligned with the applied field $\vec{H}$ and the term $\mu_0 \vec{M}$ is a measure of the reinforcement brought by the material upon the magnetic field [30]. Moreover, the magnitude of the magnetization is related to the applied field as follows [31]:

$$\vec{M} = \chi_m \vec{H} \tag{2.9}$$

here χ_m is called magnetic susceptibility which is related also with the relative permeability according to the following expression:

$$\chi_m = \mu_r - 1 \tag{2.10}$$

It is important to emphasize that there is a dielectric analogue for each of the magnetic field parameters. The $\vec{B}$ and $\vec{H}$ fields are analogous to the dielectric

displacement $\vec{D}$ and electric field $\vec{E}$, respectively.The permeability μ correlates with the permittivity ε, and magnetization $\vec{M}$ parallels polarization $\vec{P}$.

2.3   Classification of Magnetic Materials

Magnetic materials are classified broadly on the basis of the atomic structure of the material as well as the sign and magnitude of magnetic susceptibility.

Diamagnetism is a very weak form of magnetism. Most materials are diamagmetic and they have very small negative susceptibilities. In these instances, there need be no permanent dipoles present. When a magnetic field is applied to a diamagnetic material, small net magnetization is induced in a sense opposing the magnetic field. This phenomenon is really the most natural of magnetism and it can be observed only when other types of magnetism are totally absent. Figure 3 represents the atomic dipole configuration in a diamagnetic substance.
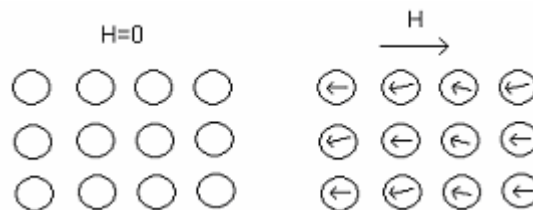
Figure 3 The atomic magnetic dipole configurations for a diamagnetic material
         with and without applied field [30].

In some solid materials, in the absence of an applied magnetic field, the orientations of the magnetic moments are random and the material possesses no net macroscopic magnetization. When an external field is applied, atomic magnetic moments preferentially align by rotation which results in paramagnetism. Susceptibility values for paramagnetic materials are relatively small but positive. Figure 4 illustrates the atomic magnetic configuration for a paramagnetic material with and without an external field.

Figure 4 The atomic dipole configuration for a paramagnetic material with or without a magnetic field [30].

In certain metallic materials, so-called ferromagnetic materials, magnetization is spontaneous below a certain critical temperature, known as Curie temperature T_c. In the absence of an external field; magnetic moments are also present as in the paramagnetic materials. The difference being, however, that the spins of neighboring ions are already more or less parallel, that is, the spontaneous magnetization is not apparent in ferromagnetic materials without an applied external field due to the formation of small volumes, named as domains. The atomic dipole configuration for a ferromagnetic material in the absence of a magnetic field is shown in Figure 5. When an external field is applied, the magnetic dipoles are mutually aligned with the applied field. By the removal of the applied field, some part of the induced domain alignment remains so that the material can be called as a real 'magnet' in this case. Moreover, these materials follow the B-H hysteresis over magnetization cycle below T_c as shown in Figure 6.
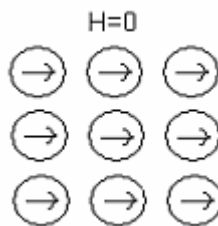
Figure 5 The atomic dipole configuration for a ferromagnetic material in the absence of a magnetic field [30].
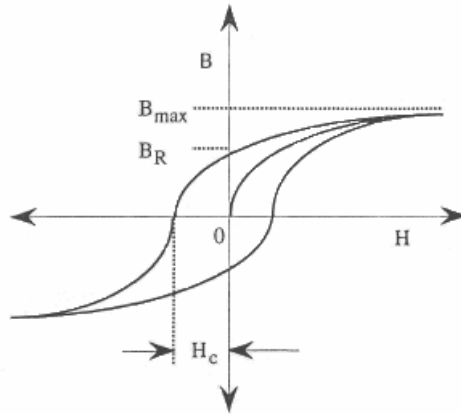
Figure 6 Magnetic flux density versus the magnetic field strength for a ferromagnetic material.

Hysteresis behavior can be explained by the motion of the domain walls as shown in Figure 7. Upon reversal of the magnetic field direction from B_{max}, known also as saturation point, the process by which the domain structure changes is reversed. It starts by the rotation of the single domain with the reversed field. Next, magnetic moments of the domains align with the applied field and grow at the expense of the former grains. When the applied field becomes zero, there is still alignment of the domains in the former direction, explained by the remanence, B_r. To reduce the magnetic flux density to zero, an H field of magnitude $-H_c$, called coercivity or coercive force, must be applied in the opposite direction of the incident field.
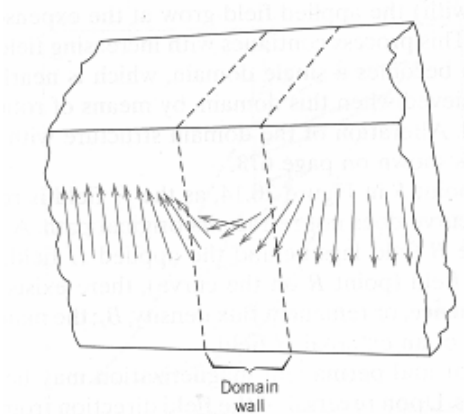
Figure 7 Change in atomic-dipole orientation through a domain wall [32].

A comparison of the diamagnetic, paramagnetic and ferromagnetic materials according to their susceptibility and permeability values as well as their magnetic spin alignment is given in Table 2.

Table 2 The comparison of the diamagnetic, paramagnetic and ferromagnetic materials [31].

Properties	Diamagnetic	Paramagnetic	Ferromagnetic
Susceptibility	Small and negative	Small and positive	Large and positive
Permeability	<1	>1	>>>1
Magnetic spin alignment	opposite	Spins too far apart	Same direction
Examples	Cu, He	Na, Al	Fe, Co, Ni

In antiferromagnetic materials, below a temperature known as the Néel point, the uncompensated electron spins associated with neighboring cations orient themselves in such a way that the overall magnetization becomes zero. Their susceptibilities are small and positive. Above Néel point, these materials behave as paramagnetic materials. Figure 8 shows the schematic illustration of the spin magnetic moments for an antiferromagnetic material.
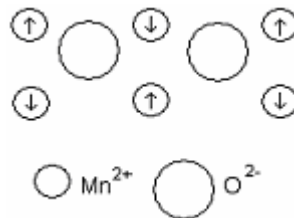
Figure 8 Schematic illustration of spin magnetic moments for antiferromagnetic manganese oxide [30].

Finally, some ceramics exhibit a permanent magnetization, defined as ferrimagnetism. Ferromagnets and ferrimagnets are similar in the macroscopic characteristics; the distinction is due to the source of the magnetic moments. In ferrimagnets, there is antiferromagnetic coupling between cations occupying crystallographically different sites, and the magnetization of one lattice is antiparallel to another sublattice. Since the two magnetizations are of unequal strength there is a net spontaneous magnetization which disappears at $T > T_c$ due to energy forcing individual magnetic moments [31]. "Ferrites" are known to be the major class of the ferrimagnetic materials and they are described in detail in the following section.

2.4 Ferrites

Ferrite ceramics are mixed crystals of various metallic oxides and may be considered to consist of oxygen ions in a closed-packed structure with cations filling the interstices.

Ferrites with a high coercivity are called hard ferrites, whereas those with an easy magnetization and low coercivity are called soft ferrites. The boundary in coercive field values with respect to these two cases is somewhere between 1 kA/m ($H_c \leq 1$ kA/m –soft ferrites) and 10 kA/m ($H_c \geq 10$ kA/m -hard ferrites). In ferrites the highest coercivity belongs to $BaFe_{12}O_{19}$ with a value of 420 kA/m [33].

2.4.1 Classification of Ferrites

Ferrites may be classified further according to their crystal structures as spinel, garnet and magnetoplumbite. These are mainly distinguished with the ratio of the Fe_2O_3 to the other oxide component as illustrated in Table 3.

Spinel ferrites are also known as cubic ferrites. These ionic materials may be represented by the formula $MeFe_2O_4$ in which Me represents any one of several metallic elements such as Mn^{2+}, Fe^{2+}, Co^{2+}, Ni^{2+}, Cu^{2+} or Zn^{2+}. The prototype ferrite is Fe_3O_4. The spinel ferrites have low magnetic anisotropies and are magnetically soft; exceptions are those containing Co^{2+} with a coercivity of 10^5 A m^{-1} [28].

Table 3 Summary of ferrite structure types, typified by changes in the Fe_2O_3 – MeO (or Me_2O_3) modifier oxide ratios [34].

Spinel	$1Fe_2O_3$ - $1MeO$	(where MeO = transition metal oxide)
Garnet	$5Fe_2O_3$ - $3Me_2O_3$	(where Me_2O_3 = rare earth metal oxide
Magnetoplumbite	$6Fe_2O_3$ - $1MeO$	(where MeO = divalent metal oxide from group II A- BaO, CaO, SrO)

The garnets, which contain rare-earth oxides, have a very complicated crystal structure. They are represented by the chemical formula $Me_3Fe_5O_{12}$ in which Me represents the rare earth ions such as samarium, europium, gadolinium or yttrium. Garnet type ferrites exhibit high resistivity due to the absence of divalent metal ions. As a result of this fact, they are low loss materials at microwave frequencies.

Magnetoplumbites, that is hexagonal ferrites or hard magnets, have a crystal structure similar to the inverse spinel with hexagonal symmetry. The chemical formula may be represented as $MeFe_{12}O_{19}$ where Me is a divalent ion such as barium, lead or strontium. Barium hexaferrite ceramics, which have been the subject of this study, are important members of this type of ferrites and are described in detail in the following sections.

2.4.1.1 Hexagonal Ferrites

Hexagonal ferrites are classified into four main types depending on chemical formula and crystal structure. These are designated as M, W, Y, and Z with (BaO + MeO) / Fe_2O_3 ratios corresponding to 1:6, 3:8, 4:6, and 5:12, respectively. In all hexagonal ferrites Me represents a divalent ion or combination of divalent ions [35]. Figure 9 shows the phase equilibria in the $BaO:Fe_2O_3$ - Fe_2O_3 system with hexagonal ferrites located by points M, W, Y, and Z.
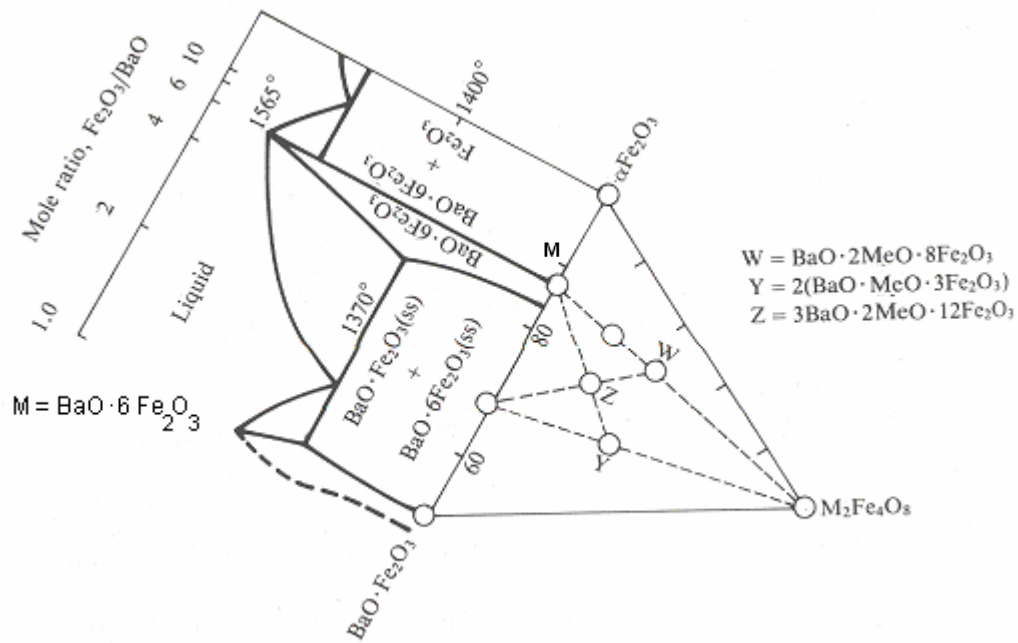
Figure 9 Relation of the phase equilibria of the $BaO:Fe_2O_3$ - Fe_2O_3 system with hexagonal ferrites M, W, Y, and Z [29].

Among the hexagonal ferrites the compound of greatest technological interest is the M type ferrite, $BaFe_{12}O_{19}$ or shortly "BaHF". High value of permeability (necessarily >1), high value of magnetization and good dielectric properties make them special candidates for radar absorbing materials at microwave frequencies [6, 25]. BaHF is isostructural with naturally occuring magnetoplumbite having the composition of $PbFe_{7.5}Mn_{3.5}Al_{0.5}Ti_{0.5}O_{19}$ [35]. The hexagonal crystal structure of BaHF with a space group of $P6_3/mmc$ consists of 10 layers of oxygen and has two chemical formula units in the unitcell. The 24 Fe^{3+} ions are distributed among five different crystallographic sites: three octahedral (12k, $4f_2$ and 2a), one tetrahedral ($4f_1$), and one bipyramidal site (2b) [18, 21]. Because of the fact that it is rather complicated, Braun [36] described the crystal structure of BaHF as a sequence of two structural units: the spinel blocks S $(Fe_6O_8)^{2+}$, separated by the block R $(BaFe_6O_{11})^{2-}$ that is as RSR*S*. Asterisk indicates a 180°-rotation of the corresponding block around the hexagonal axis. Figure 10 illustrates schematically this behavior.
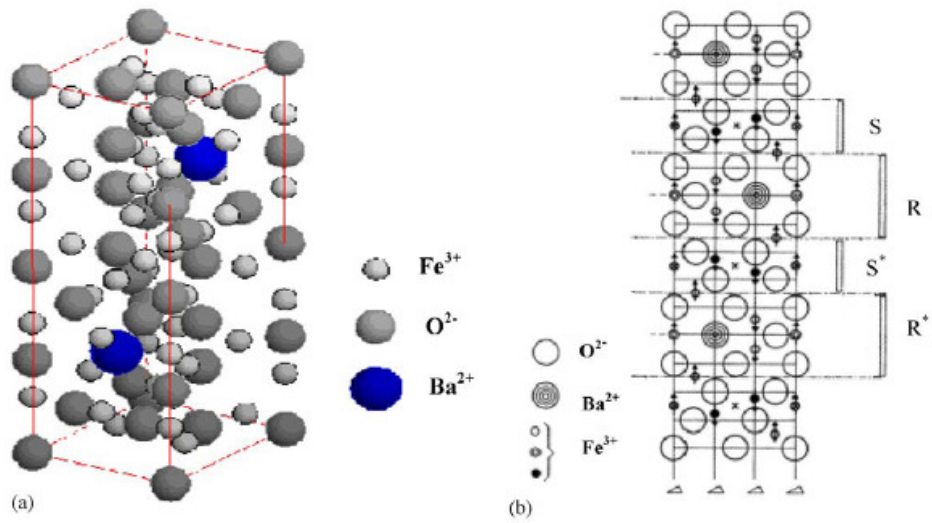
Figure 10 Crystal structure of Barium hexaferrite: (a) unit cell, (b) positions of ionic sites by blocks (SRS*R*) and by relative orientation of magnetic moments (↑↓) [37].

The crystallographic and magnetic properties of the five sublattices of BaHF were summarized in Table 4. The resulting magnetization M at a temperature T of BaHF per formula unit (f.u.) can be approximated by the following formula [18]:

$$M(T) = 6\sigma_{12k}(T) + \sigma_{2a}(T) + \sigma_{2b}(T) - 2\sigma_{4f1}(T) - 2\sigma_{4f2}(T) \tag{2.11}$$

where σ_i stands for the magnetic moment of an i-Fe^{3+} ion. Thus, it is the sum of five of the seven octahedral ions and the ion in the layer containing Ba minus the moments of the two octahedral and two tetrahedral ions [38]. Assuming a magnetic moment of 5 μ_B (μ_B is the Bohr magneton) per Fe^{3+} ion at 0 K and using Equation (2.11), net magnetization results as 20 μ_B per f.u. for the undoped BaHF at this temperature [18].

Table 4 Crystallographic and magnetic properties for the various cation sublattices of M-type hexagonal ferrite [18].

Sublattice	Coordination	Block	Ions per f.u.	Spin direction
12k	Octahedral	R-S	6	Up
$4f_1$	Tetrahedral	S	2	Down
$4f_2$	Octahedral	R	2	Down
2a	Octahedral	S	1	Up
2b	Fivefold	R	1	Up

2.4.1.2 Magnetization Dynamics in Hexagonal ferrites

The change in magnetization is generally brought about by rotation of spins or domain wall displacement. Domain wall dynamics are related with the low frequency applications. At very high frequencies (in GHz range), domain walls are unable to follow the field. Because of this fact spin rotation within domains is the only remaining magnetization mechanism [33]. Hence, in microwave applications of BaHF spin resonance or ferromagnetic resonance is a very important phenomenon.

From the macroscopic point of view, the magnetic ions may be substituted by divalent ions and the magnetization characteristics of BaHF was reported to be changed with increasing amount of non-magnetic substitution [19]. After the Fe^{3+} ions are substituted with Zn-Ti, Mn-Ti, Ti-Cu, Ni-Zr and Co-Mo, the saturation magnetization, coercivity and ferromagnetic resonant frequency of BaHF is changed [12].

2.4.1.3 Magnetocrystalline Anisotropy

The spin-orbit lattice coupling in magnetic materials results in orientation of the spins relative to the crystal lattice in a minimum energy direction which is called as 'easy direction' of magnetization [28]. Alligning spins in any other direction leads to an increase in anisotropy energy. It is designated as ε_{Kh} for hexagonal crystals and can be expressed approximately as [28]:

$$\varepsilon_{Kh} = K_{1h} \sin^2 \theta + K_{2h} \sin^4 \theta \tag{2.12}$$

where K_{1h} and K_{2h} are magnetocrystalline anisotropy constants and θ is the angle between the c axis and the magnetization vector. The energy minimum occurs when θ is equal to zero, making the c axis the easy direction.

2.5   Radar Absorbing Materials (RAMs)

Needs are increasing for materials which absorb the EM energy incident on them. EM wave absorbers are especially useful as radar absorbing materials, in anechoic chambers, as EM phantom materials and so on. For all of these materials, their primary function is to absorb and dissipate the EM energy into heat, although most absorbers do not dissipate enough energy to get detectably warm [39].

In RAM applications, when the surface of a target is covered or coated with a radar absorbing material, the radar echo is minimized and it results in low probability of detection of the target by the radar. The concept in using a RAM is mainly to reduce the radar cross-section (RCS) [31]. RCS of a target may be defined as the projected area of a metal sphere that would scatter the same power in the same direction that the target does. RCS may be calculated as follows [40] :

$$RCS = \sigma = \lim_{R \to \infty} 4\pi R^2 \frac{\left| \vec{E}_S \right|^2}{\left| \vec{E}_i \right|^2} \tag{2.13}$$

where R is the distance from scatterer to the point where the scattered power is measured, $\vec{E}_s$ and $\vec{E}_i$, are scattered and incident electric field respectively.

The earliest form of radar absorber, known as the "Salisbury screen", was a sheet of porous material impregnated with graphite and spaced a quarter-wavelength off a metallic backing plate and no reflection of microwaves were observed in narrow

frequency range [39]. The absorption bandwidth may be increased by the collection of several sheets in one structure, called a "Jaumann absorber".

RAMs are found in a number of forms. To begin with, ferrites are widely used materials for radar absorption purposes. They are often sintered in the form of small, rigid tiles. However, their application to a surface requires careful consideration of bonding techniques. Another method to manufacture ferrites as RAM involves embedding ferrite powders in a flexible matrix of natural or synthetic rubber. Several companies have developed spray-on mixtures in which ferrite powder particles are suspended in an epoxy vehicle [39]. However, this technique requires great attention. Since the powders are heavy they tend to settle at the bottom of the spray container. Another difficulty may be arised during spraying on the surface of the target. Uniform thickness and uniform properties are difficult to obtain unless skilled operators are available.

There are RAMs other than ferrites such as the conducting polymers. However, they present the disadvantage of poor mechanical properties.Therefore, it is necessary to blend them with a matrix, usually based on polymeric systems [41].

Another class of single-layer absorber (commonly used in anechoic chambers) depends upon carbon- loaded foam to provide loss but also uses a geometric transition from free space to the highly lossy medium to provide a dielectric gradient and thereby reduce reflections [39]. This type of absorbers are used commonly in the form of pyramids, mounted side by side, and connected at the base, forming a continuous slab of lossy dielectric [42].

2.5.1 Electromagnetic Loss Mechanisms

Generally, RAM is a lossy material. At microwave frequencies, the loss may be due to several mechanisms on the atomic and molecular level. However, for most practical dielectric absorbers a majority of the loss is due to the finite conductivity of the material, whereas for most magnetic absorbers, like ferrites, magnetization rotation within the domains is the principal loss mechanism [39]. Therefore, in any event, it is customary to group all loss mechanisms in terms of dielectric permittiviy (ε) and magnetic permeability (μ).

The real part of the complex permittivity gives information about storage capability of the electric energy whereas its imaginary part symbolizes the loss of electric energy [16]. In the same manner, the real part of the complex permeability gives information about storage capability of the magnetic energy and the imaginary part symbolizes the loss of magnetic energy [16].

2.5.2   Radar Absorber Measurement Techniques

Large numbers of methods are available for measuring radar absorption characteristics of a bulk material. Among these, two methods have become quite popular for the radar absorption measurement by using S-parameter techniques which are transmission/reflection (TR) waveguide method and free space method.

The waveguides, one form of uniform wave-guiding structures, are hollow metal pipes [1]. The waveguide method involves calculation of complex relative permittivity and permeability from transmitted and reflected scattering parameters measured by a network analyzer. A typical waveguide measurement setup is given in Figure 11.
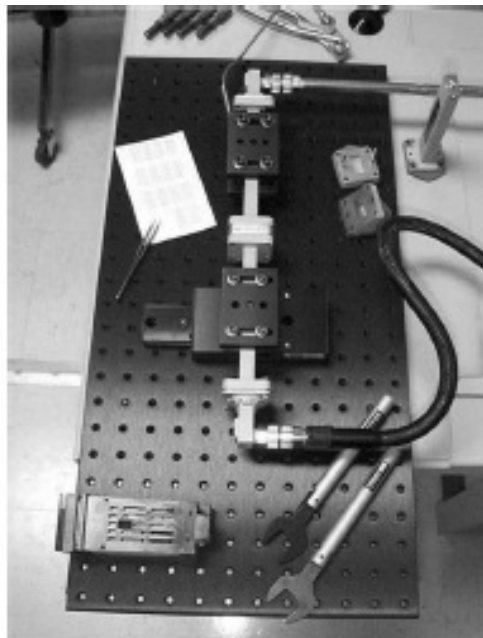
Figure 11 Waveguide measurement setup [43].

Waveguides have cut off frequencies, in other words, for operation frequencies below cut off frequency there is no electromagnetic wave propagation in a waveguide. On the other hand, when the operating frequency is higher than cut off frequency, there may be also other plane waves bouncing within the waveguide walls, which statisfy the boundary conditions as shown in Figure 12. This fact proves that waveguides may support more than one mode of operation. Propagation modes that may exist are governed by the electrical height and width of rectangular waveguides [39]. To prevent higher order mode propagation, it is very important to choose the waveguide dimensions accurately so that only dominant (lowest order) mode exist over the operating frequencies.
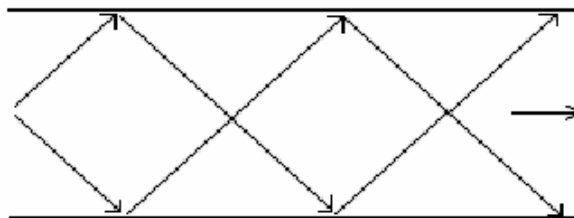
Figure 12 The increased wavelength of propagation down a waveguide is due to cross-guide propagation of a pair of bouncing plane waves [39].

Waveguide propagation modes can be grouped according to whether the electric or magnetic field is transverse to the direction of propagation. The former is known as TE (transverse electric) and the latter as TM (transverse magnetic). In TE modes, there is no component of electric field along the length of the waveguide and in TM modes there is no magnetic field along the length of the waveguide [1].

Combination of the integers m and n defines a possible mode that may be designated as the TM_{mn} and TE_{mn}. Hence, there are a double infinite number of TM and TE modes. For TM modes in rectangular waveguides, neither m nor n can be zero, for TE modes however, either m or n (but not both) can be zero [1]. The TE_{10} mode has the lowest cut off frequency of all modes in a rectangular waveguide and is called therefore the dominant mode.

The other very useful absorption technique is the free space method which was developed for the accurate determination of the dielectric constant and loss tangent of samples at microwave frequencies [44]. The measurement setup for free space method is illustrated in Figure 13. In this setup, a pair of spot focusing horn lens antennas are mounted on a large table. The sample to be measured lies between these antennas. Again, the scattering data are collected with the help of a vector network analyzer.

The waveguide method offered several advantages when compared to the free space method. First, in waveguide method the sample size can be smaller than the measurement wavelength. Thus, free field techniques at low frequencies (<40 GHz) require specimens with dimensions significantly greater than the wavelength of measurement [8]. In the waveguide method measurements are conducted in a closed waveguide walls which prevents multiple reflections from other sources. In the free space method, however, the inaccuracies may result from multiple reflections between the two horns via the surface and edges of the sample [44] .

One of the disadvantages of the waveguide method is that, if the material is not homogeneous, the small size samples do not represent fully the entire material. Besides, inhomogeneous materials may excite unwanted higher order modes at an air dielectric interface in waveguides [44]. Another disadvantage of the waveguide method is that it requires specimens in the form of parallel slices which fit the waveguide dimensions accurately with negligible air gaps, that is, it needs extensive preparation of sample.
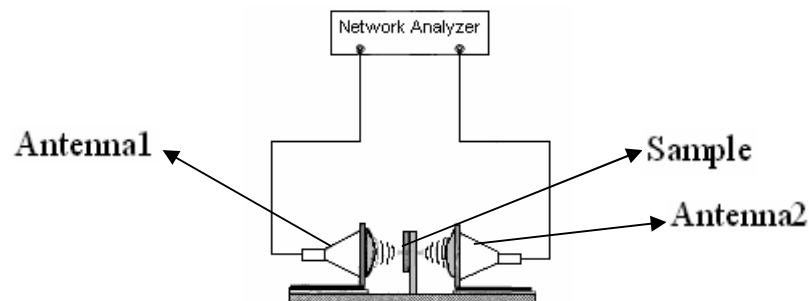
Figure 13 Free space measurement setup.

CHAPTER 3

EXPERIMENTAL PROCEDURE

3.1 General Procedure

Barium hexaferrite (BaHF) ceramics, prepared for the radar absorption purposes, were produced from powders which were synthesized by the "mixed oxide" approach in this research. The chemical compositions of the barium ferrite powders were modified by doping with Ti and/or Co. In order to obtain magnetoplumbite structure, a calcination process was carried out at 1020 $^{\circ}$C for 10 hours. The calcined ferrite powders were then used to manufacture small ceramic tiles by sintering each composition at 1250 °C with soaking times ranging from 1 to 16 hours.

X-ray diffraction (XRD) and scanning electron microscope (SEM) studies were conducted to examine the effects of dopants and sintering variables on the crystal structure and development of microstructure. The electromagnetic absorption properties of the ceramics were characterized within 8 to 17 GHz frequency range (X and Ku bands) by using a vector network analyzer. The complex dielectric constant ε and magnetic permeability µ were determined by measuring electromagnetic reflection and transmission coefficients of the ceramic tiles.

3.2 Experimental Technique

3.2.1 Preparation of Ferrite Powders

Generally the powders for making magnetic ceramics are produced by a variety of processing techniques including methods such as co-precipitation, hydro-thermal synthesis, sol-gel and micro emulsion synthesis [45]. In a study conducted by İyiel [46], a co-precipitation method was used whereby hydroxides of barium and iron were precipitated simultaneously from a mixed aqueous salt solution resulting in

highly dense barium ferrite powders with micron size particles. However, these powders failed to exhibit characteristic absorption maxima with respect to frequency. In contrast, the powders produced by the mixed oxide technique have the potential of displaying maxima in their loss factor spectrum [12, 14, 24, 25]. Therefore, in the present study the mixed oxide technique was preferred over chemical routes of powder preparation.

The flowchart showing the steps involved in the preparation of the barium ferrite powder is given in Figure 14. High purity powders of Fe_2O_3 (Merck 3924), TiO_2 (Merck 812), $BaCO_3$ (Merck 1712) and Co_3O_4 (Merck 2543) were used as the raw materials for synthesizing BaHFs. The molecular formulae of the hexaferrites prepared for this study study are listed in Table 5.

Table 5 Chemical formulae of the barium hexaferrite powders produced in the present study.

Chemical Formulae of the Powders
$BaFe_{12}O_{19}$
$BaFe_{11.33}Ti_{0.5}O_{19}$
$BaFe_{10.67}TiO_{19}$
$BaFe_{10}Ti_{1.5}O_{19}$
$BaFe_{11.5}Co_{0.5}O_{19}$
$BaFe_{11}CoO_{19}$
$BaFe_{10.5}Co_{1.5}O_{19}$
$BaFe_{11}Ti_{0.5}Co_{0.5}O_{19}$
$BaFe_{10}TiCoO_{19}$
$BaFe_9Ti_{1.5}Co_{1.5}O_{19}$

Mixtures of the raw materials were obtained by weighing each oxide constituent in accordance with the stoichiometry of the ferrite type. The batch for each ferrite type weighed about 300 g. The oxides were blended for 1.5 hours in a large porcelain mortar by using distilled water as the mixing medium. The slurry obtained was dried in an oven at 80 ^{o}C for 24 hours. Cylindrical compacts of ferrite mix were pressed under 200 kg/cm^2 pressure and these were calcined in air at 1020 ^{o}C for 10 hours in a muffle furnace. The thermal synthesis reaction assumed to occur may be written as:

$$BaCO_3 + 6\ Fe_2O_3 = BaFe_{12}O_{19} + CO_{2(g)} \tag{3.1}$$
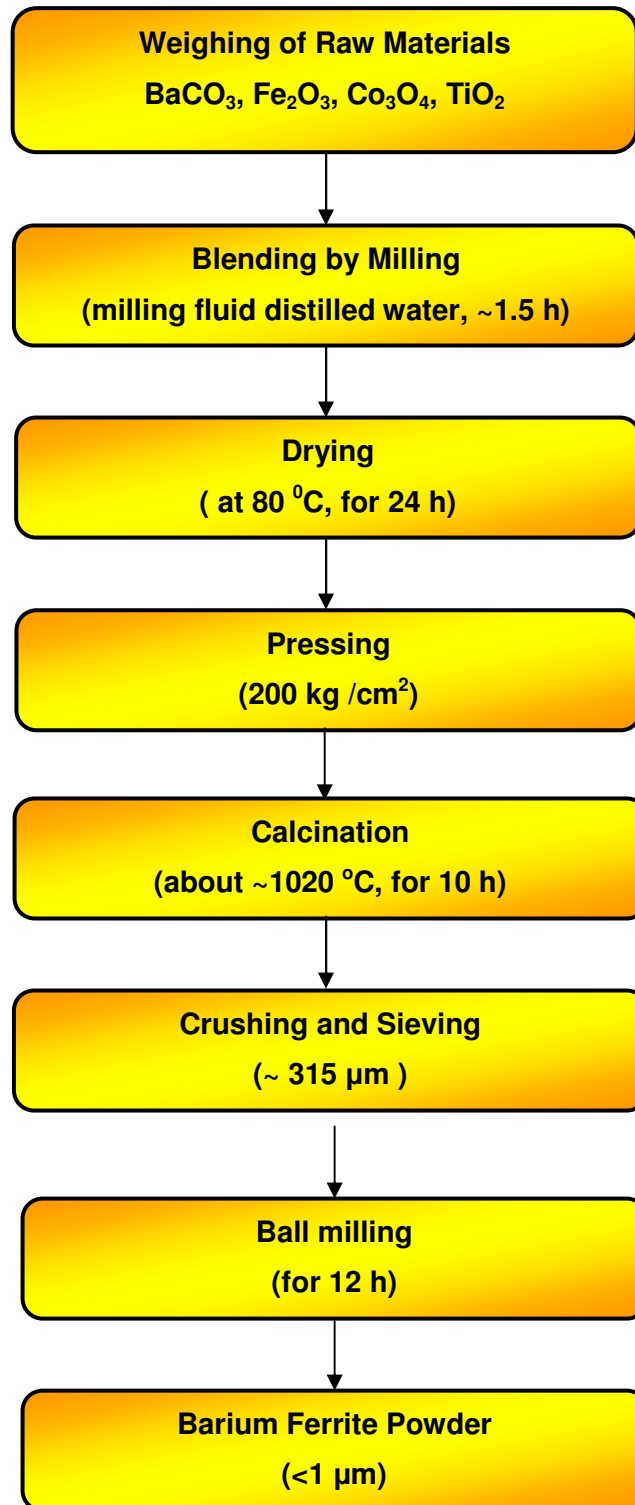
Figure 14 The flowchart showing the steps of barium ferrite powder preparation.

The barium hexaferrite slugs obtained from calcination were crushed and then sieved through 315 μm aperture. The powders were ball milled in a mullite jar for 12 hours at 70 rpm using stainless steel balls as the milling media. Ball to powder ratio was 7 to1 in weight. Distilled water was used as the milling medium. The milled slurry was dried thoroughly before use in ceramic manufacture. SEM examination revealed that the milled powders were submicron in size as shown in Figure 15.
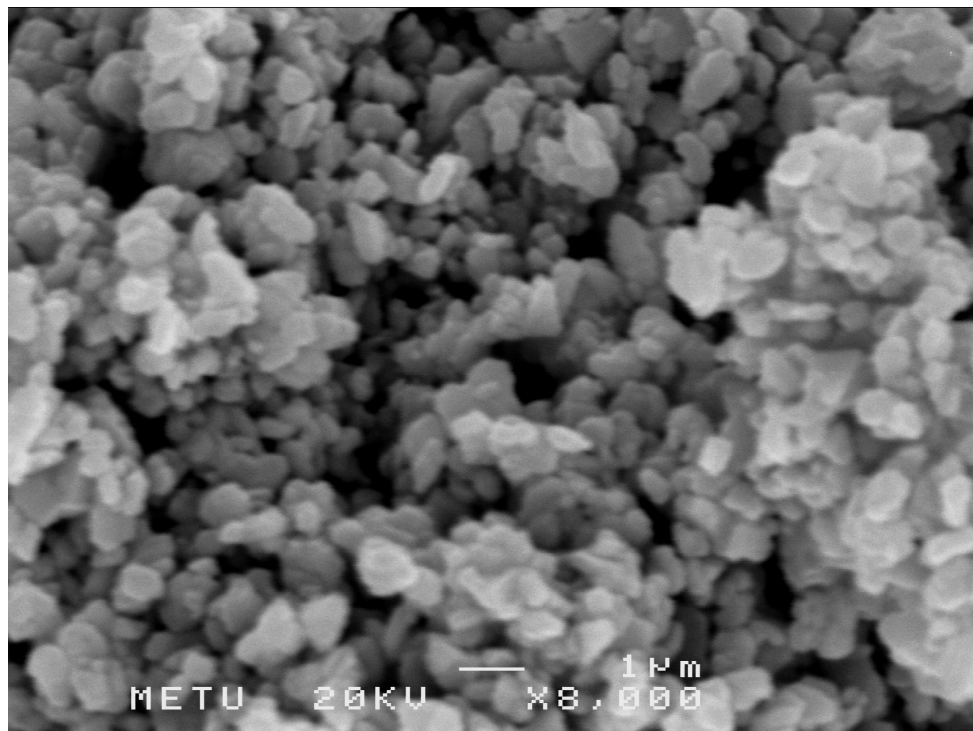
Figure 15 A SEM photo of the BaHF powder produced by the mixed oxide technique used in this study.

Formation of the magnetoplumbite structure was checked with powder XRD method. XRD verified formation of the magnetoplumbite structure in all products as shown in Figure 16. The peaks of the doped ferrite powders appeared almost at the same diffraction angles with the undoped one but intensities were different.
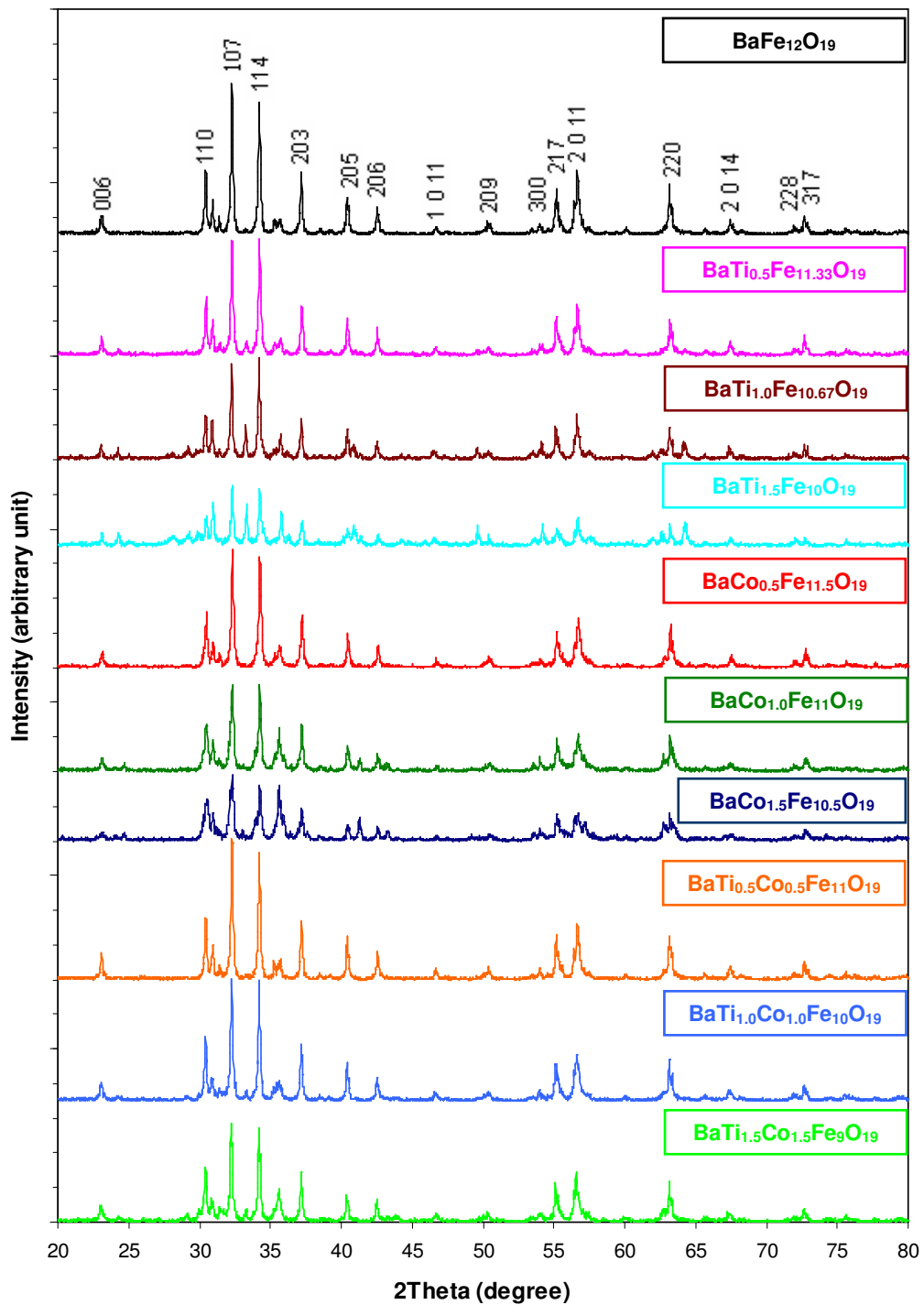
Figure 16 XRD patterns of the powders produced in this study after calcination.

Ti addition to undoped M-type BaHF caused partial formation of barium monoferrite ($BaFe_2O_4$) whose major peak was lying between (107) and (114) planes. The barium monoferrite form is known to form as a transitional phase [37].

In the powders of the ferrites, $BaFe_{11.5}Co_{0.5}O_{19}$, $BaFe_{11}CoO_{19}$, $BaFe_{11}Ti_{0.5}Co_{0.5}O_{19}$, and $BaFe_{10}TiCoO_{19}$ no transitional phase was observed. However, in the $BaFe_{11.33}Ti_{0.5}O_{19}$, $BaFe_{10.67}TiO_{19}$, $BaFe_{10}Ti_{1.5}O_{19}$, and $BaFe_9Ti_{1.5}Co_{1.5}O_{19}$ powders the major peak of the barium monoferrite became visible. This phase remained either as trace or disappeared completely in subsequent sintering stages.

3.2.2 Preparation of Ceramics

Tiles of ferrite ceramics were prepared in accordance with the flowchart shown in Figure 17. A green ceramic tile was produced by pressing 10 grams of the ferrite powder in a hardened steel die having a cavity which measured 28.5 mm by 15.5 mm. A 3% solution of PEG 6000 in water was used as plasticizer and external lubricant. Rectangular compacts of ferrites were obtained by pressing under a load of 1000 kgf. These were sintered in a muffle furnace at 1250 $^{\circ}$C for soaking durations of 1 h, 2 h, 3 h, 4 h, 8 h and 16 h. The heating and cooling rates in all samples were 4 $^{\circ}$C/min. Some of the sintered ceramics produced in this study are shown in Figure 18.

Cobalt has an increased propensity of evaporation above 1000 $^{\circ}$C. For an assessment of compositional variations due to possible Co evaporation, ferrite ceramics containing Co were sintered at 1250 $^{\circ}$C for 8 hours. The ceramics used for this purpose were $BaFe_{11}CoO_{19}$ and $BaFe_{10}TiCoO_{19}$. In closed alumina saggars, containing Co_3O_4 bedding powder to suppres Co losses, the weight loss in both samples was confined to 0.2 weight percentage, wt % . When sintered in air, the weight loss was about 0.3 wt %. Therefore, for lower Co loss all compacts containing Co were sintered in closed and sealed alumina saggars containing Co_3O_4 bedding powder.
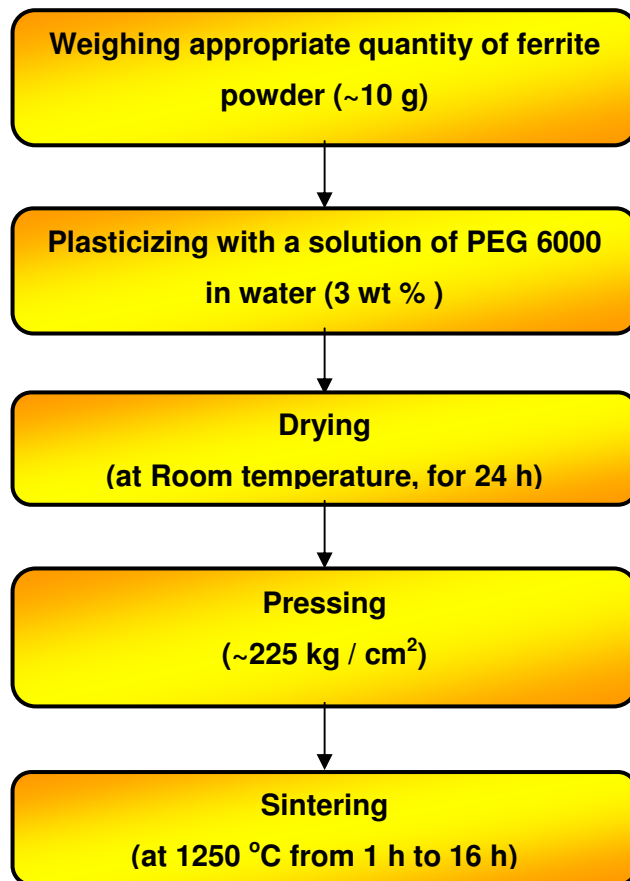
Figure 17 The flowchart of ferrite ceramic tile production.
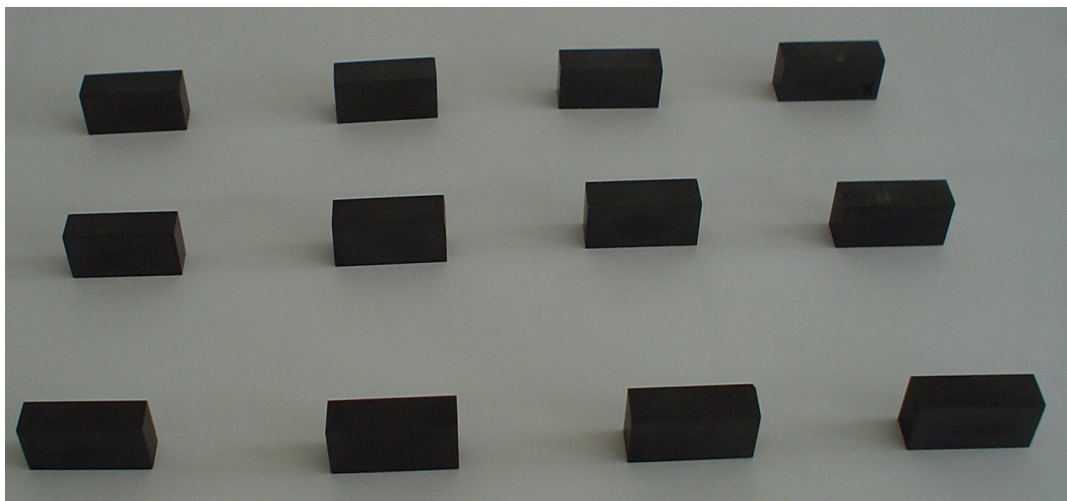
Figure 18 Barium hexaferrite ceramic tiles prepared by sintering.

3.3   Characterization of Properties

3.3.1   Density Measurements of Sintered Ceramics

The density of sintered ferrites were determined by using the Archimedes' buoyancy principle. Xylene (Merck) was the buoyancy fluid. The weight measurements were performed on a Precisa XB 220A model electronic balance equipped with a density determination kit.

The formula used for the calculation of the bulk density was:

$$\rho_{bulk} = \frac{W_{dry} \cdot \rho_{xylene}}{W_{sat} - W_{susp}} \qquad (3.2)$$

where;

ρ_{bulk} : Bulk density of the sample in g/cm^3,

W_{dry} : Dry weight of the sample in grams,

ρ_{xylene} : Density of xylene (0.86 g/cm^3),

W_{sat} : Saturated weight of the sample in grams,

W_{susp} : Suspended weight of the sample in grams.

Dry weight of the as-sintered sample, indicated as W_{dry}, was obtained by weighing it in air. Then the sample was immersed in xylene and kept for 48 hours to get full saturation. Next, the suspended weight, W_{susp}, was determined by weighing the sample while it was suspended in xylene. Then it was taken away from the beaker and excess xylene was wiped out. Finally, the sample was weighed in air immediately which was recorded as saturated weight, W_{sat}. All weight determinations were made with an accuracy of ± 0.0001 g.

3.3.2   Microstructural Characterization

Microstructures of sintered ferrites were evaluated by examination of fracture surfaces as well as polished and etched sections by using a JEOL JSM 6400 scanning electron microscope, equipped with NORAN X-Ray microanalysis

system for energy dispersive spectroscopy, EDS, analysis. EDS analyses were not dependable since Lα of Ba, Lβ of Ba and Co Kα peaks overlapped with Kα of Ti, Kβ of Ti and Kβ of Fe respectively.

Polished sections of the ceramics for SEM investigations were prepared with conventional techniques of metallography by grinding on 800 to 1200 grit emery paper and then polishing with diamond paste with 1μm particle size. Afterwards, etching was done by exposing the polished surface to a boiling aqueous solution of H_2O (4 ml) - HNO_3 (4 ml) - CH_3COOH (3 ml) - HCl (3 ml) - $HClO_4$ (2 ml) - H_2SO_4 (0.25 ml) for 8 minutes. Before SEM investigation all surfaces of ceramics were coated with Au alloy to obtain electrical conductivity.

3.3.3 X-Ray Diffraction

The phases present in the calcined ferrite powders as well as those in the fired ceramics were identified by powder XRD methods using a D/MAX2200/PC Rigaku XRD unit with Cu Kα radiation. The diffraction data were collected in the 2θ range from 20° to 80° at a count time of one second for 0.02° widths. Divergent high limiting slit was 5 mm, divergent slit and scattering slit was 1 degree and receiving slit was 0.15 mm. Precise lattice parameters were calculated by processing the XRD data through Cohen's method [47].

3.3.4 Measurement of Microwave Absorption Properties

Microwave absorption characteristics of sintered ceramic tiles were evaluated by determination of their reflection and transmission properties with the help of a HP 8720D network analyzer (50 MHz – 20 GHz). The outline of the set-up is shown in Figure 19. The measurement system was constructed by coaxial cables, adapters and waveguides.
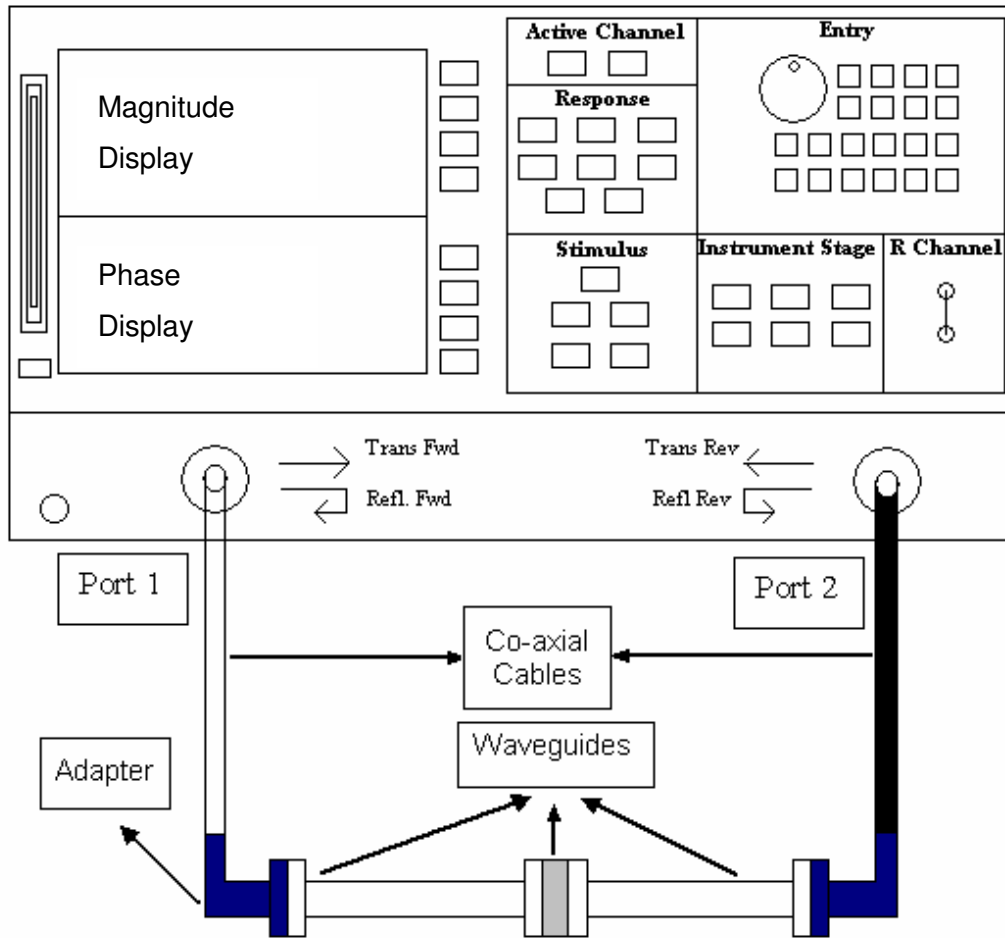
Figure 19 Schematic representation of the set up used for microwave absorption
properties.

In a measurement, the ceramic tile was placed into the rectangular waveguide,
sample holder, which was lying between two longer waveguides. The reflection
coefficient, designated as S_{11}, and the transmission coefficient, designated as S_{21},
were determined over the frequency range 8 to 11.5 GHz for X Band and 12-17
GHz for Ku Band. The designation of S_{21} means that electromagnetic waves were
sent from port 1 and the transmitted waves were received at port 2. As in the
former case, in S_{11}, electromagnetic waves were sent from port 1 and reflected
waves were received at port 1. Preliminary measurements in ceramic tiles
revealed that $S_{11} = S_{22}$ and $S_{21} = S_{12}$; therefore determination of the parameters S_{11}
and S_{21} was sufficient for elucidating the EM interactions.

For the measurement of S_{21} and S_{11}, the size of the tiles were reduced to rectangular waveguide dimensions of 22.86 mm x 10.16 mm x 6.50 mm for X-band and to 15.60 mm x 7.70 mm x 4.50 mm for Ku band. The size of the waveguides used in X-band had to be different from than used in Ku-band to ensure single dominant waveguide mode operations,TE_{10}, over the band.

The calibration of the set-up shown in Figure 19 had a crucial importance for obtaining reproducible results. Therefore; the entire system was calibrated with the thru reflect line calibration (TRL) procedure. This calibration was necessary to overcome systematic errors such as test port mismatch and leakage from connections.

Basically there were three major steps in TRL calibration [48]. In the first step, named as the THRU calibration step, the test ports were mated tightly with coaxial cables, adapters and long waveguides without sample holders and then transmission frequency response as well as port match were measured in both directions as seen in Figure 20. In the second step of TRL calibration, which was the REFLECT calibration step, highly reflective device (a short circuit in this case) was connected to each test port and its reflection coefficient was measured as shown in Figure 21. In the final step, LINE calibration was done by inserting a short length of waveguide between port 1 and 2 as seen in Figure 22.
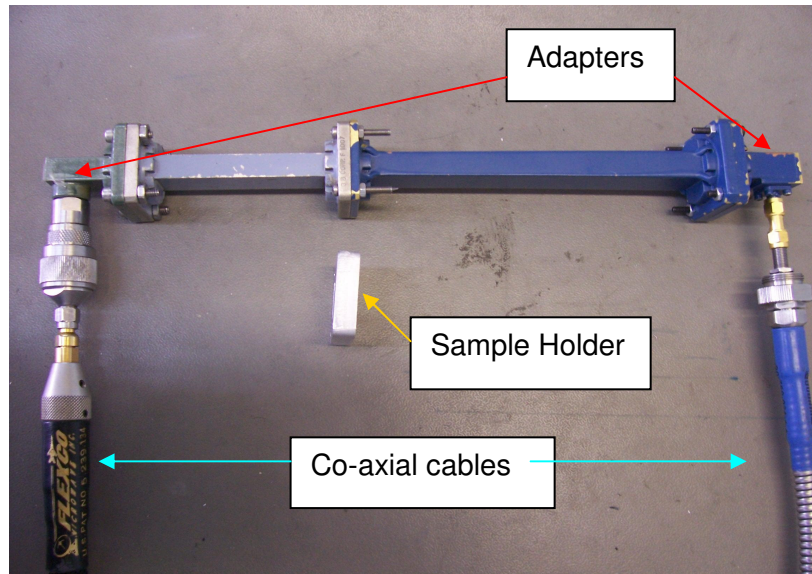
Figure 20 Thru calibration procedure in TRL calibration.
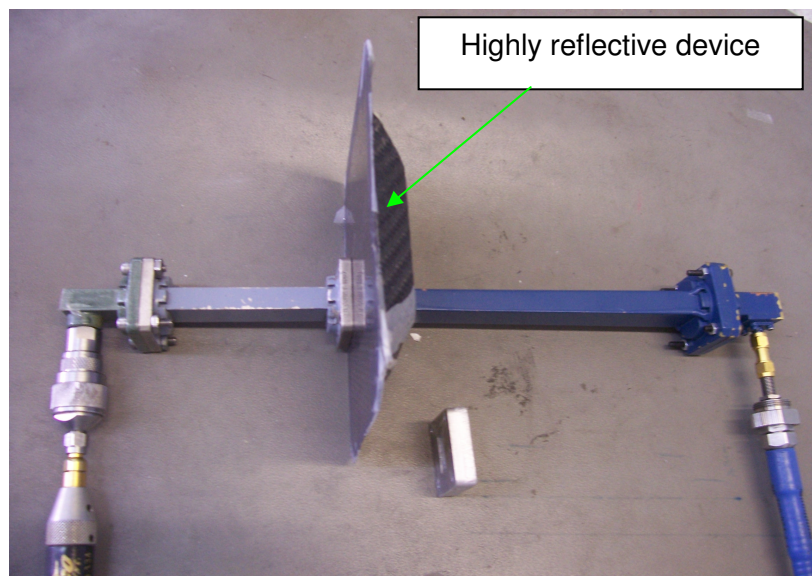
Figure 21 Reflect calibration procedure in TRL calibration.
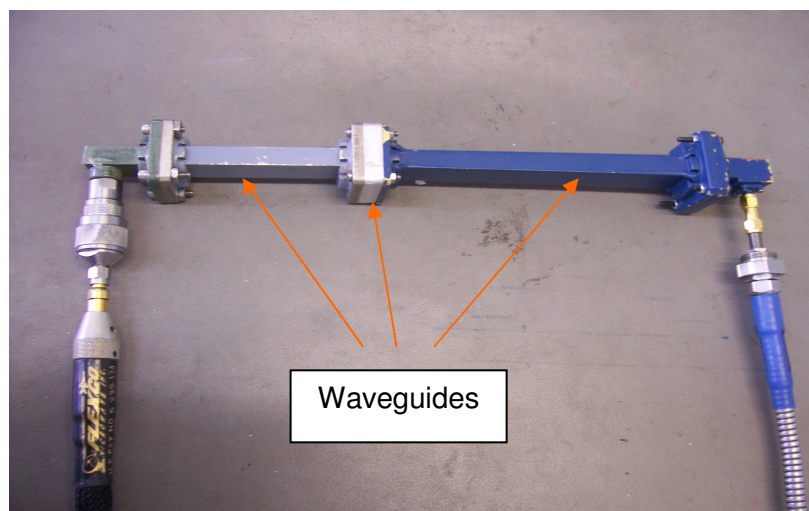
Figure 22 Line calibration procedure in TRL calibration.

3.3.5   Magnetic Hysteresis

ADE Magnetics EV9 model vibrating sample magnetometer was used to determine the hysteresis loops of ferrite ceramics at room temperature. The maximum applied field was 18,000 Oe. The magnetization (emu / gram) versus applied field (oersted) curves were drawn to find out coercivity values of the samples. The steps of data taken with respect to applied field during measurements are listed in Table 6.

Table 6 The steps of hysteresis data taken with respect to applied field.

Applied Field (Oe)	The Steps of Data Taken
-18000 to -10000	2000
-10000 to -5000	1000
-5000 to 5000	500
5000 to 10000	1000
10000 to 18000	2000

CHAPTER 4

EXPERIMENTAL DATA AND RESULTS

4.1　X-Ray Diffraction Analyses on Sintered Ceramics

The X-ray diffractograms of barium hexaferrite ceramics sintered at 1250 ^{o}C for 2 hours are shown in Figure 23. The XRD pattern of the undoped BaHF ceramic was equivalent to that of the magnetoplumbite as revealed in the JCPDS card file 43-0002. The diffractograms of the ceramics containing Ti also exhibited single phase BaHF characteristics; thus, the ceramics with compositions $BaFe_{11.33}Ti_{0.5}O_{19}$, $BaFe_{10.67}TiO_{19}$, and $BaFe_{10}Ti_{1.5}O_{19}$ had essentially magnetoplumbite crystal structure. The same was true when BaHF was modified by simultaneous doping with Co and Ti. Therefore, the XRD patterns of $BaFe_{11}Ti_{0.5}Co_{0.5}O_{19}$, $BaFe_{10}TiCoO_{19}$, and $BaFe_{9}Ti_{1.5}Co_{1.5}O_{19}$ resembled exactly that of the undoped BaHF.

When the soak duration, while sintering at 1250 ^{o}C, was prolonged to 16 hours, the XRD pattern of BaHF and those of the BaHF compounds doped with Ti or Ti and Co, remained essentially independent of temperature as seen in Figure 24. The exception to this was the compound $BaFe_{11}Ti_{0.5}Co_{0.5}O_{19}$ in which the intensities of the peaks from 006, 008 and 220 planes became pronounced with longer sintering treatment.
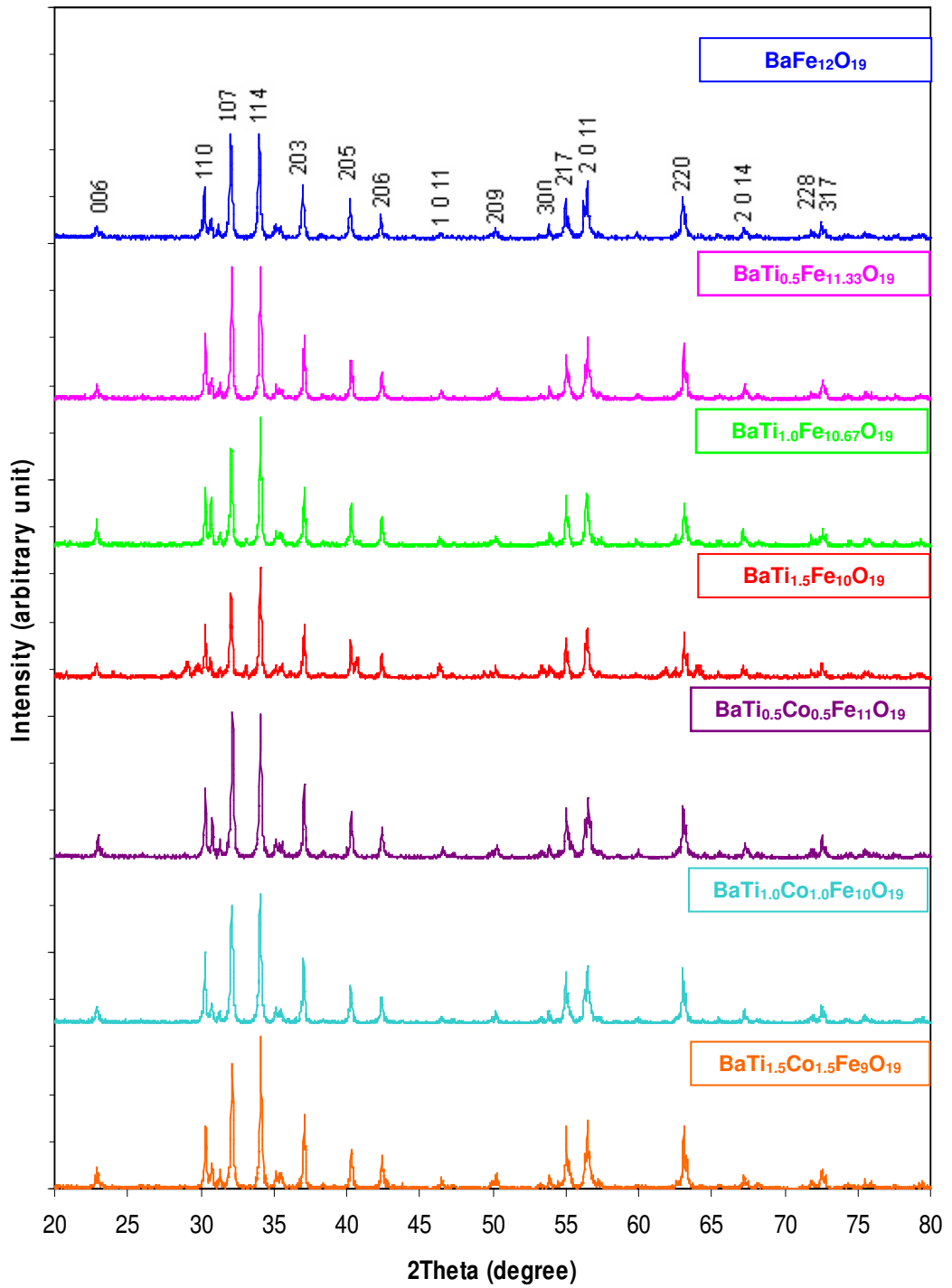
Figure 23 XRD patterns of undoped and modified BaHF ceramics soaked for 2 hours at 1250 °C.
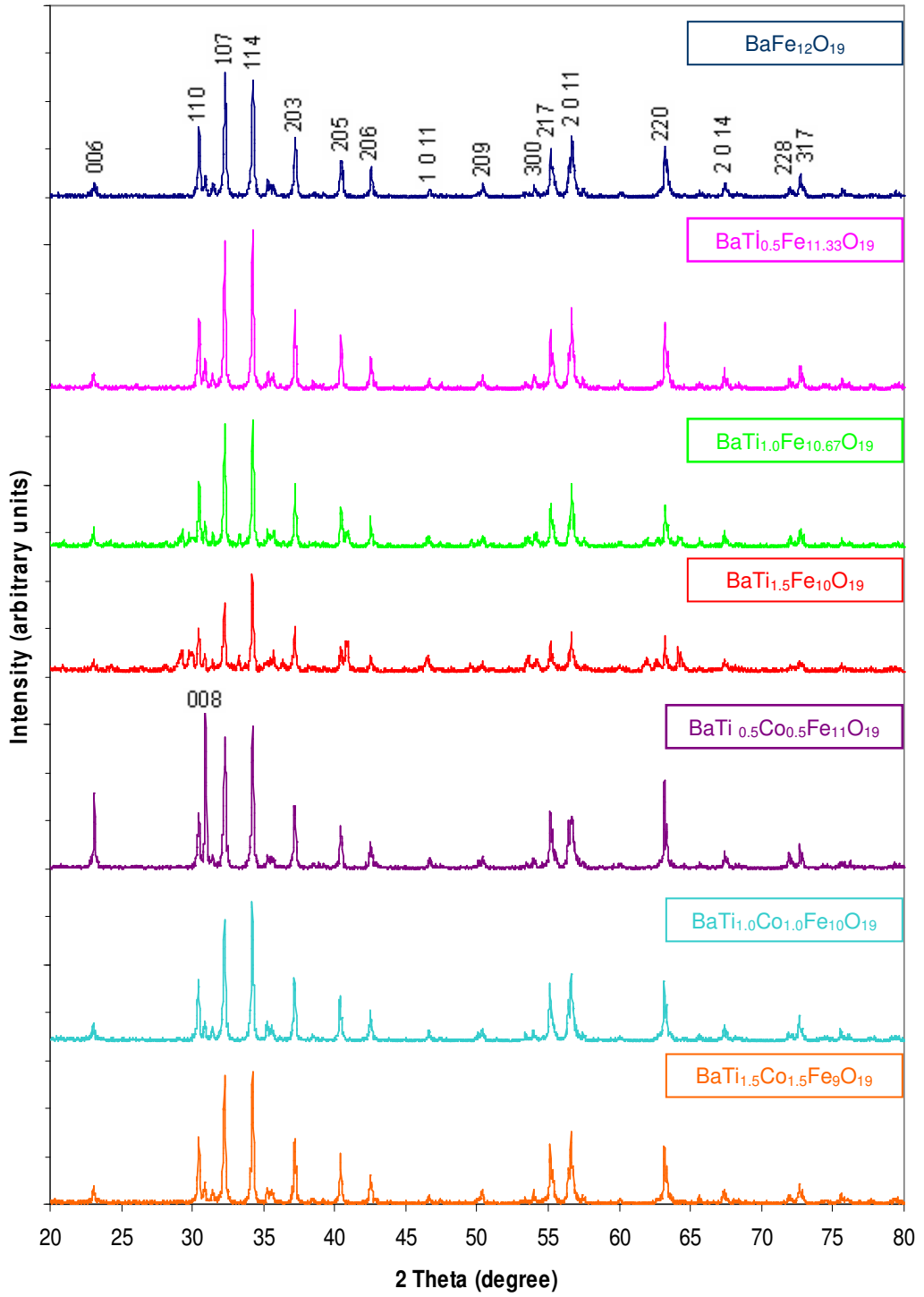
Figure 24 XRD patterns of undoped and modified BaHF ceramics soaked for 16 hours at 1250 °C.

Rather large anomalies were observed in the XRD patterns of the BaHF compounds doped with Co only. The diffractograms of the compounds $BaFe_{11.5}Co_{0.5}O_{19}$, $BaFe_{11}CoO_{19}$, and $BaFe_{10.5}Co_{1.5}O_{19}$ are shown in Figure 25. In general, the major peaks of BaHF were preserved with minor shifts in their positions. The peaks representing BaHF were marked with (*) on the XRD patterns. The additional peaks in the XRD patterns were attributed to the formation of unidentified new phase(s).

When the BaHF compounds doped with cobalt were fired for longer duration at 1250 ^{o}C the number of unidentified peaks increased. In view of the increased uncertainities, the ferrites doped with Co were left outside the scope of the present study.
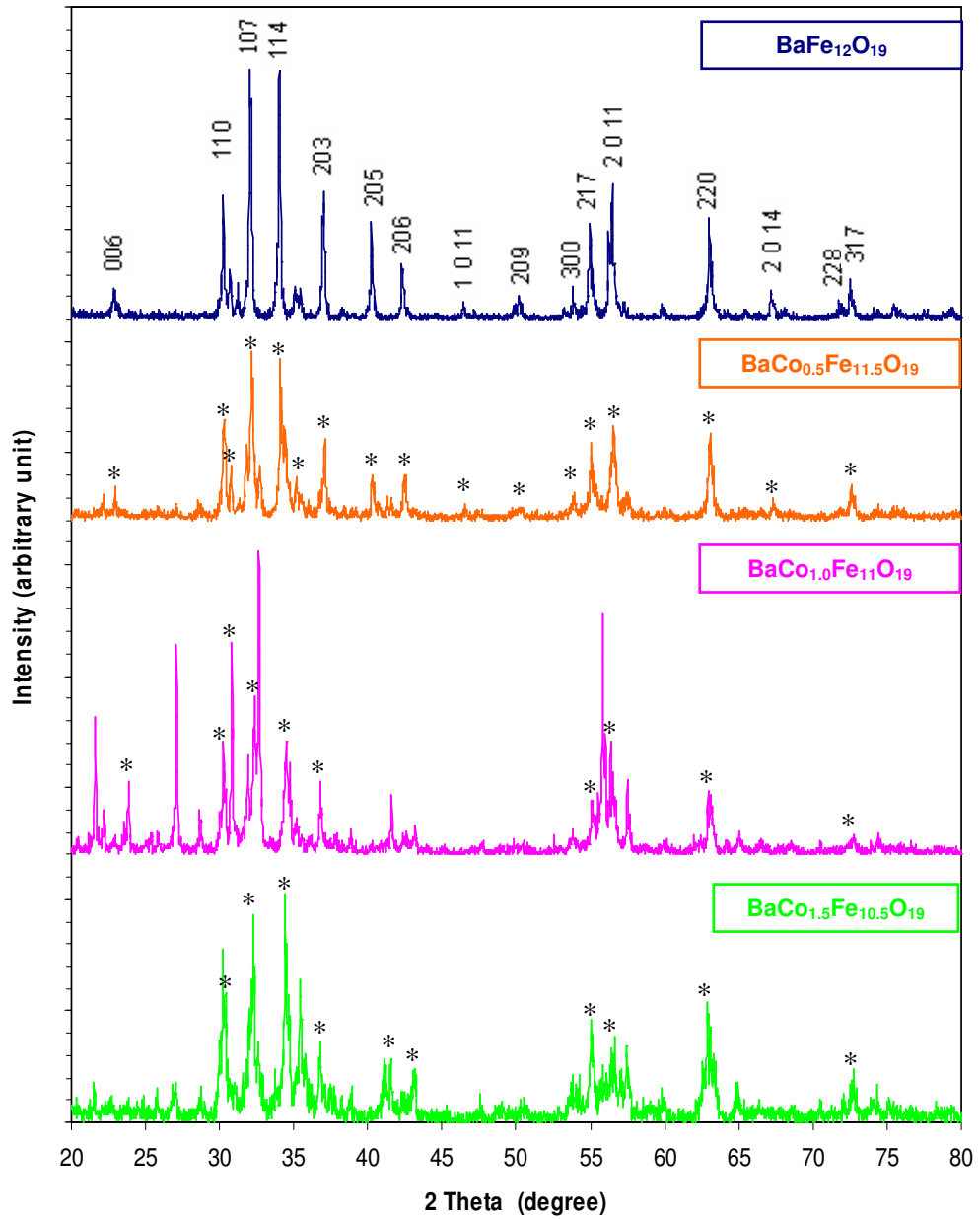
Figure 25 XRD patterns of undoped and Co doped BaHF ceramics soaked for 2 hours at 1250 °C.

The lattice parameters "a" and "c" of the hexagonal ferrites were calculated by treating the XRD data with Cohen's method [47]. In order to calculate the x-ray density ($\rho_{x\text{-ray}}$) of the powders, these parameters were substituted to the following expression [35]:

$$\rho_{x-ray} = \frac{n \cdot A}{V_c \cdot N_A} \tag{4.1}$$

where;

$\rho_{x\text{-ray}}$: X-ray density of the sample, g/cm^3

n   : Number of atoms associated with each unitcell

M   : Molecular mass of the ferrite compound

V_c : Volume of the unit cell, cm^3

N_A : Avogadro's number $\left(6.02 \cdot 10^{23}\right)$, mol^{-1}

By inserting these terms into Equation (4.1), the x-ray density could be expressed as:

$$\rho_{x-ray} = \frac{2 \cdot M}{\left(\dfrac{a^2\sqrt{3}}{2}\right) \cdot c \cdot \left(6.02 \cdot 10^{23}\right)} \tag{4.2}$$

The results obtained on lattice parameters and X-ray density of the ferrites are summarized in Table 7. It could be stated that doping BaHF with Ti and Ti plus Co caused a slight increase both in the "a" and the "c" parameter. X-ray density of the ferrite compounds decreased as the amount of dopants increased. The change in the lattice parameters were smaller than the difference between the ionic radius of the doping agents and Fe. This fact confirmed that the crystal structure of the corresponding ferrite did not change [37]. Results on "a" and "c" parameters of the Co and Ti doped BaHF ceramics obtained in the present study support earlier findings of Nedkov and Petkov [49].

Table 7 Lattice parameters and X-ray density of the ferrite compounds.

Molecular Formula of Ferrite	Lattice Parameter "a" (A°)	Lattice Parameter "c" (A°)	X-ray density (g/cm³)
$BaFe_{12}O_{19}$	5.8882	23.1848	5.3046
$BaFe_{11.33}Ti_{0.5}O_{19}$	5.8884	23.1942	5.2378
$BaFe_{10.67}TiO_{19}$	5.8924	23.2202	5.1634
$BaFe_{10}Ti_{1.5}O_{19}$	5.8907	23.2272	5.1007
$BaFe_{11}Ti_{0.5}Co_{0.5}O_{19}$	5.8929	23.2034	5.2803
$BaFe_{10}TiCoO_{19}$	5.8921	23.2077	5.2691
$BaFe_9Ti_{1.5}Co_{1.5}O_{19}$	5.8928	23.2464	5.2475

4.2   Densification in Sintered Ceramics

Data on bulk density of the undoped and doped BaHF ceramics sintered at 1250 °C with different soak durations are given in Table 8.

Table 8 Relative sintered density of BaHF ceramics for different soak durations.

Composition of the Ferrites	Soaking Time (hours)					
	Bulk Density (g/cm³)					
	1	2	3	4	8	16
$BaFe_{12}O_{19}$	4.7280	4.7702	4.7345	4.7350	4.7605	4.1864
$BaFe_{11.33}Ti_{0.5}O_{19}$	4.0944	4.1024	4.0984	4.2525	4.4595	3.6107
$BaFe_{10.67}Ti_{1.0}O_{19}$	4.8119	4.9131	4.9923	4.9818	4.9943	4.1487
$BaFe_{10}Ti_{1.5}O_{19}$	4.9260	4.9867	5.0108	5.0100	5.0279	4.3958
$BaFe_{11}Ti_{0.5}Co_{0.5}O_{19}$	4.7230	4.7950	4.7699	4.7701	4.8567	4.8164
$BaFe_{10}Ti_{1.0}Co_{1.0}O_{19}$	4.6759	4.7042	4.8384	4.9534	5.0143	4.0052
$BaFe_9Ti_{1.5}Co_{1.5}O_{19}$	4.7229	4.9639	4.9496	4.9279	4.9334	4.1973

The data were used to assess degree of densification, expressed in terms of percentage theoretical density, as follows:

$$\rho_{\%th} = \frac{\rho_{bulk}}{\rho_{x-ray}} \cdot 100 \qquad (4.3)$$

where;

$\rho_{\%th}$: the density of the ceramic reference to the theoretical density
ρ_{bulk}: the bulk density of the sample, g/cm^3
ρ_{x-ray}: the X-ray density of the sample; g/cm^3

Relative sintered density of the ceramics obtained by processing the density data in Equation (4.3) are listed in Table 9. Maximum densities were obtained in the ceramics $BaFe_{10.67}Ti_{1.0}O_{19}$ and $BaFe_{10}Ti_{1.5}O_{19}$ sintered at 1250 ^{o}C for 8 hours. For reasons which remained unknown, the hexaferrite manufactured with 0.5 mole Ti substitution displayed the minimum density for all soak durations. The same behavior was observed by Marino-Castellanos [37] in a BaHF ceramic containing 0.6 mole Ti substitution.

Table 9 Variation of theoretical density for different soak duration.

Composition of the Ferrite	Soaking Time (hours)					
	% Theoretical Density					
	1	2	3	4	8	16
$BaFe_{12}O_{19}$	89.13	89.93	89.25	89.26	89.74	78.92
$BaFe_{11.33}Ti_{0.5}O_{19}$	77.53	77.68	77.61	80.53	84.45	68.37
$BaFe_{10.67}Ti_{1.0}O_{19}$	92.65	94.60	96.13	95.92	96.16	79.88
$BaFe_{10}Ti_{1.5}O_{19}$	96.15	97.34	97.81	97.79	98.14	85.80
$BaFe_{11}Ti_{0.5}Co_{0.5}O_{19}$	89.33	90.69	90.21	90.22	91.86	91.09
$BaFe_{10}Ti_{1.0}Co_{1.0}O_{19}$	88.64	89.18	91.72	93.90	95.05	75.93
$BaFe_{9}Ti_{1.5}Co_{1.5}O_{19}$	89.80	94.39	94.11	93.70	93.81	79.81

4.3 SEM Analyses on Sintered Ferrite Ceramics

SEM analyses were confined to freshly fractured surfaces, as well as polished and etched sections, of the ceramics sintered at 1250 ^{o}C for 2 hours. The micrograph of the undoped BaHF ceramic is shown in Figure 26. The microstructure consisted of hexagonal plates measuring about 10 µm across the diagonal with 1 µm thickness. Etched surface revealed that a certain degree of anisotropy was present due to the partial self-alignment of the grains in the c direction.
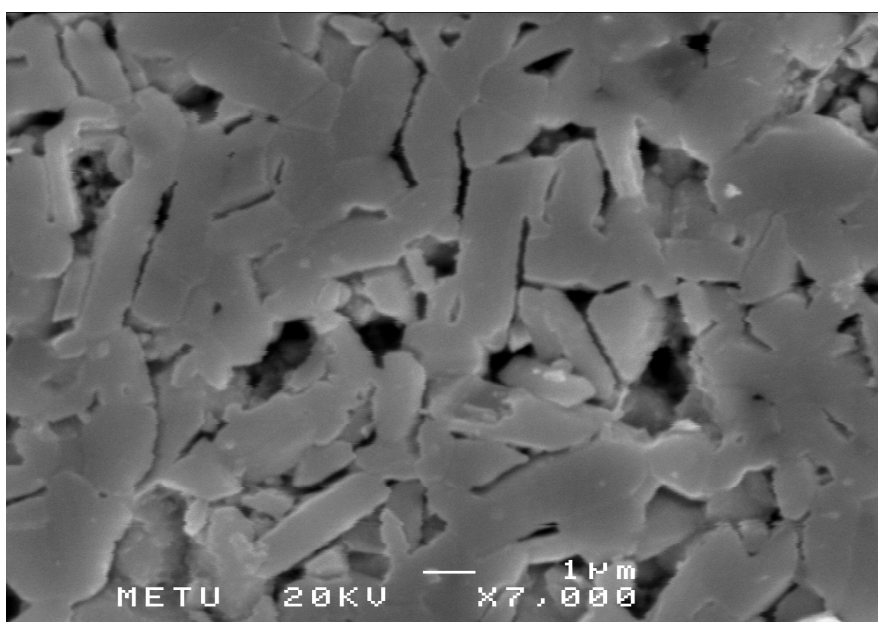
Figure 26 SEM micrograph of undoped BaHF ceramic. Sample was soaked at 1250 ^{o}C for 2 hours and etched.

As shown in Figure 27, the microstructure of the ceramic containing 0.5 mole Ti was similar to that of undoped BaHF except that the grains tended to be more equiaxed.
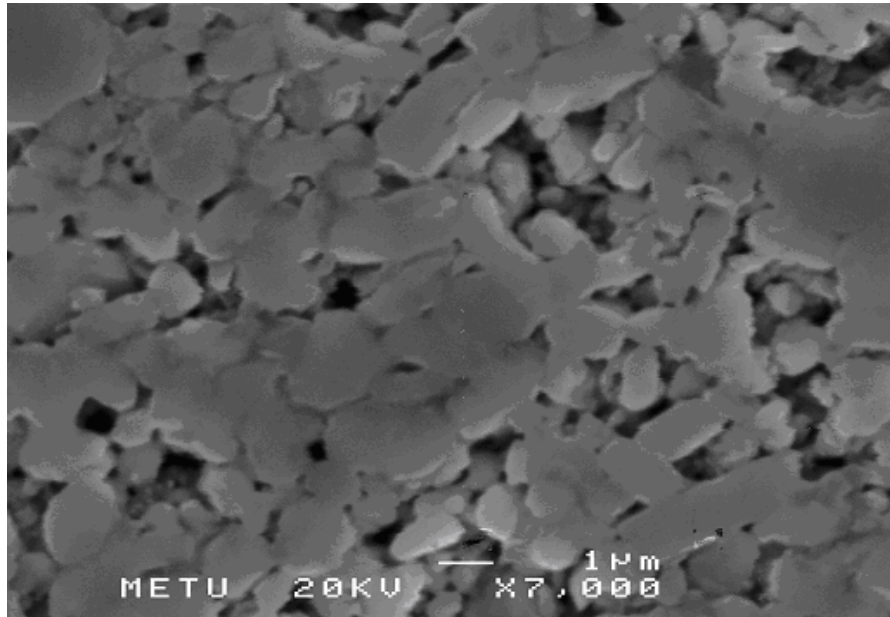
Figure 27 SEM micrograph of $BaTi_{0.5}Fe_{11.33}O_{19}$ ceramic. Sample was soaked at 1250 ^{o}C for 2 hours and etched.

When Ti level was raised to 1.0 mole, a duplex grain structure appeared as shown in Figure 28. The microstructure consisted of rather large grains with interstitial spaces filled by smaller ones. The diagonals of small grains were in the range of 1-3 μm while larger grains measured about 40 μm in size.

For $BaTi_{1.5}Fe_{10}O_{19}$, the small grains in the interstitial sites were grown, however partial duplex grain morphology persisted as seen in Figure 29.
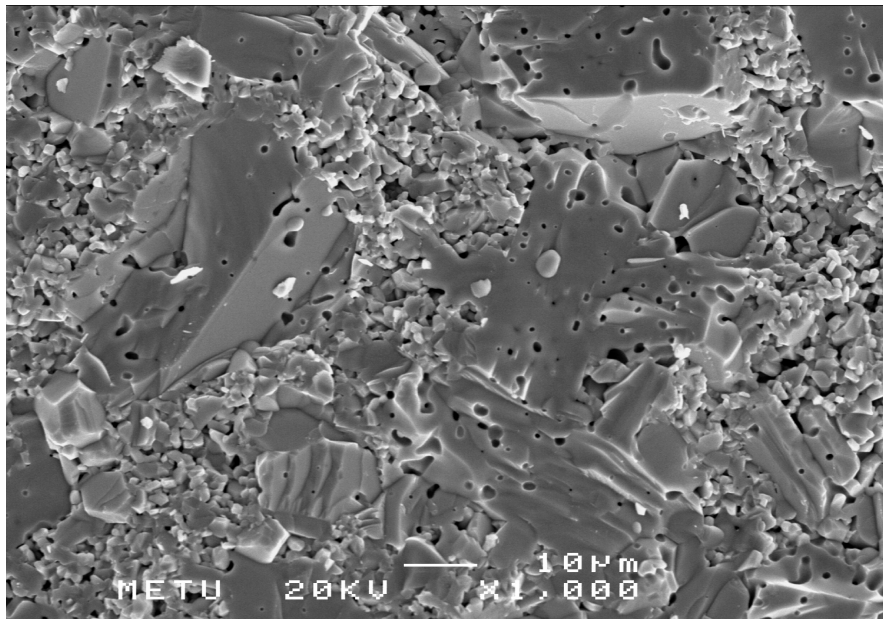
Figure 28 SEM fractograph of $BaTi_{1.0}Fe_{10.67}O_{19}$ ceramic. Sample was soaked at 1250 ^{o}C for 2 hours.
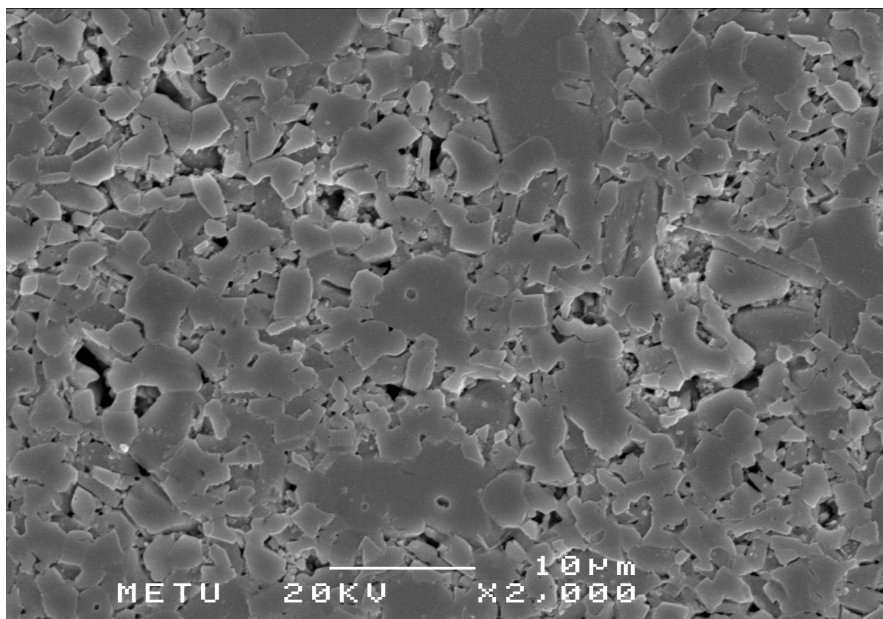
Figure 29 SEM micrograph of $BaTi_{1.5}Fe_{10}O_{19}$ ceramic. Sample was soaked at 1250 ^{o}C for 2 hours and etched.

The grain morphology in the presence of dual additions of Ti and Co, for $BaTi_{0.5}Co_{0.5}Fe_{11}O_{19}$, revealed that the growth in the c-direction was promoted. The large platelet grains grew even larger than 10 µm in size while smaller platelets were filling the spaces formed by larger ones as seen in Figure 30. Majority of grains seemed to be oriented with their c-axis parallel to the plane of the paper.
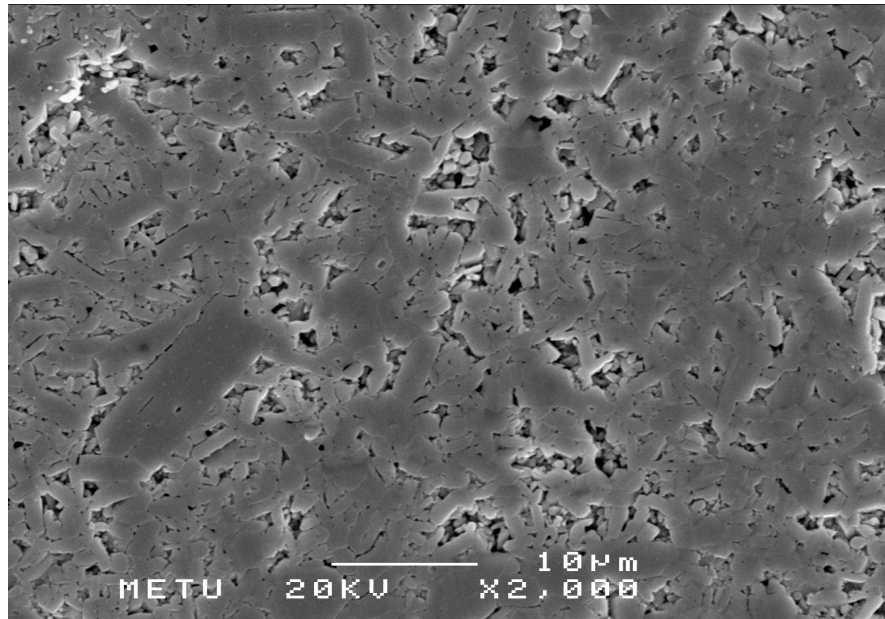
Figure 30 SEM micrograph of $BaTi_{0.5}Co_{0.5}Fe_{11}O_{19}$ ceramic. Sample was soaked at 1250 ^{o}C for 2 hours and etched.

At intermediate concentrations of Ti and Co, in $BaTi_{1.0}Co_{1.0}Fe_{10}O_{19}$, the plates became thicker, and the growth in the basal plane was somehow inhibited as seen in Figure 31. Thick and small platelets of BaHF with no stacking symmetry dominated the microstructure.

When concentrations of Ti and Co were each raised to 1.5 mole, the fragmented grain morphology remained unchanged as shown in Figure 32. The diagonals of the fine grains were smaller than 1 µm. There was an indication of exaggerated grain growth arising possibly from local chemical inhomogeneties.
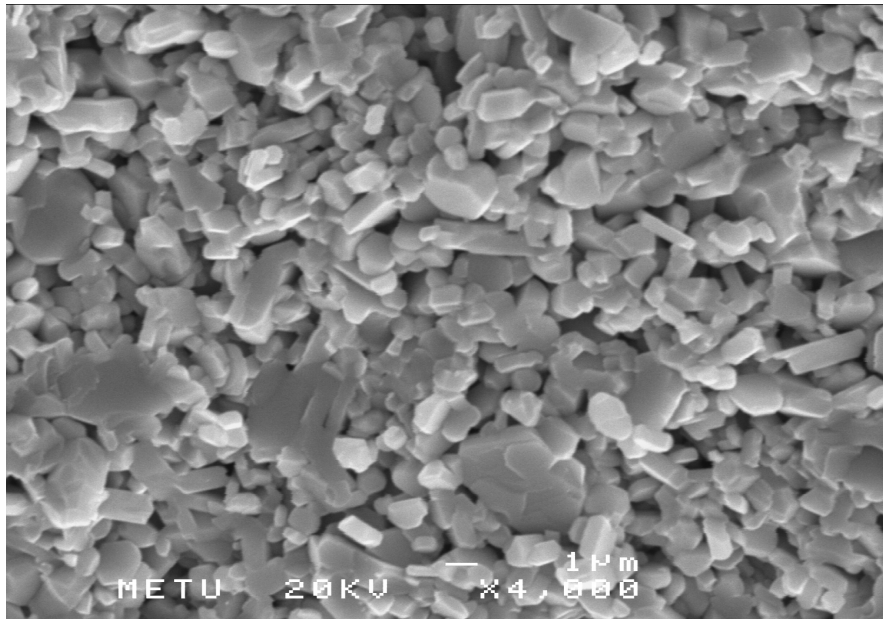
Figure 31 SEM fractograph of BaTi$_{1.0}$Co$_{1.0}$Fe$_{10}$O$_{19}$ ceramic. Sample was soaked at 1250 ^{o}C for 2 hours.
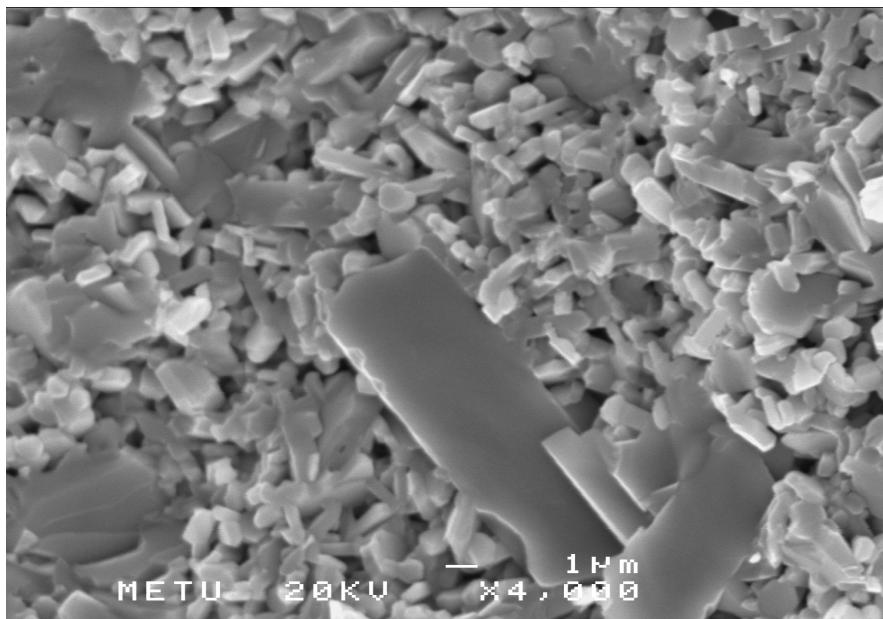
Figure 32 SEM fractograph of BaTi$_{1.5}$Co$_{1.5}$Fe$_9$O$_{19}$ ceramic. Sample was soaked at 1250 ^{o}C for 2 hours.

With prolonged sintering at a given temperature, extending to 8 hours, the grain morphology of the ceramics did not change much. However when soak duration was raised up to 16 hours; tendency towards more equiaxed grains increased.

4.4 Microwave Absorption Properties

4.4.1 Reflection, Transmission Parameters and Microwave Absorption Properties of Ferrites within the X-band

The reflection and transmission coefficients of the sintered ferrite ceramics were obtained with the help of the network analyzer, as described in section 3.3.4. The data on the reflection and transmission coefficients of the samples within the X-band are displayed graphically by the Intensity (dB) versus frequency (GHz) curves shown in Figure 33 through Figure 46.

4.4.1.1 $BaFe_{12}O_{19}$ Ceramic

The response of the undoped BaHF ceramic tile to microwave frequencies in the X-band is represented by the spectral data shown in Figure 33. The upper bunch of curves in full lines describe the reflection characteristics designated as S_{11} and the lower bunch in dotted lines describe transmission characteristics designated as S_{21}.

Each curve corresponds to different soak duration at the peak sintering temperature of 1250 $^{\circ}$C. As seen in Figure 33, the reflection curves did not vary significantly with soak duration; their magnitude remained almost constant at about -5 dB within the X-band meaning that the microwave reflection of BaHF tiles was rather high. Transmission curves showed slight variation with respect to soak duration; the transmission properties of BaHF tiles were not affected greatly by frequency change or processing time. Transmission curves occupied a band spaced between -12 dB to -17 dB.
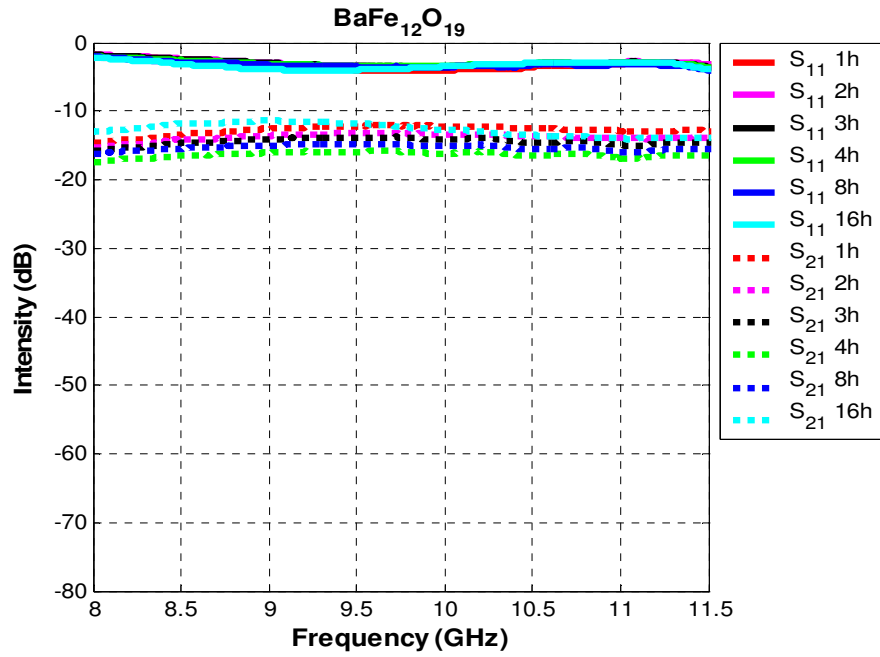
Figure 33 Reflection and transmission coefficients of undoped BaHF ceramics sintered at 1250 $^{\circ}$C for different soak durations.

The absorption characteristics of ferrites were evaluated from the data on transmission and reflection, by using following relationships [50]:

$$R_{dB} = 10 \log P_{\Gamma} \tag{4.4}$$

$$T_{dB} = 10 \log P_{T} \tag{4.5}$$

$$\%Absorption = \left[1 - (P_{\Gamma} + P_{T})\right] \cdot 100 \tag{4.6}$$

where;

R_{dB} : the decibel value of the power reflectivity

T_{dB} : the decibel value of the power transmission

P_{Γ} : power reflectivity ratio relative to the incident power

P_{T} : power transmission ratio relative to the incident power

%Absorption : absorption percentage of the incident wave

Curves in Figure 34 represent the absorption characteristics of undoped BaHF ceramics sintered at 1250 $^{\circ}$C with different soak durations. Within the X-band, absorption increased mildly as the frequency increased from 8 GHz towards 11.5 GHz. The extended soak duration did not have a significant effect on absorption. The maximum absorption was recorded as 55 percent located within the frequency interval 9.5 to 10 GHz.
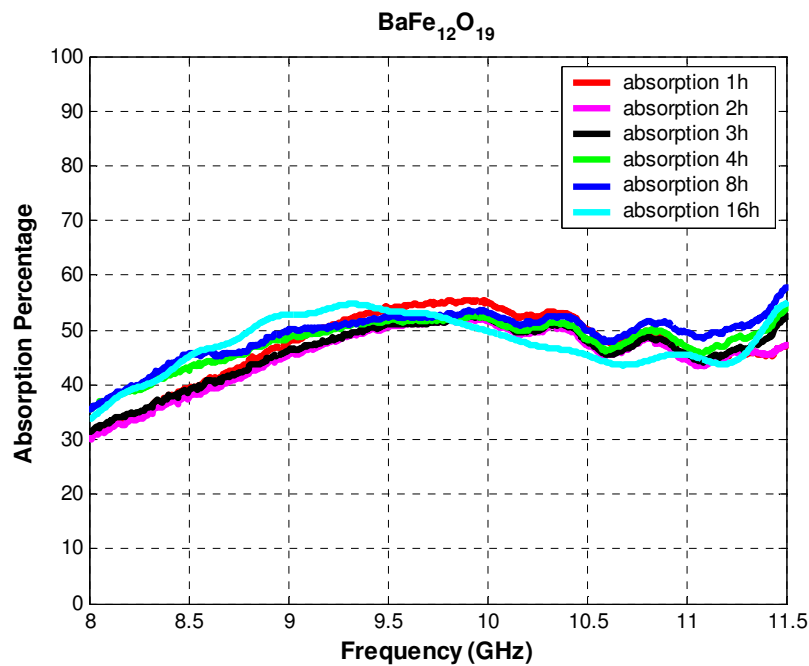
Figure 34 Absorption percentage of undoped BaHF ceramic tiles within the X-band.

4.4.1.2 BaHF Ceramics Doped with Titanium

Figure 35 shows the change in the transmission and reflection curves with respect to frequency for the single substitution of 0.5 mole Ti. In this figure, the reflection curves showed a shallow minima at about 10 GHz with a value of -8 dB meaning that 16 percentage of the incident wave was reflected. The ceramic tiles produced by extended sintering allowed increased transmission of EM waves through the material. The absorption characteristic of this ceramic tile is shown in Figure 36. It

was seen that Ti addition on 0.5 mole level raised the microwave absorption at about 10 GHz to 61 percent as opposed to the 55 percent absorption recorded in the undoped BaHF.
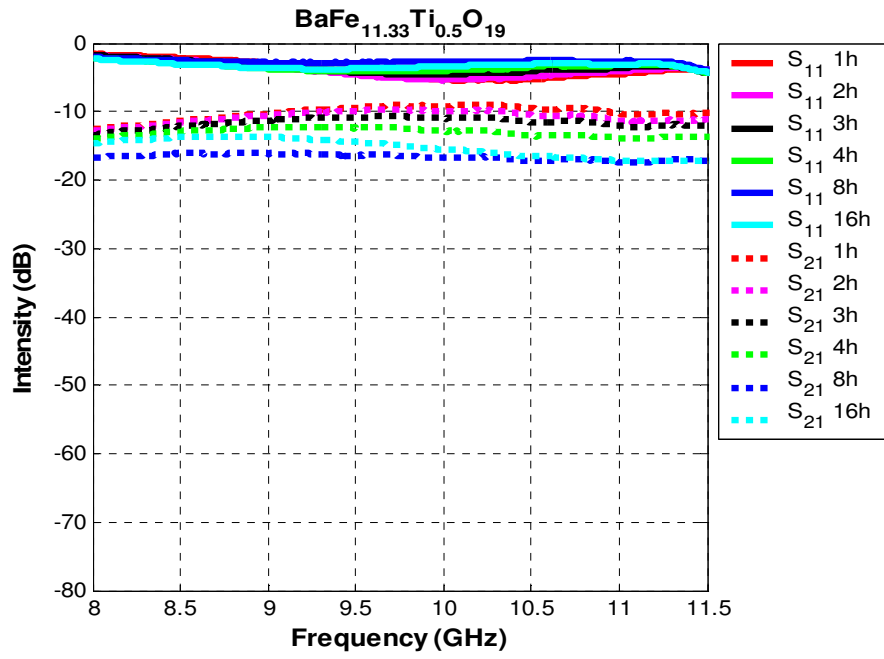
Figure 35 Reflection and transmission coefficients of 0.5 mole Ti doped BaHF ceramics sintered at 1250 $^{\circ}$C for different soak durations.
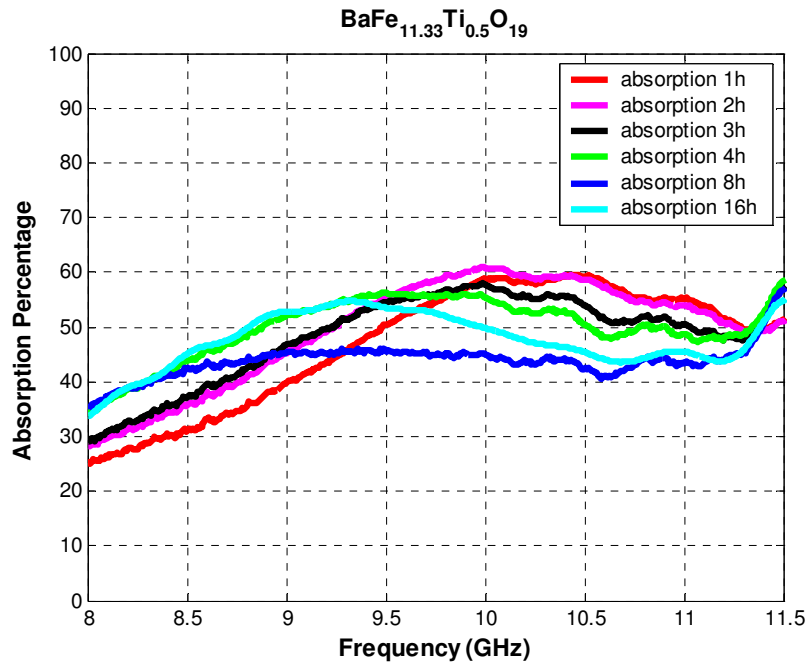
Figure 36 Absorption percentage of $BaFe_{11.33}Ti_{0.5}O_{19}$ ceramic tiles within the X-band.

The reflection and transmission characteristics of BaHF ceramic with one mole of Ti replacement are displayed in Figure 37. In tiles prepared with different soak durations the reflected portion of the EM wave was at its highest level. Exception was the tile soaked for 16 hours. According to Figure 38, the tiles sintered up to 8 hours of soaking time exhibited very poor microwave absorption characteristics. The absorption behavior recovered partially with extended sintering, approaching that of undoped BaHF towards 16 hours of soaking period.
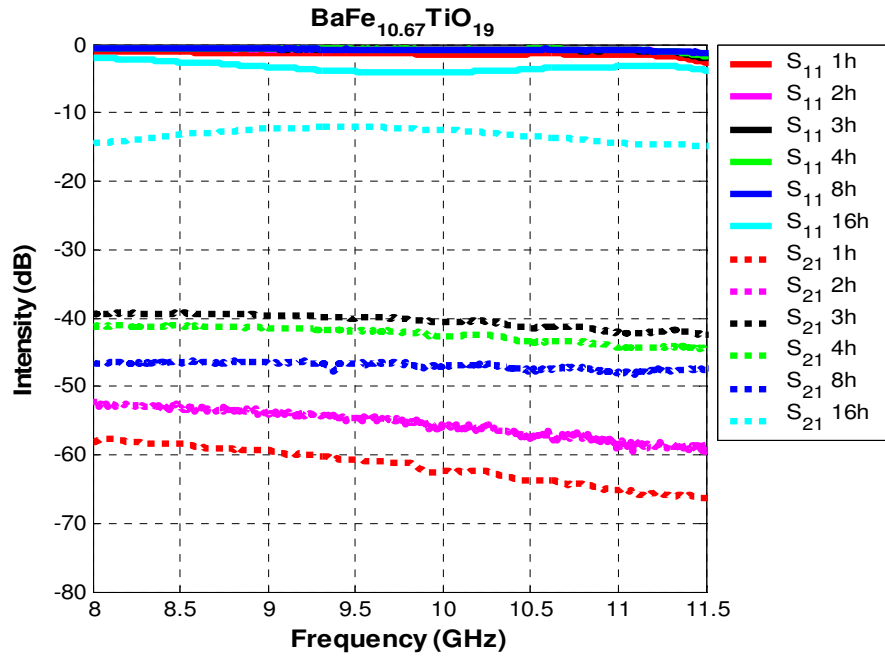
Figure 37 Reflection and transmission coefficients of 1.0 mole Ti doped BaHF ceramics sintered at 1250 ^{o}C for different soak durations.
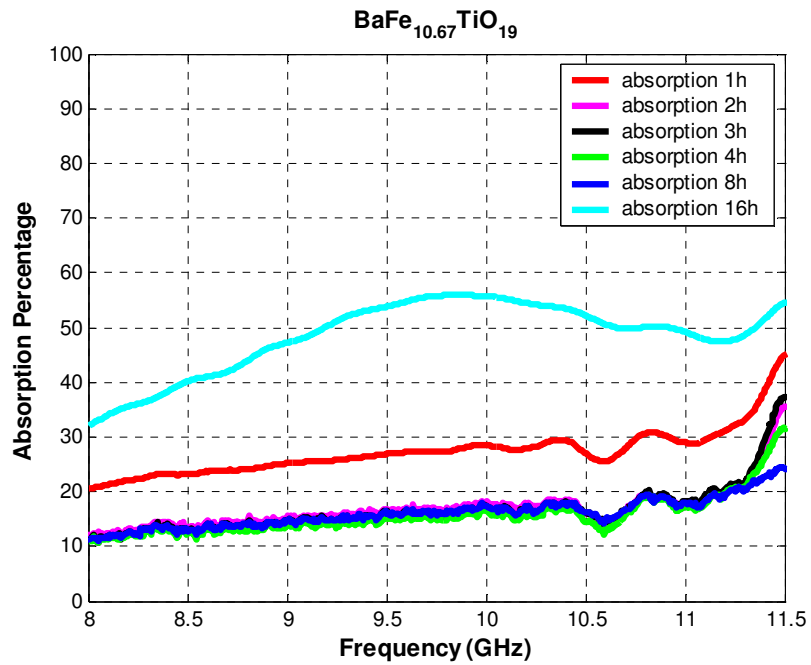
Figure 38 Absorption percentage of BaFe$_{10.67}$TiO$_{19}$ ceramic tiles within the X-band.

Increased Ti substitution caused further deterioration in the microwave absorbance of the ceramic as evidenced by the curves in Figure 39 and Figure 40. The ceramic tile manufactured with 1.5 Ti substitution absorbed only a small fraction of the incident EM wave. The improvement on absorbance by prolonged sintering was not so significant.
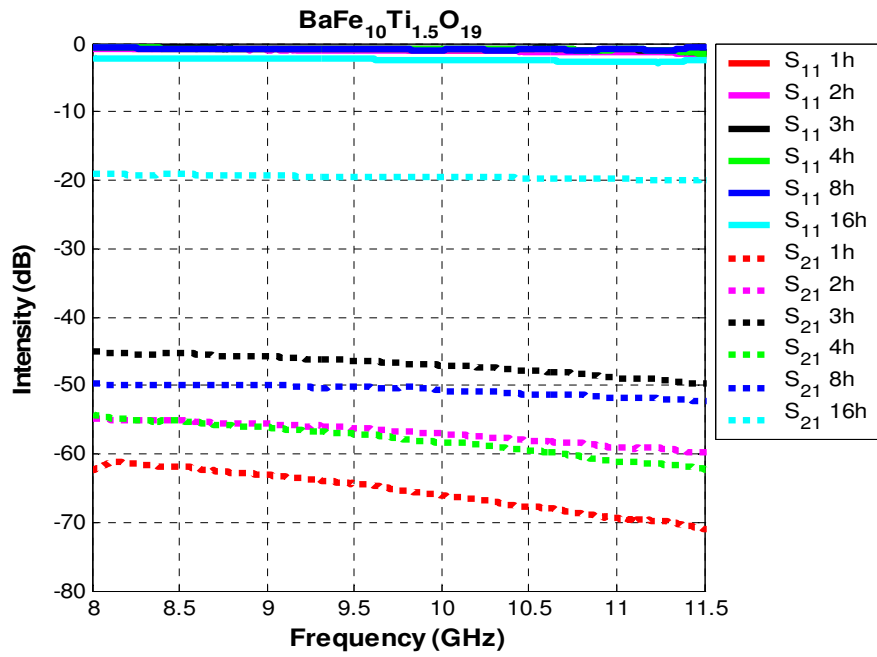

Figure 39 Reflection and transmission coefficients of 1.5 mole Ti doped BaHF ceramics sintered at 1250 ^{o}C for different soak durations.
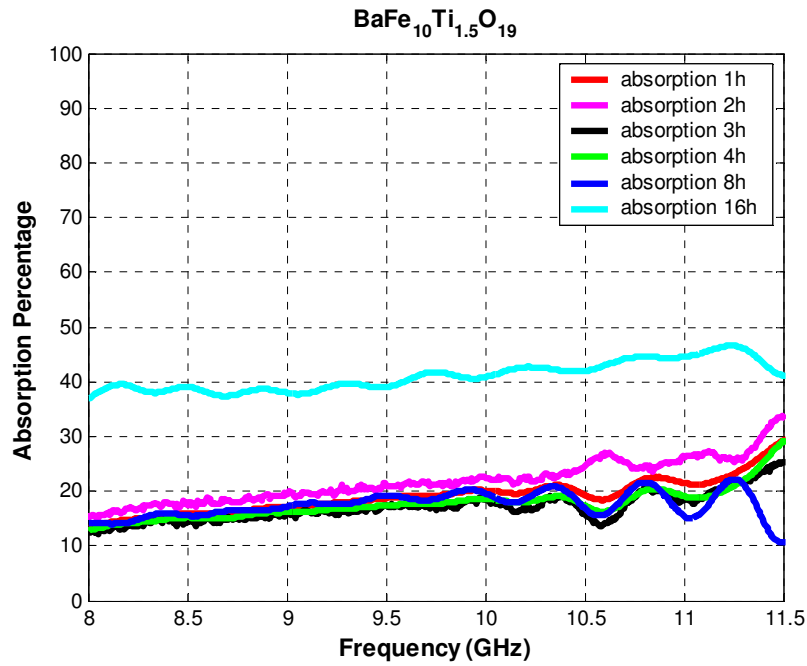
Figure 40 Absorption percentage of $BaFe_{10}Ti_{1.5}O_{19}$ ceramic tiles within the X-band.

4.4.1.3 BaHF Ceramics Doped with Titanium and Cobalt

Figure 41 shows the variation in the reflection and transmission coefficients with frequency for $BaFe_{11}Ti_{0.5}Co_{0.5}O_{19}$ ceramic. It was noted that the reflection spectra of ceramic tiles manufactured with $Ti_{0.5}Co_{0.5}$ dual substitution exhibited a minimum in the central part of the diagram at about 9.7 GHz frequency. Hence Co was effective in attenuating the reflectivity. The minima in the reflectance curve shifted to lower frequencies with prolonged sintering. On the other hand, transmittance displayed a reverse behavior; it became very high in the central part of the frequency axis.

The overall absorption properties of this ferrite are shown in Figure 42. Although there was a drop in reflectance, absorption was low due to increase in transmittance.
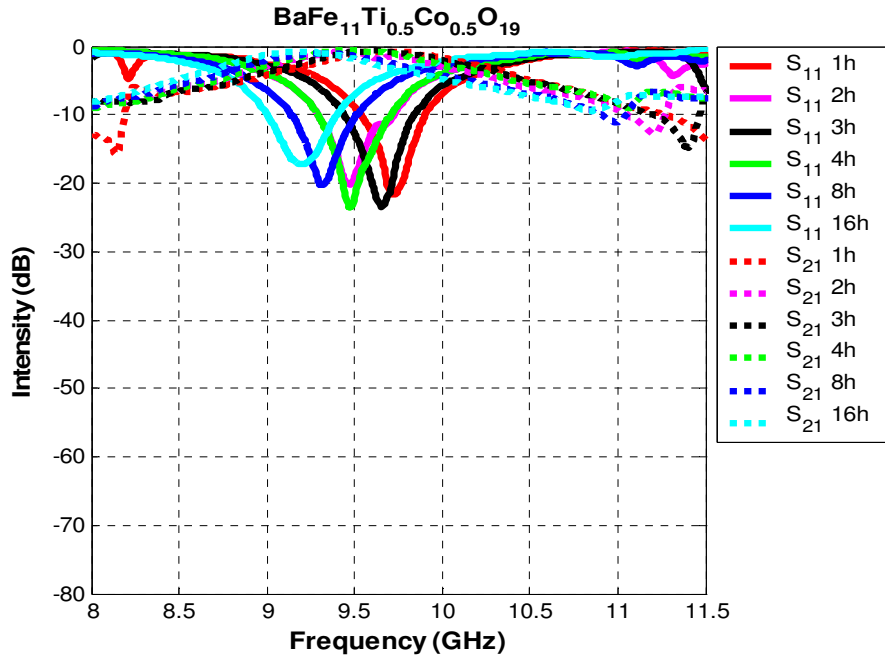
Figure 41 Reflection and transmission coefficients of 0.5 mole Ti and 0.5 mole Co doped BaHF ceramics sintered at 1250 ^{o}C for different soak durations.
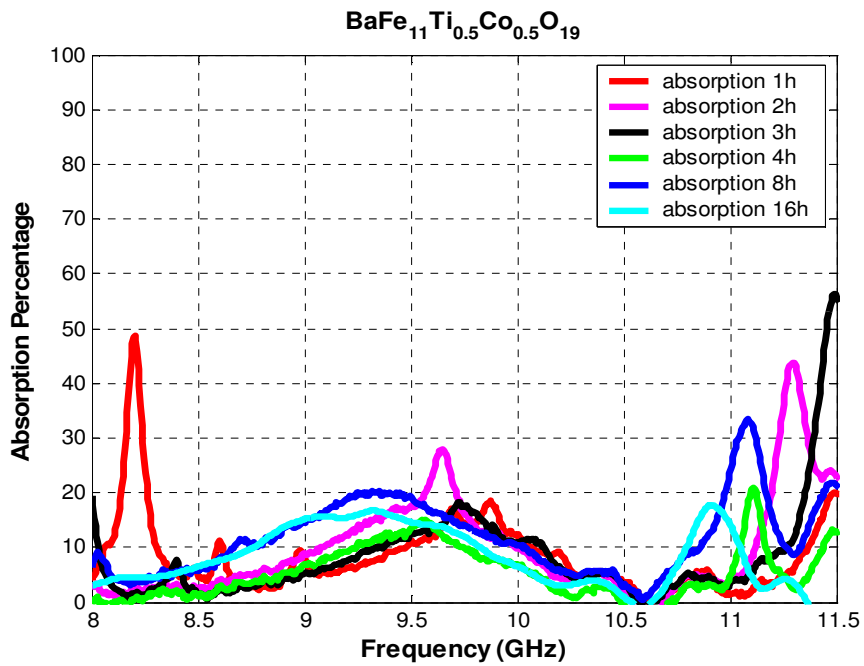
Figure 42 Absorption percentage of $BaFe_{11}Ti_{0.5}Co_{0.5}O_{19}$ ceramic tiles within the X-band.

Dual additions of Ti and Co each at 1.0 mole level resulted in reflection and transmission characteristics shown in Figure 43. Reflectance was practically unaffected by changes in soak duration but considerable spread could be observed in transmittance. According to Figure 44, absorption of the incident wave varied between 40 to 60 percent; the average being about 48 percent.

When doping level with Ti and Co was raised to 1.5, reflectance remained high and transmittance was also high as seen in Figure 45. Absorption percentage of the incident wave dropped to an average of about 40 percent as shown in Figure 46.
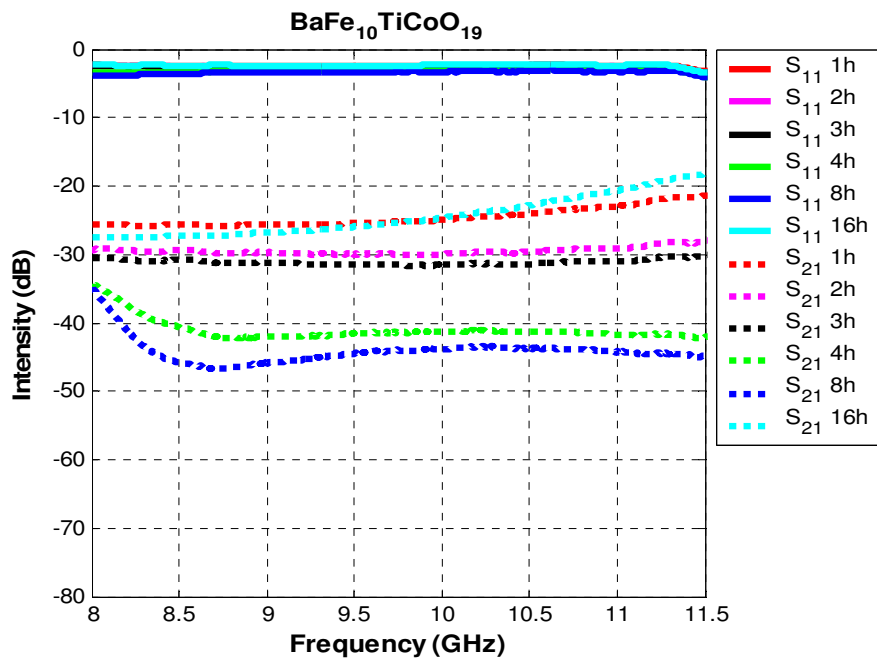
Figure 43 Reflection and transmission coefficients of 1.0 mole Ti and 1.0 mole Co doped BaHF ceramics sintered at 1250 ^{o}C for different soak durations.
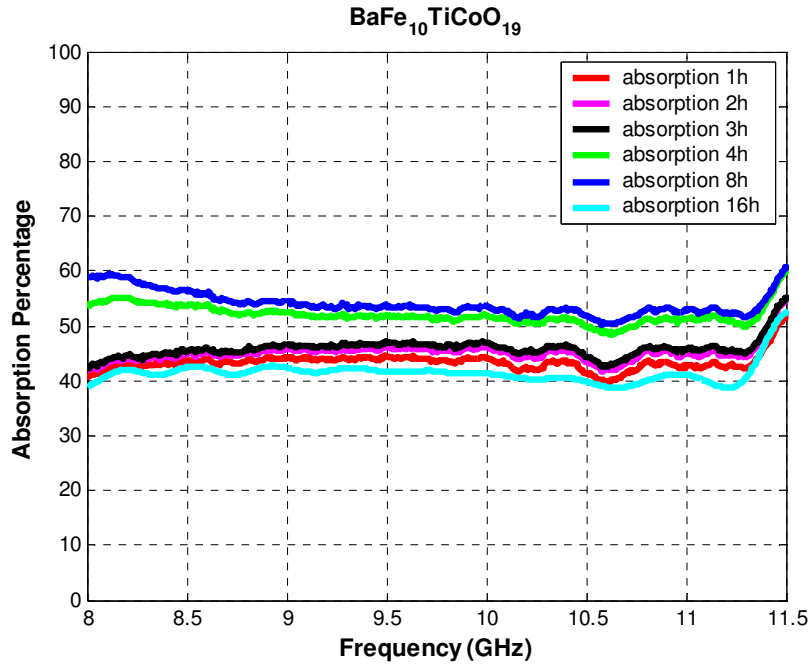
Figure 44 Absorption percentage of $BaFe_{10}TiCoO_{19}$ ceramic tiles within the X-band.
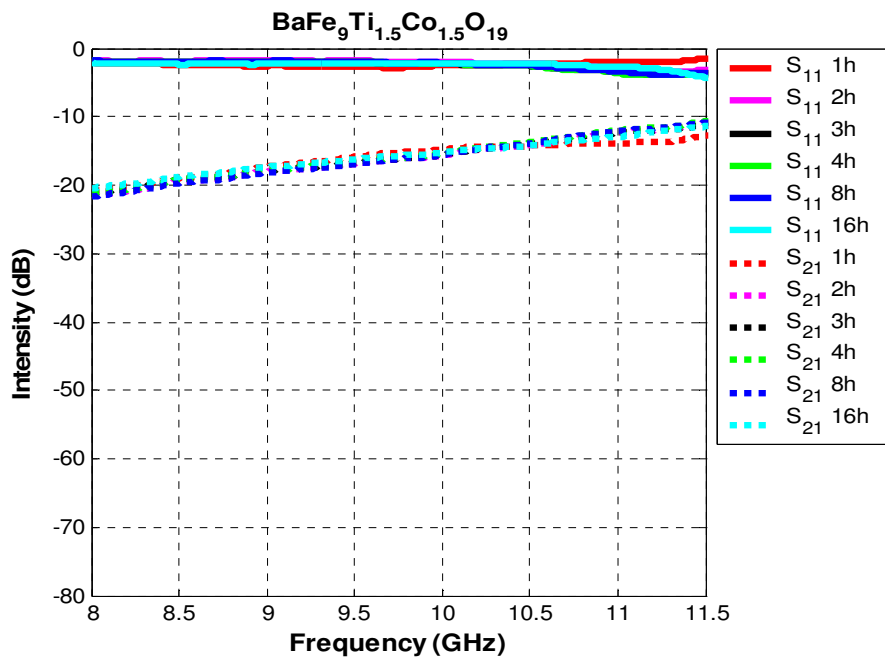

Figure 45 Reflection and transmission coefficients of 1.5 mole Ti and 1.5 mole Co doped BaHF ceramics sintered at 1250 ^{o}C for different soak durations.
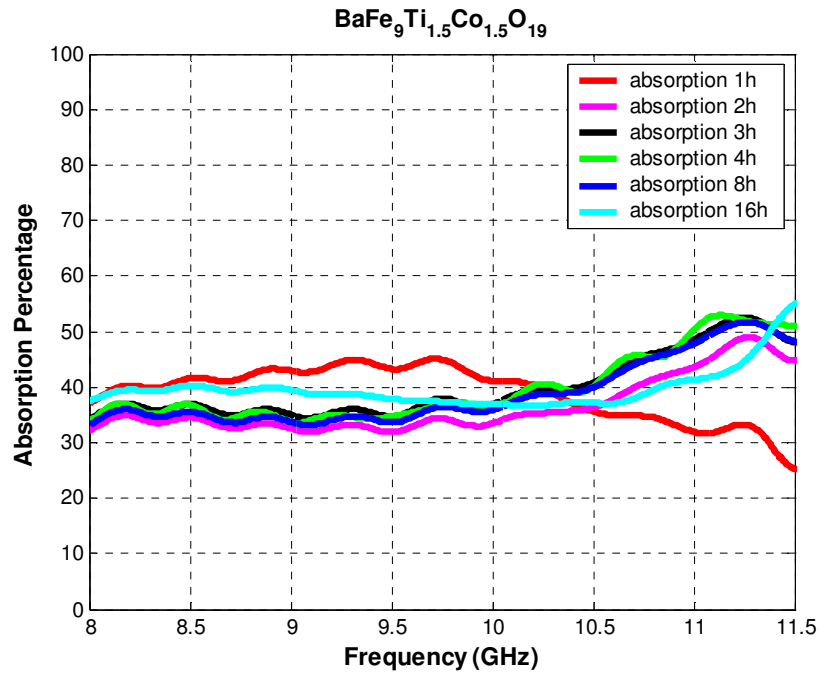
Figure 46 Absorption percentage of the $BaFe_9Ti_{1.5}Co_{1.5}O_{19}$ ceramic tiles within the X-band.

4.4.2 Reflection, Transmission Parameters and Microwave Absorption Properties of Ferrites within the Ku-band

Data on the reflection and transmission coefficients of BaHF ceramics obtained in the Ku-band frequencies displayed graphically in Figure 47 through Figure 60. The measurements were confined to the ceramics sintered at 1250 ^{o}C for soak durations of 2, 8 and 16 hours.

With the exception of the ferrite with composition $BaFe_{11}Ti_{0.5}Co_{0.5}O_{19}$ the curves showing reflection characteristics were essentially the extension of those obtained in the X-band. Disregarding the minor fluctuations the reflectance of all ceramics was high and remained virtually unaffected by changes in frequency.

In BaHF ceramics which contained 0.5 mole Ti and 0.5 mole Co as co-dopants, the reflectance was distinctly lowered at 13 GHz frequency. However, this did not

increase the absorbance, the loss in reflectance at this frequency was rather compensated by a rise in transmittance.

Within the Ku-band all BaHF ceramics exhibited rather shallow absorption characteristics. In general, the proportion of the absorbed incident EM wave ranged from 30 percent to an upper limit of 65 percent.
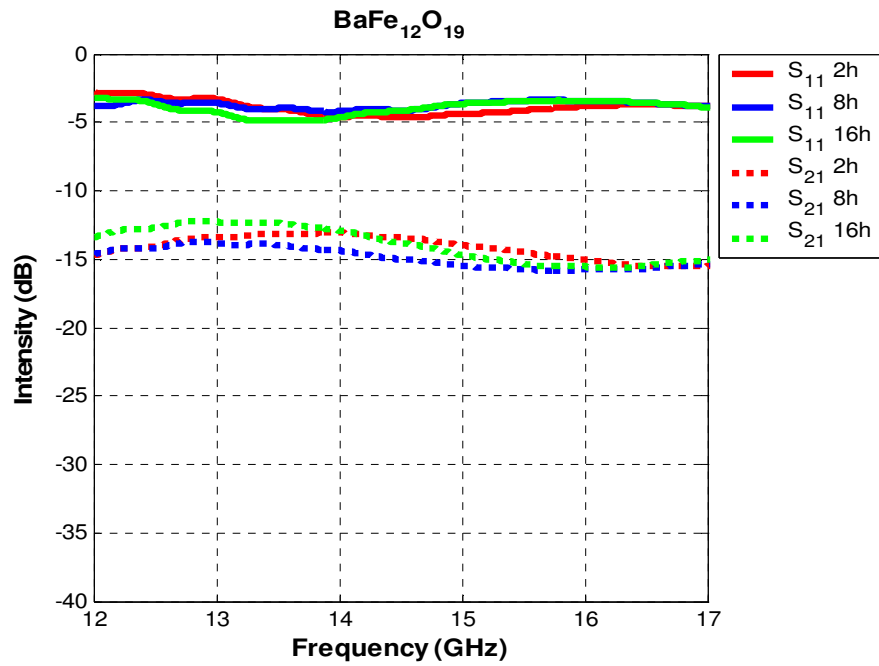
Figure 47 Reflection and transmission coefficients of undoped BaHF ceramics sintered at 1250 ^{o}C for different soak durations.
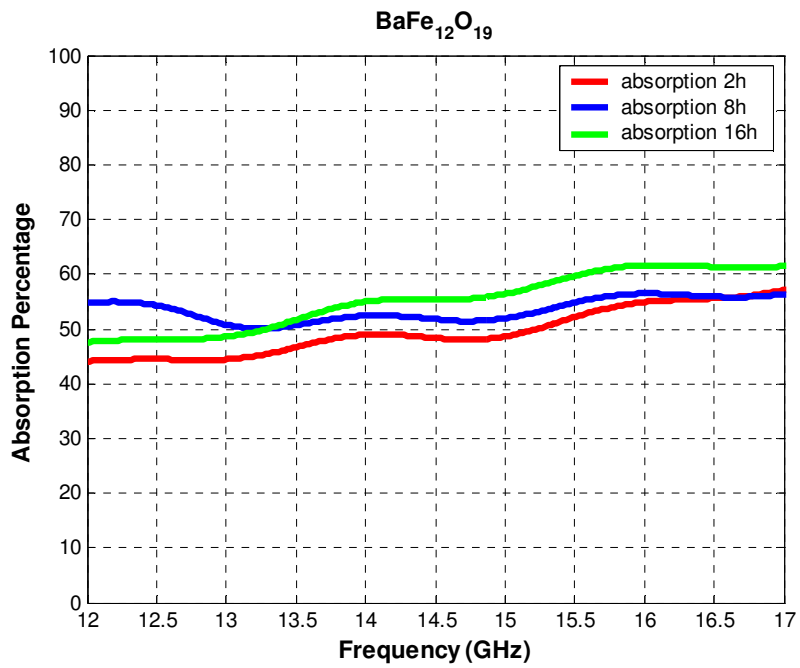
Figure 48 Absorption percentage of $BaFe_{12}O_{19}$ ceramic tiles within Ku-band.
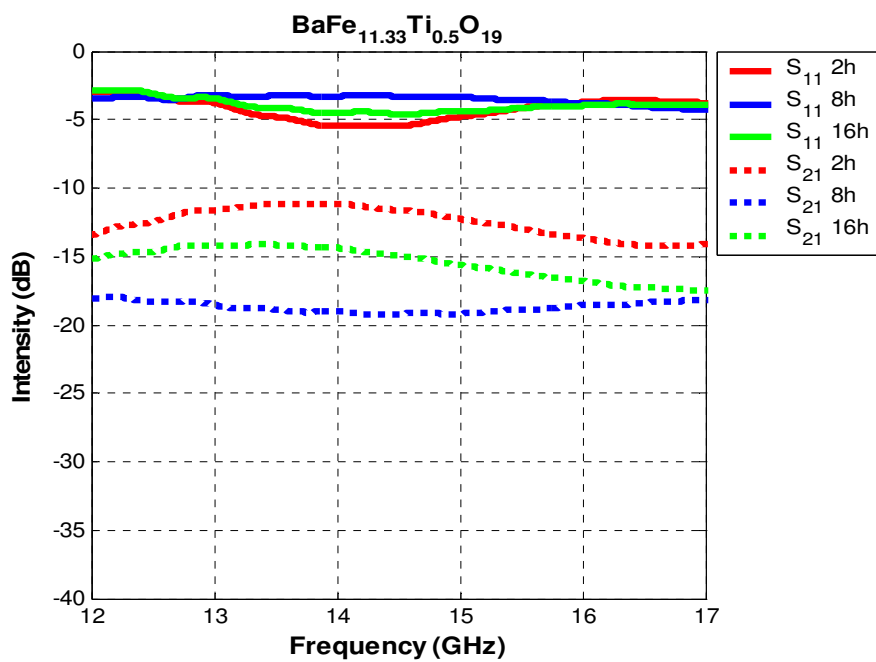
**Figure 49** Reflection and transmission coefficients of 0.5 mole Ti doped BaHF ceramics sintered at 1250 ^oC for different soak durations.
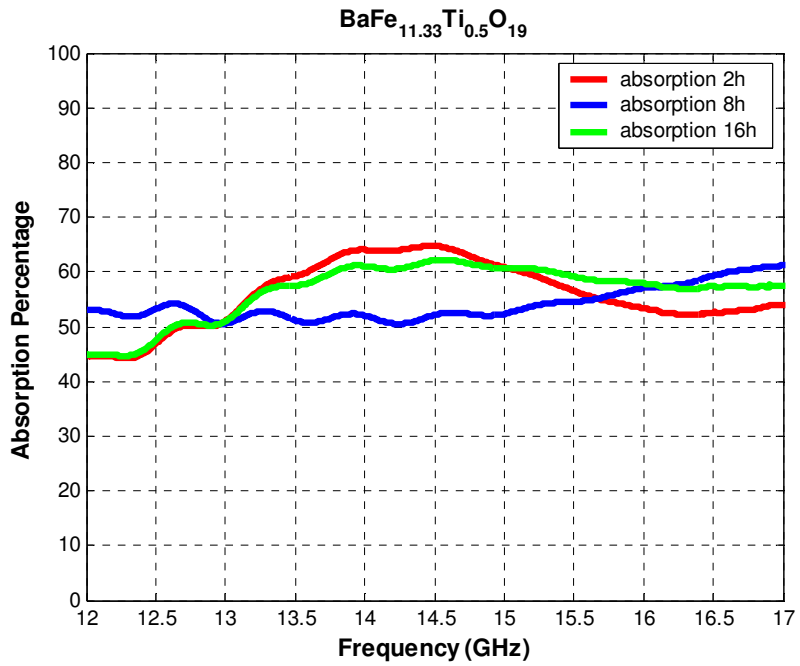
Figure 50 Absorption percentage of $BaFe_{11.33}Ti_{0.5}O_{19}$ ceramic tiles within the Ku-band.
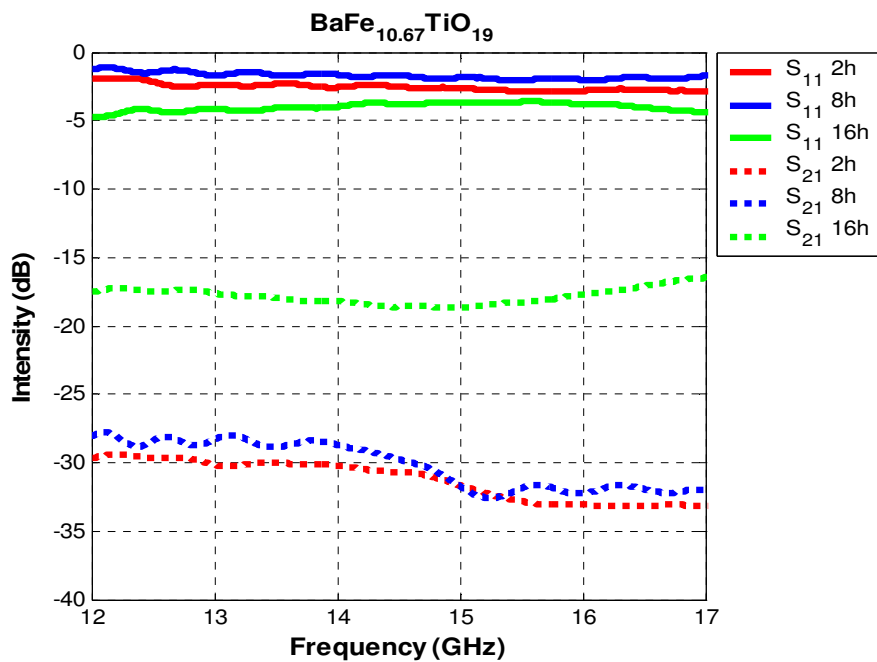
Figure 51 Reflection and transmission coefficients of 1.0 mole Ti doped BaHF ceramics sintered at 1250 ^{o}C for different soak durations.
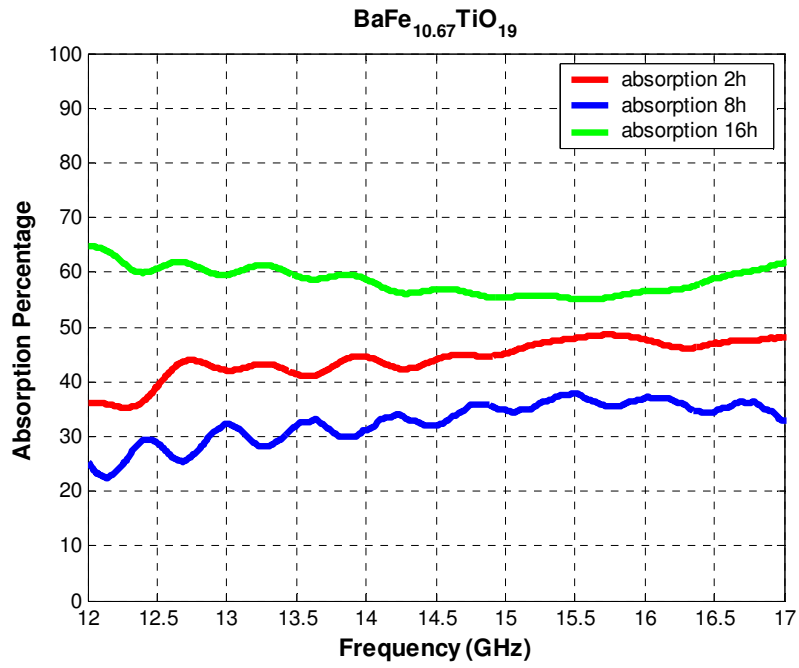
Figure 52 Absorption percentage of $BaFe_{10.67}TiO_{19}$ ceramic tiles within the Ku-band.
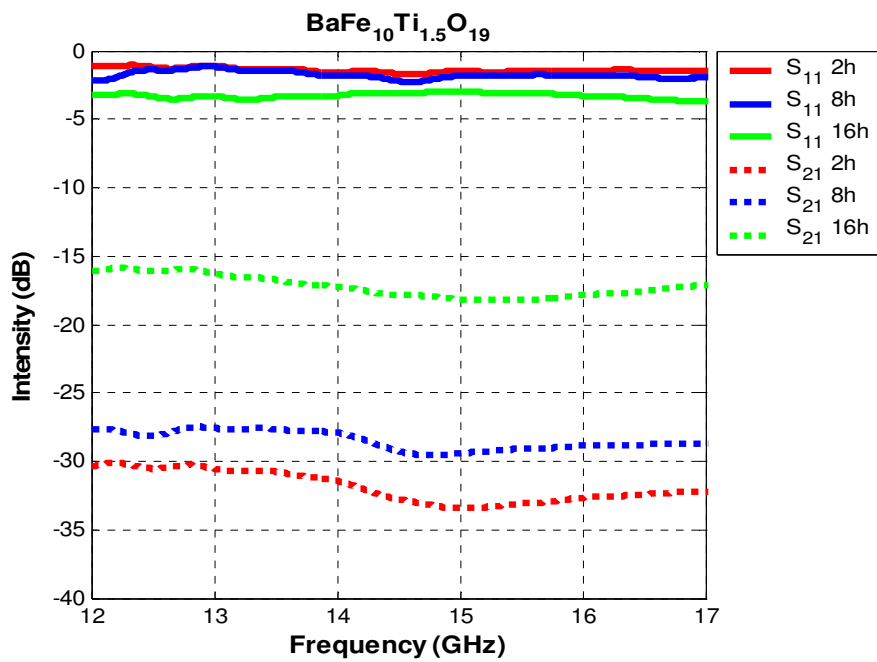

Figure 53 Reflection and transmission coefficients of 1.5 mole Ti doped BaHF ceramics sintered at 1250 ^{o}C for different soak durations.
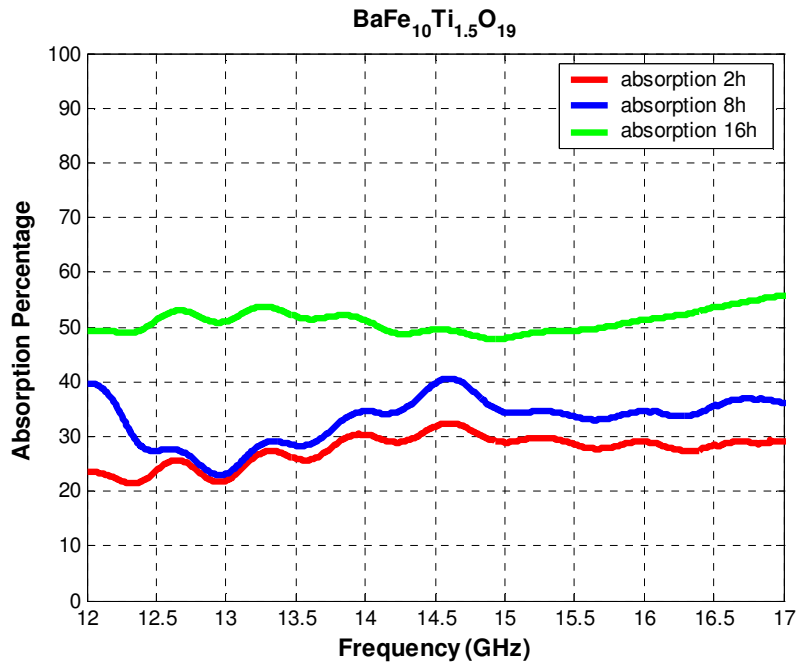
Figure 54 Absorption percentage of $BaFe_{10}Ti_{1.5}O_{19}$ ceramic tiles within the Ku-band.
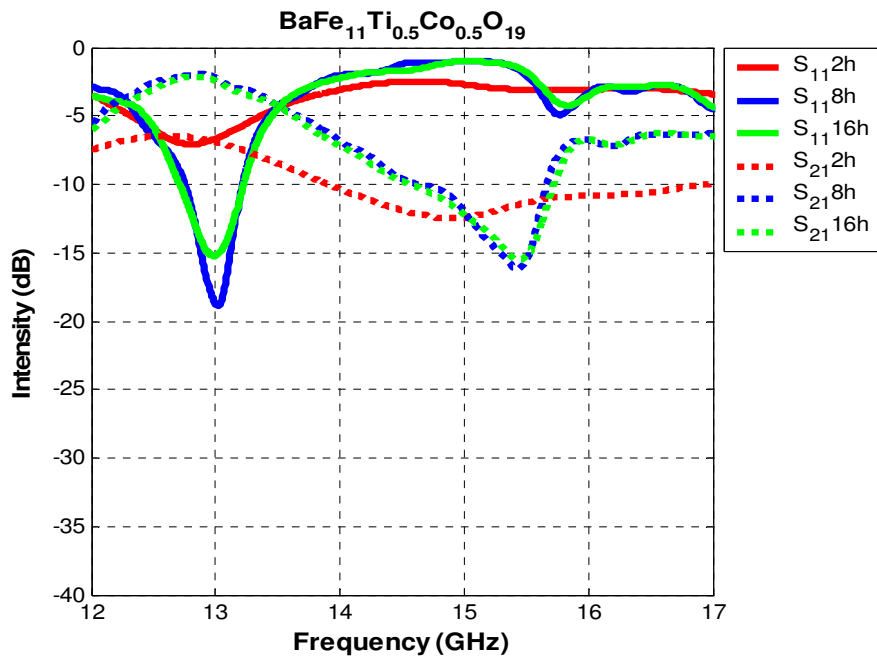
Figure 55 Reflection and transmission coefficients of 0.5 mole Ti and 0.5 mole Co doped BaHF ceramics sintered at 1250 ^{o}C for different soak durations.
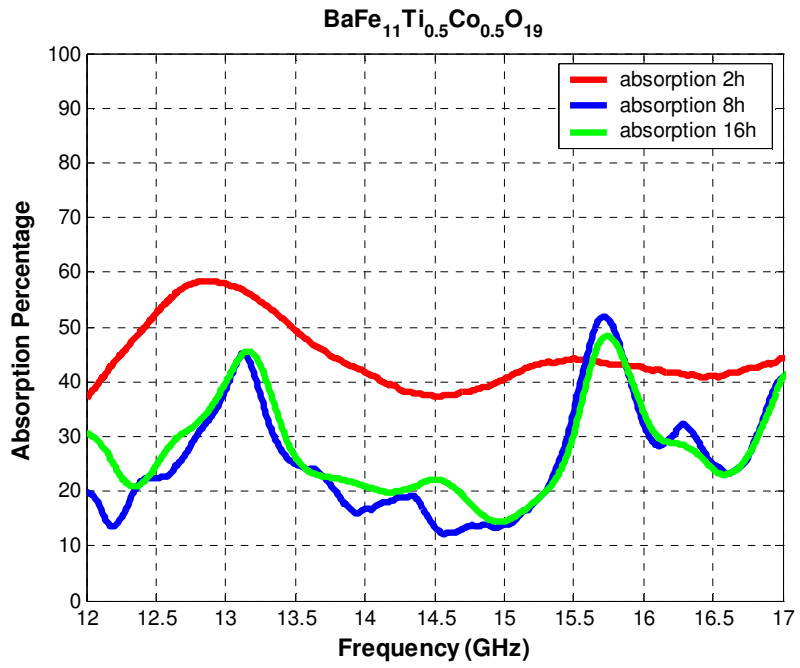
Figure 56 Absorption percentage of $BaFe_{11}Ti_{0.5}Co_{0.5}O_{19}$ ceramic tiles within the Ku-band.
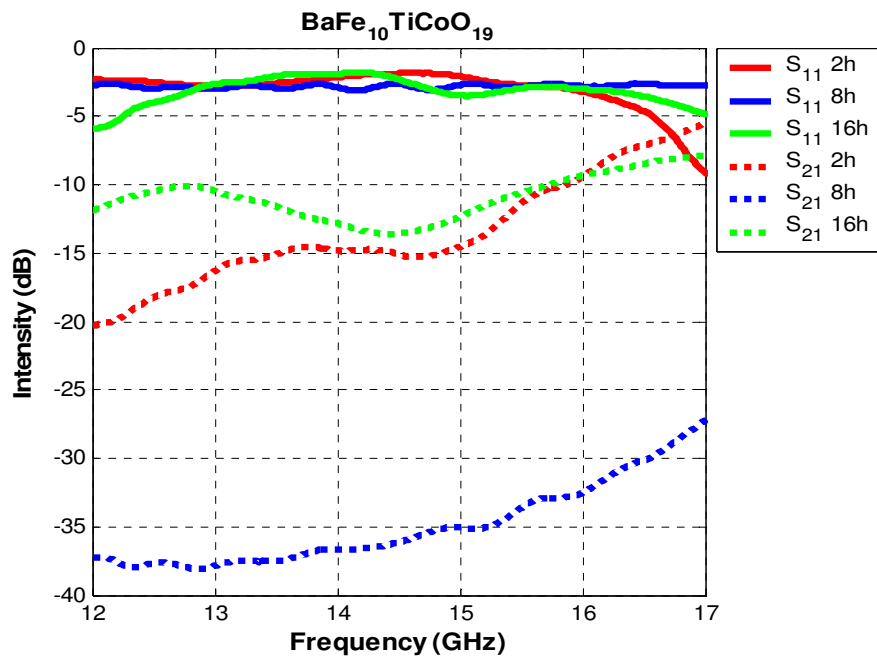
Figure 57 Reflection and transmission coefficients of 1.0 mole Ti and 1.0 mole Co doped BaHF ceramics sintered at 1250 ^{o}C for different soak durations.
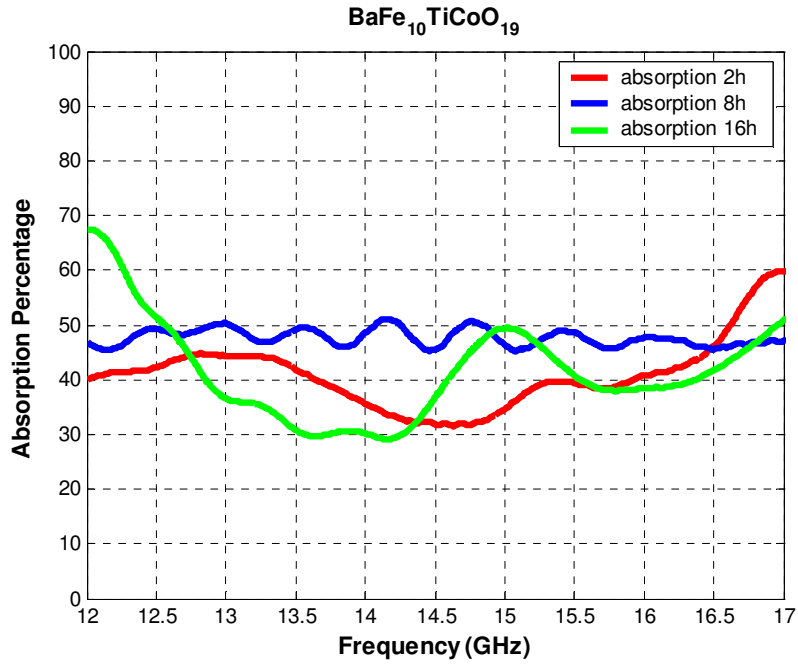
Figure 58 Absorption percentage of $BaFe_{10}TiCoO_{19}$ ceramic tiles within the Ku-band.
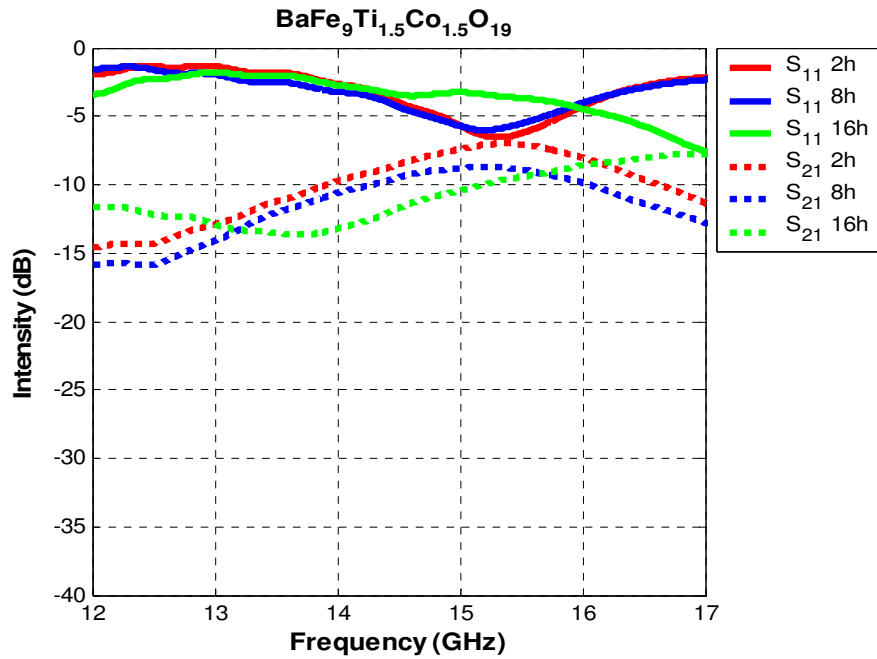
**Figure 59** Reflection and transmission coefficients of 1.5 mole Ti and 1.5 mole Co doped BaHF ceramics sintered at 1250 ^{o}C for different soak durations.
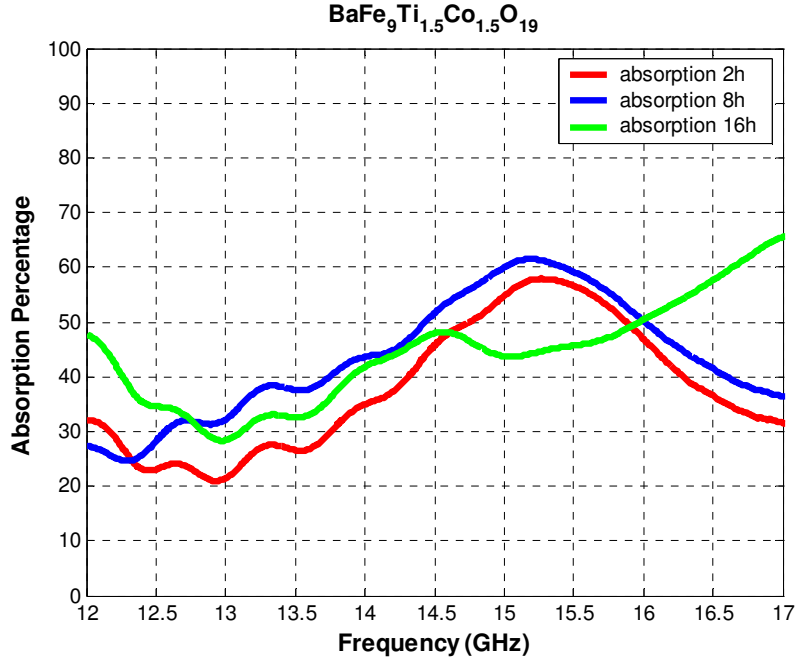
Figure 60 Absorption percentage of $BaFe_9Ti_{1.5}Co_{1.5}O_{19}$ ceramic tiles within the Ku-band.

4.4.3 Complex Permittivity and Complex Permeability Data within X and Ku Bands

Data on the reflection and transmission coefficients were used to calculate the complex dielectric constant ε and magnetic permeability μ of the ceramic tiles, using the expressions developed by Weir [9]. For this purpose, data gathered from the network analyzer were processed in the Matlab program.

Referring to Weir's formulas; ε and μ were defined in terms of their real and imaginary parts as follows:

$$\varepsilon = \varepsilon_r \, \varepsilon_0 = (\varepsilon_r^{'} - j\varepsilon_r^{''})\varepsilon_0 \tag{4.7}$$

$$\mu = \mu_r \, \mu_0 = (\mu_r^{'} - j\mu_r^{''})\mu_0 \tag{4.8}$$

Initially, the reflection coefficient (Γ) at the air-sample interface was found from;

$$\Gamma = X \pm \sqrt{X^2 - 1} \qquad (\Gamma \leq 1)$$
(4.9)

where;

$$X = \frac{S_{11}^2 - S_{21}^2 + 1}{2S_{11}}$$
(4.10)

In the Equation (4.10);

S_{11} is the complex reflection coefficient

S_{21} is the complex transmission coefficient

Then, the complex propagation factor P was calculated from the relationship;

$$P = \frac{S_{11} + S_{21} - \Gamma}{1 - (S_{11} + S_{21})\Gamma}$$
(4.11)

After determining P and Γ, complex magnetic permeability μ_r was obtained by the combinaton of following expressions:

$$\frac{1}{\Lambda^2} = -\left[\frac{1}{2\pi l}\ln\left(\frac{1}{P}\right)\right]^2$$
(4.12)

$$\mu_r = \frac{1 + \Gamma}{\Lambda(1 - \Gamma)\sqrt{\dfrac{1}{\lambda_0^2} - \dfrac{1}{\lambda_c^2}}}$$
(4.13)

where;

l is the thickness of the ceramic tile, in meter

Λ is a constant

λ_0 free space wavelength, in meter

λ_c cut off wavelength (2 times of the largest waveguide dimension), in meter

The complex dielectric permittivity ε_r was evaluated from the expression,

$$\frac{1}{\Lambda^2} = \left(\frac{\varepsilon_r \mu_r}{\lambda_0^2} - \frac{1}{\lambda_c^2} \right) \tag{4.14}$$

The data generated on the real and imaginary parts of the complex permeability and complex permittivity are displayed graphically by the curves shown in Figure 61 through Figure 88. When the curves related to magnetic permeability are examined, it should be noted that in all ferrites the complex part of the permeability was always a finite non-zero quantity. This should be taken to mean that all of the ceramic tiles were magnetically lossy, which is a desirable feature in a good RAM. However, this advantage was offset by the rather high magnitudes of the dielectric permittivity. A comprehensive treatment of the results on dielectric permittivity and magnetic permeability will be provided in the next chapter.
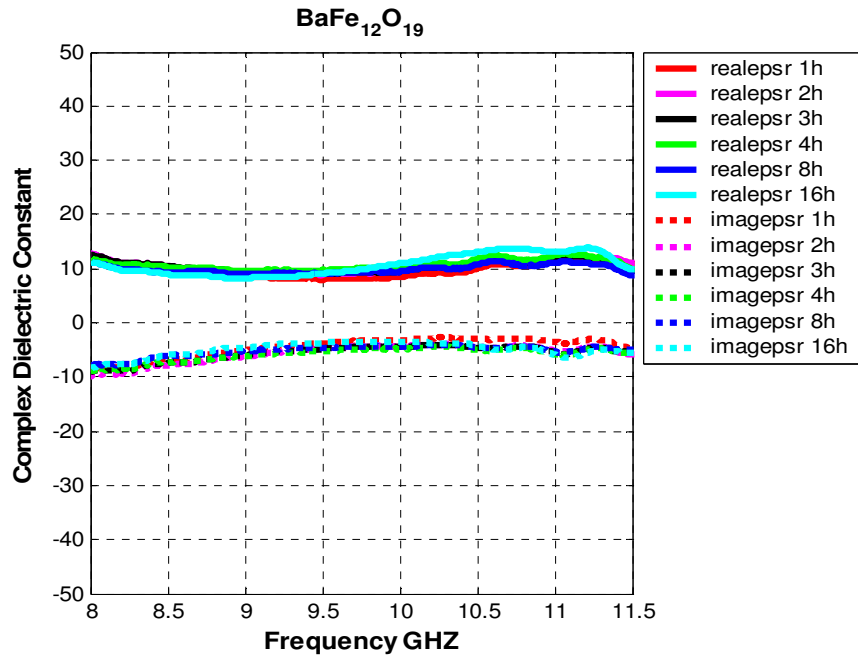
Figure 61 Variation of the real and imaginary parts of the complex permittivity with respect to frequency for $BaFe_{12}O_{19}$ ceramics within the X-band.
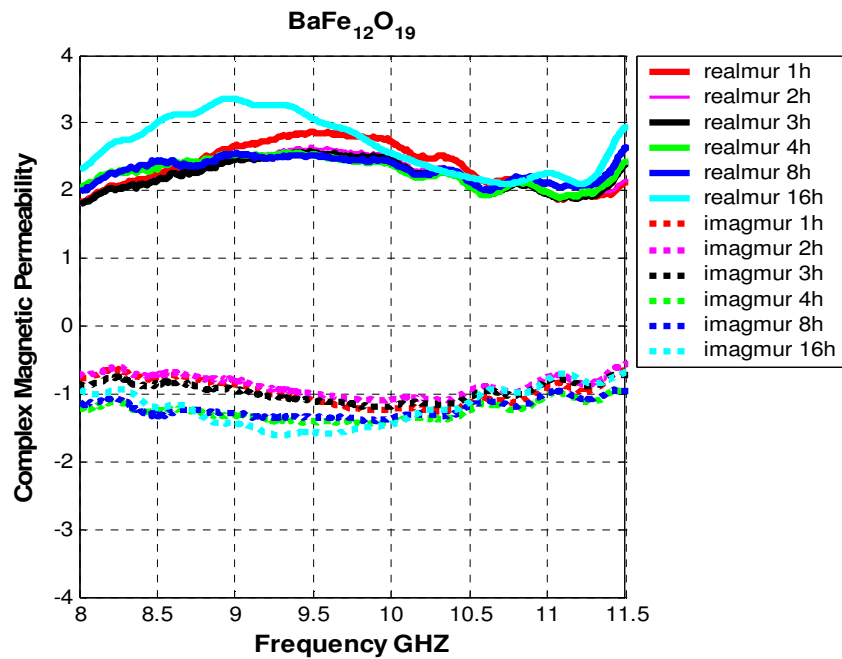
Figure 62 Variation of the real and imaginary parts of the complex permeability with respect to frequency for $BaFe_{12}O_{19}$ ceramics within the X-band.
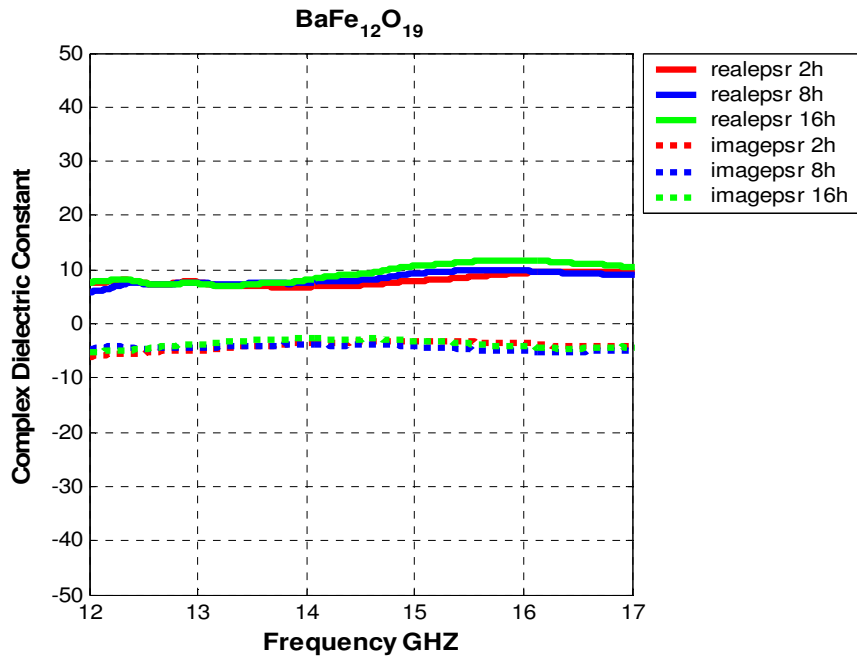
Figure 63 Variation of the real and imaginary parts of the complex permittivity with respect to frequency for $BaFe_{12}O_{19}$ ceramics within the Ku-band.
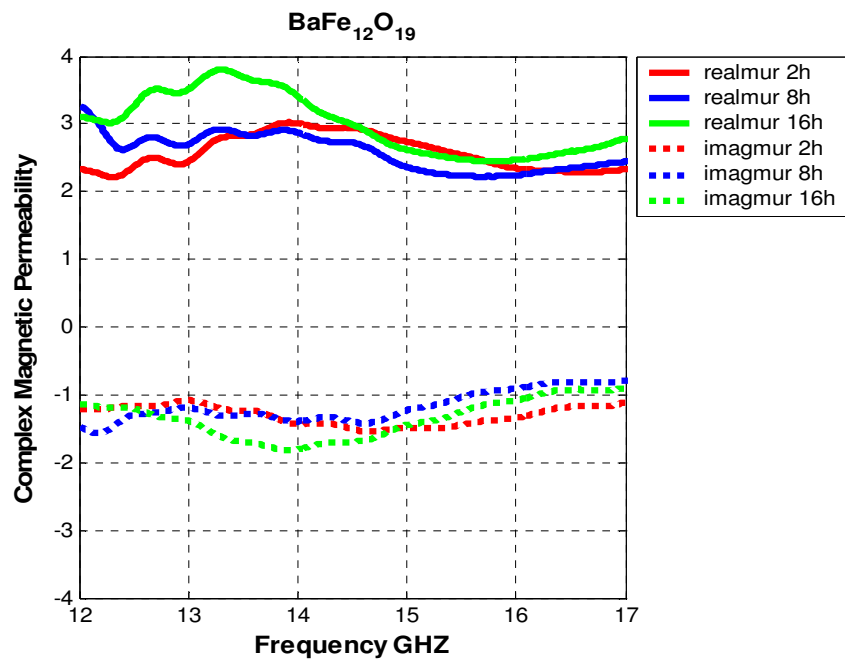
Figure 64 Variation of the real and imaginary parts of the complex permeability with respect to frequency for $BaFe_{12}O_{19}$ ceramics within the Ku-band.
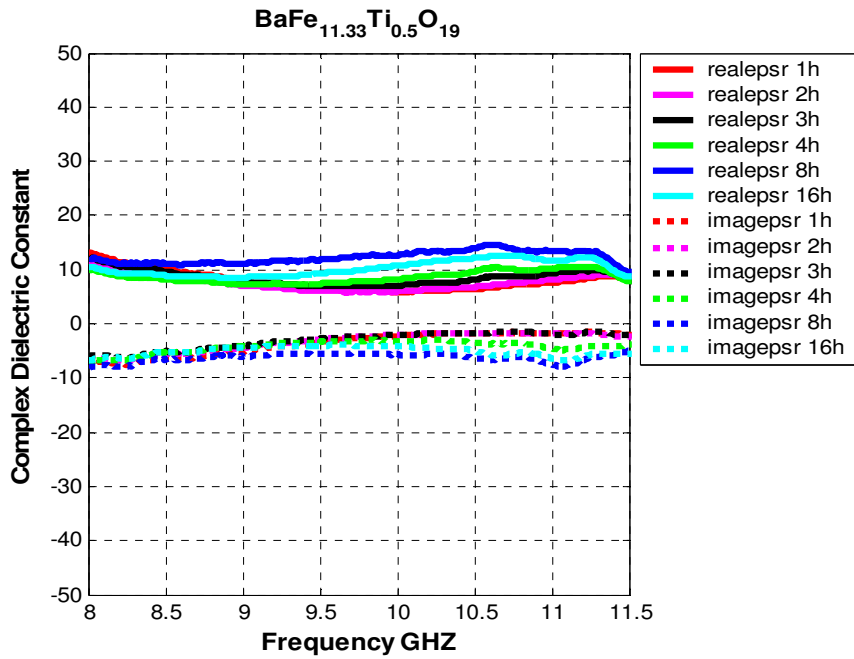
Figure 65 Variation of the real and imaginary parts of the complex permittivity with respect to frequency for $BaFe_{11.33}Ti_{0.5}O_{19}$ ceramics within the X-band.
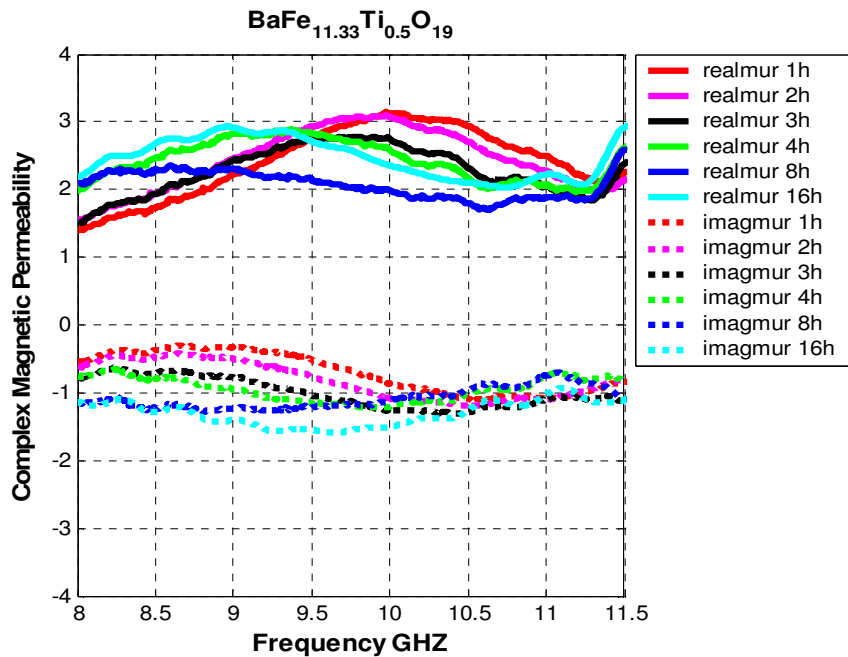
Figure 66 Variation of the real and imaginary parts of the complex permeability with respect to frequency for $BaFe_{11.33}Ti_{0.5}O_{19}$ ceramics within the X-band.
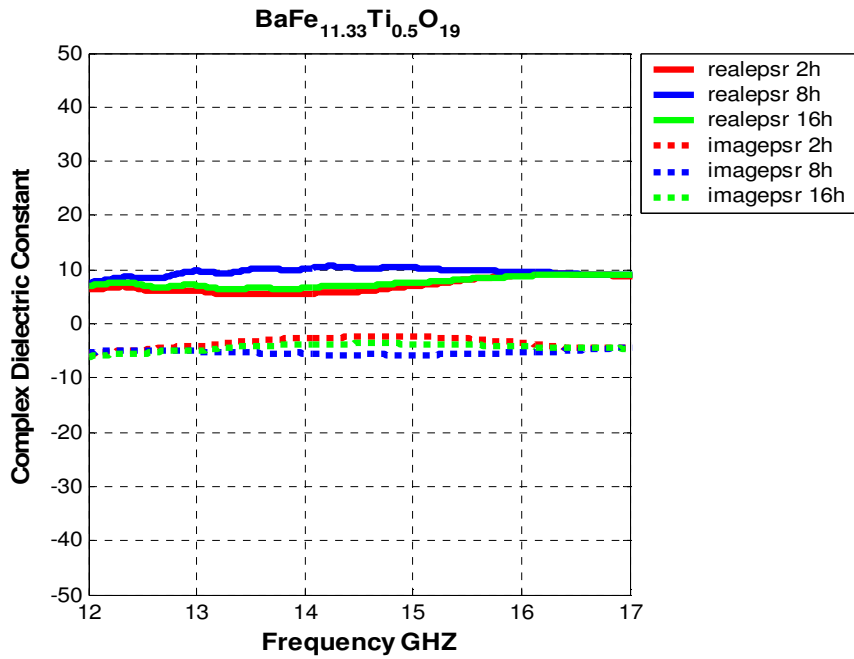
Figure 67 Variation of the real and imaginary parts of the complex permittivity with respect to frequency for $BaFe_{11.33}Ti_{0.5}O_{19}$ ceramics within the Ku-band.
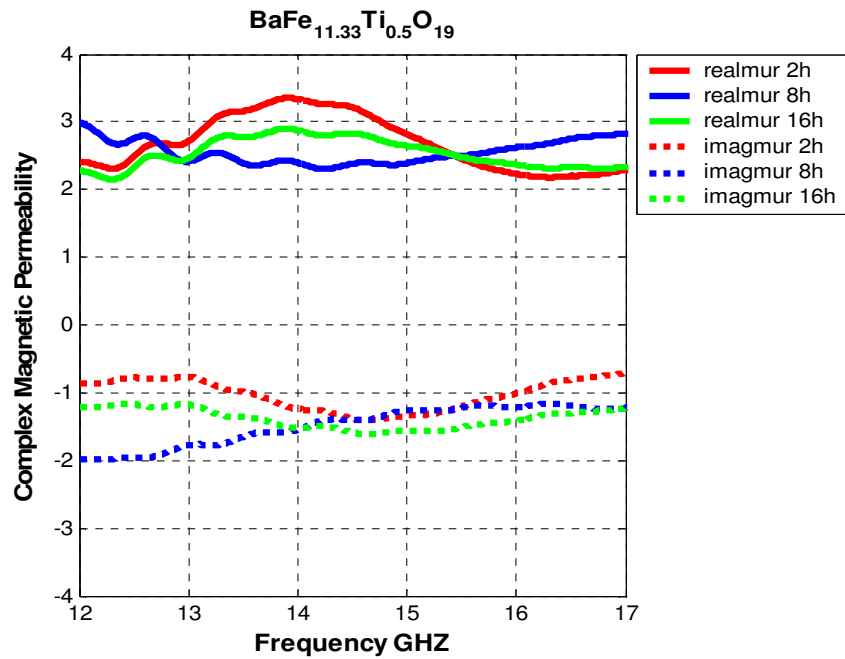
Figure 68 Variation of the real and imaginary parts of the complex permeability with respect to frequency for $BaFe_{11.33}Ti_{0.5}O_{19}$ ceramics within the Ku-band.
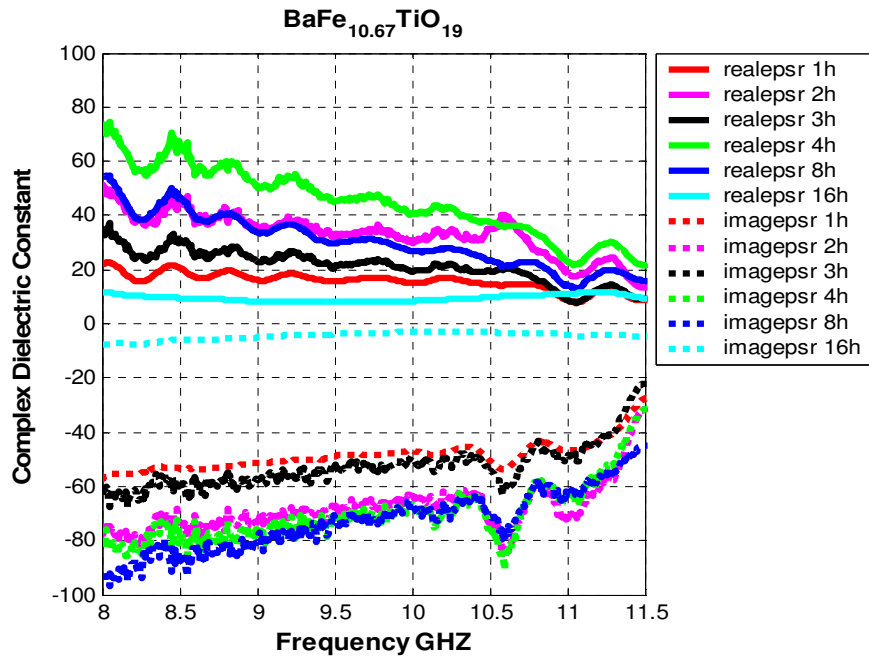
Figure 69 Variation of the real and imaginary parts of the complex permittivity with respect to frequency for BaFe$_{10.67}$TiO$_{19}$ ceramics within the X-band.
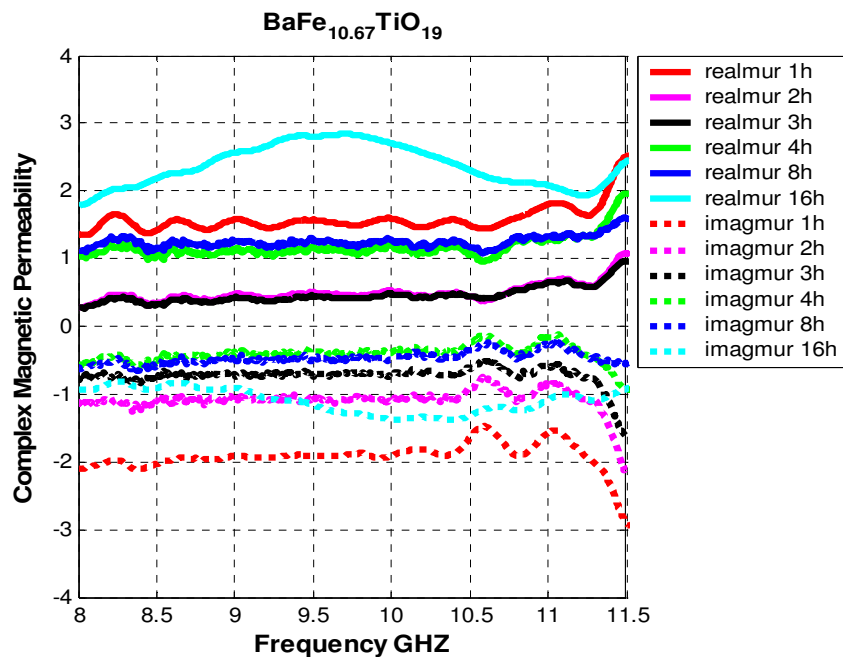
Figure 70 Variation of the real and imaginary parts of the complex permeability with respect to frequency for BaFe$_{10.67}$TiO$_{19}$ ceramics within the X-band.
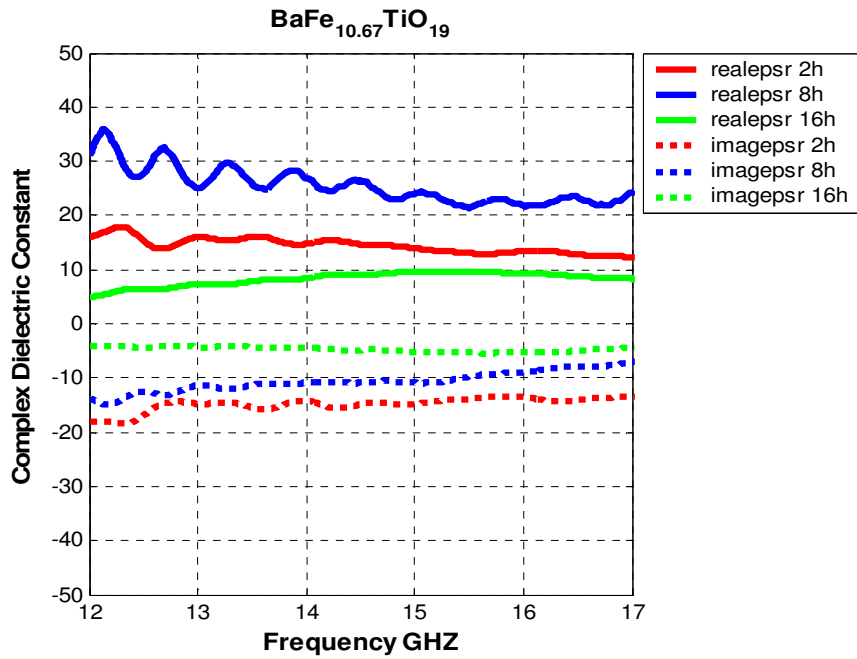
Figure 71 Variation of the real and imaginary parts of the complex permittivity with respect to frequency for BaFe$_{10.67}$TiO$_{19}$ ceramics within the Ku-band.
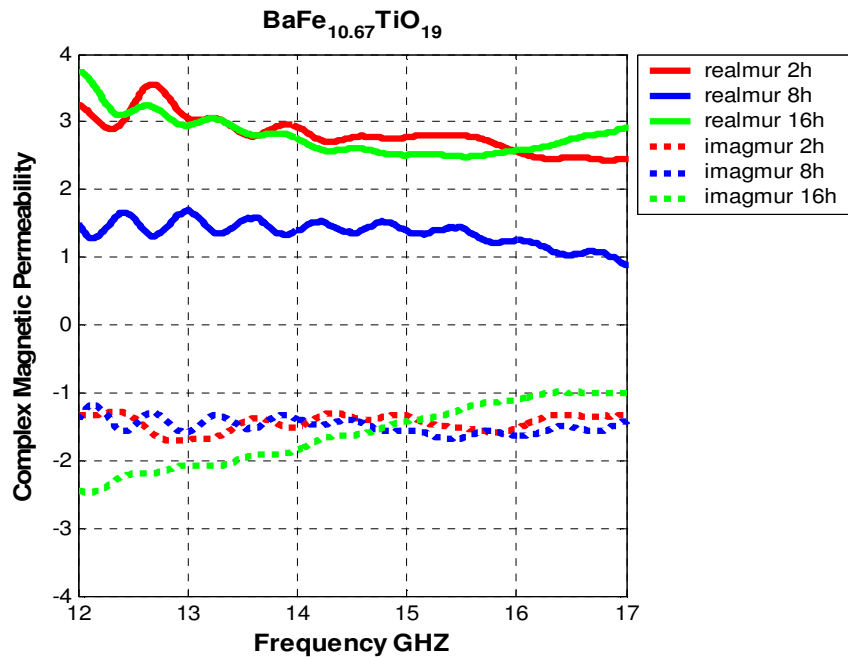
Figure 72 Variation of the real and imaginary parts of the complex permeability with respect to frequency for BaFe$_{10.67}$TiO$_{19}$ ceramics within the Ku-band.
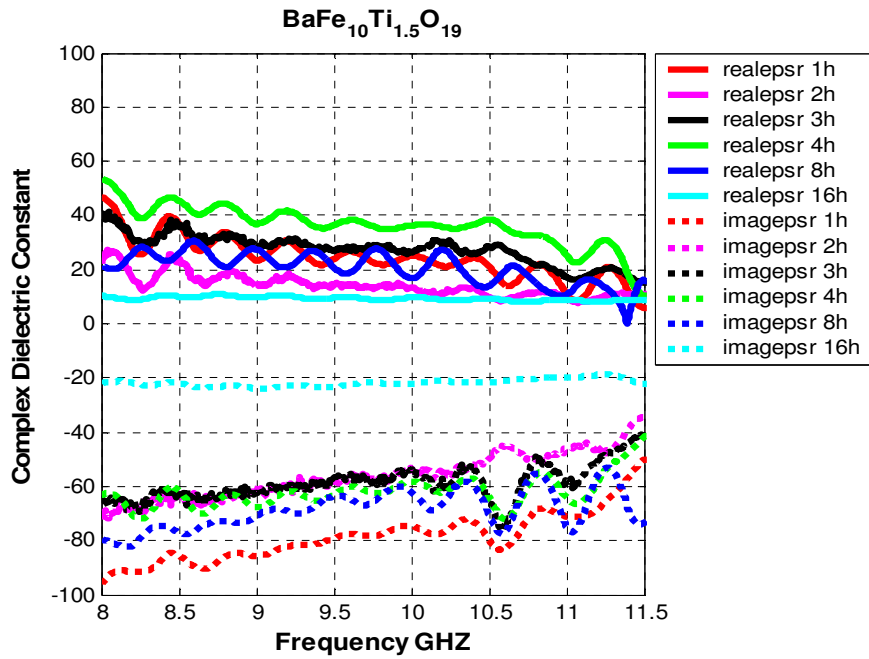
Figure 73 Variation of the real and imaginary parts of the complex permittivity with respect to frequency for $BaFe_{10}Ti_{1.5}O_{19}$ ceramics within the X-band.
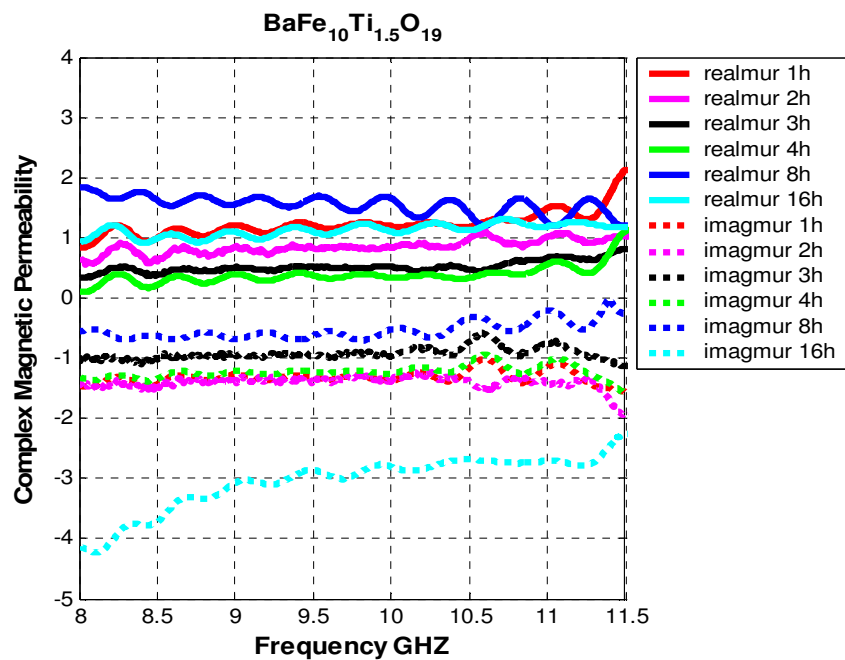
Figure 74 Variation of the real and imaginary parts of the complex permeability with respect to frequency for $BaFe_{10}Ti_{1.5}O_{19}$ ceramics within the X-band.
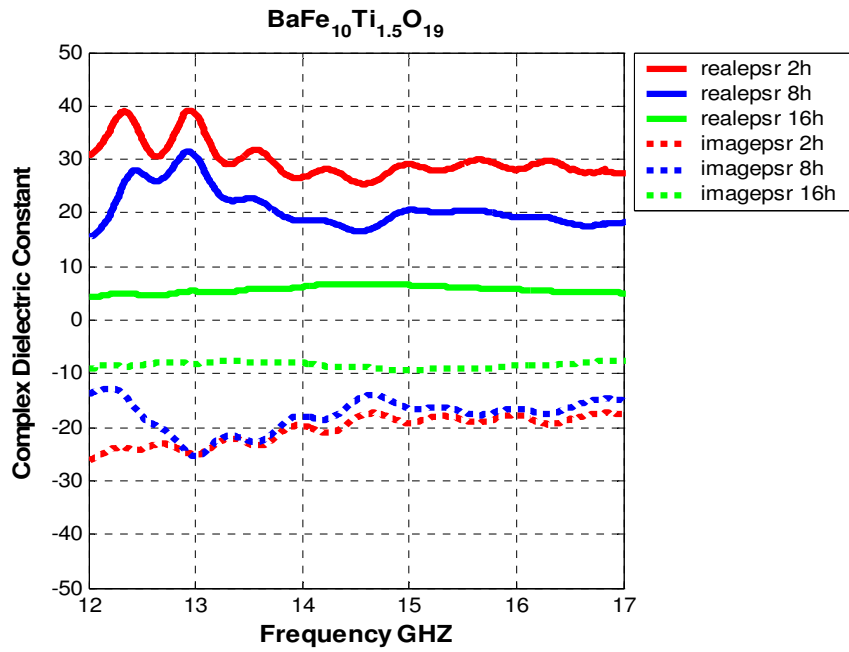
Figure 75 Variation of the real and imaginary parts of the complex permittivity with respect to frequency for $BaFe_{10}Ti_{1.5}O_{19}$ ceramics within the Ku-band.
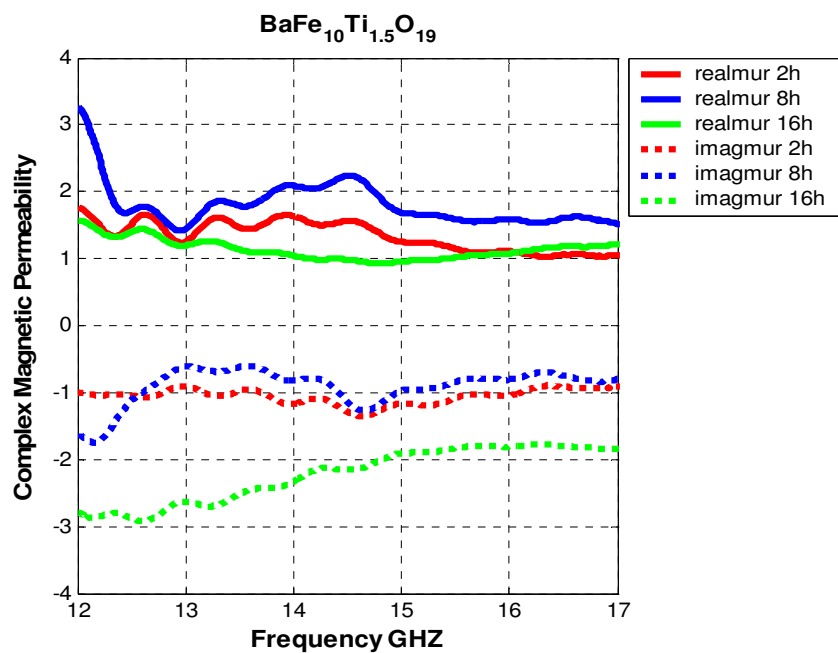

Figure 76 Variation of the real and imaginary parts of the complex permeability with respect to frequency for $BaFe_{10}Ti_{1.5}O_{19}$ ceramics within the Ku-band.
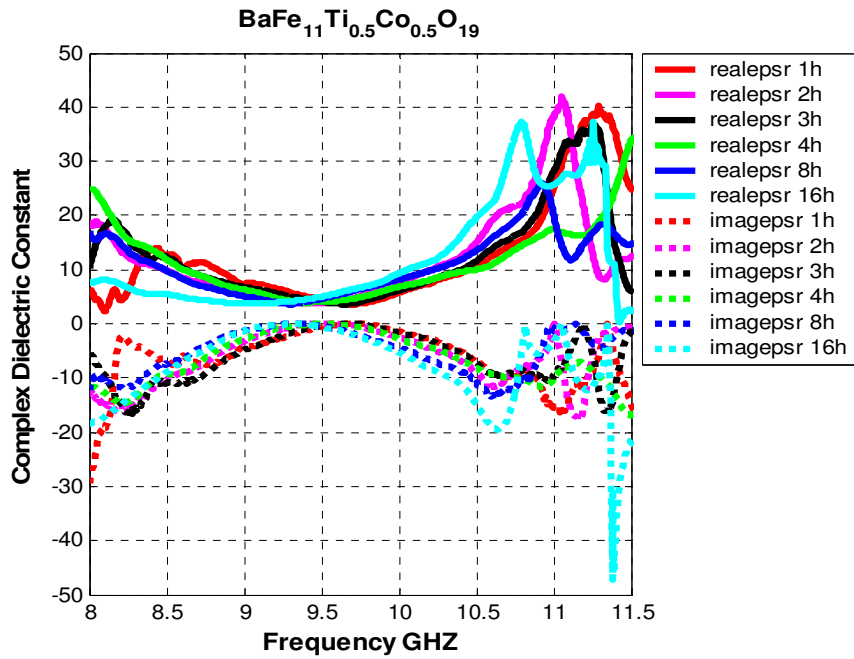
Figure 77 Variation of the real and imaginary parts of the complex permittivity with respect to frequency for $BaFe_{11}Ti_{0.5}Co_{0.5}O_{19}$ ceramics within the X-band.
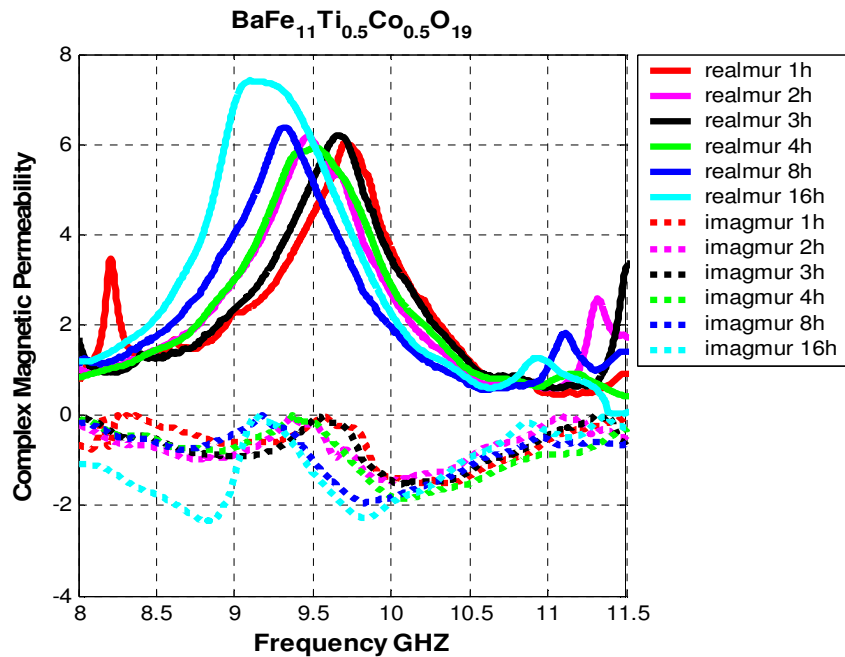
Figure 78 Variation of the real and imaginary parts of the complex permeability with respect to frequency for $BaFe_{11}Ti_{0.5}Co_{0.5}O_{19}$ ceramics within the X-band.
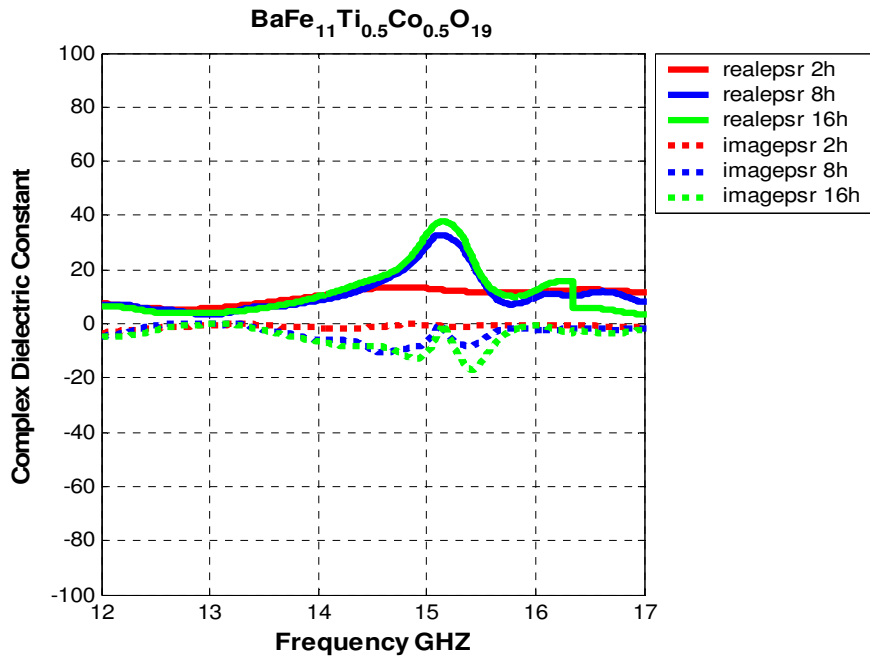
Figure 79 Variation of the real and imaginary parts of the complex permittivity with respect to frequency for $BaFe_{11}Ti_{0.5}Co_{0.5}O_{19}$ ceramics within the Ku-band.
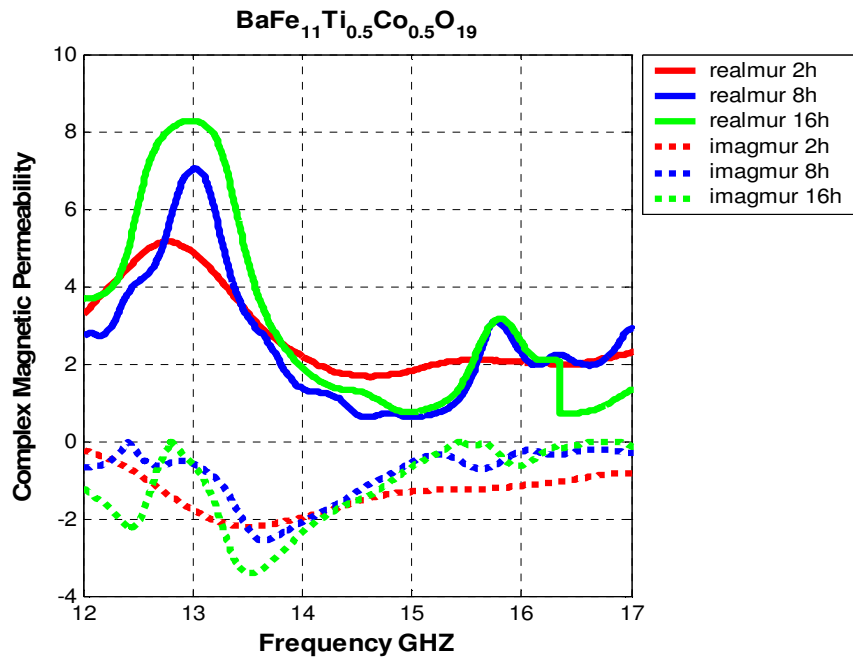
Figure 80 Variation of the real and imaginary parts of the complex permeability with respect to frequency for $BaFe_{11}Ti_{0.5}Co_{0.5}O_{19}$ ceramics within the Ku-band.
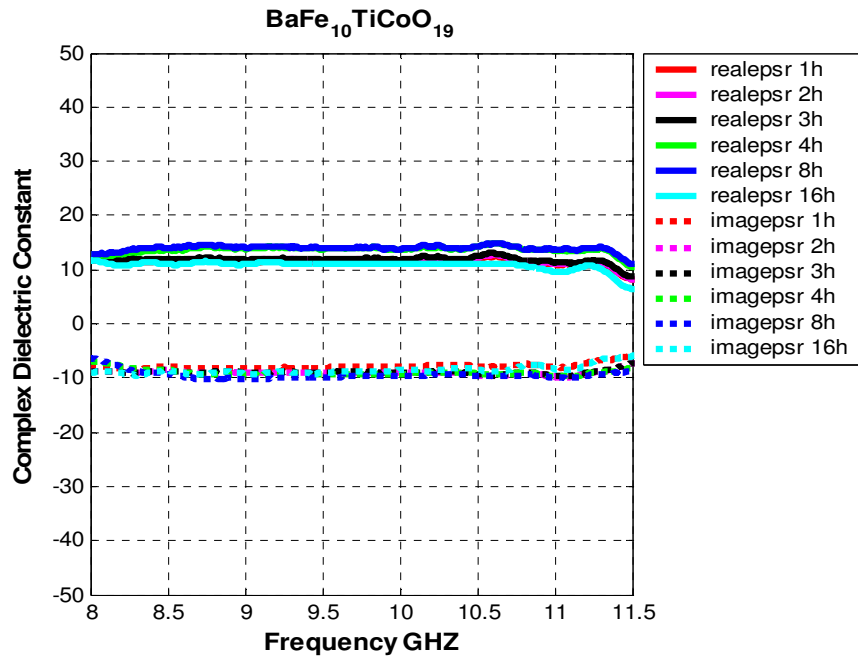
Figure 81 Variation of the real and imaginary parts of the complex permittivity with respect to frequency for $BaFe_{10}TiCoO_{19}$ ceramics within the X-band.
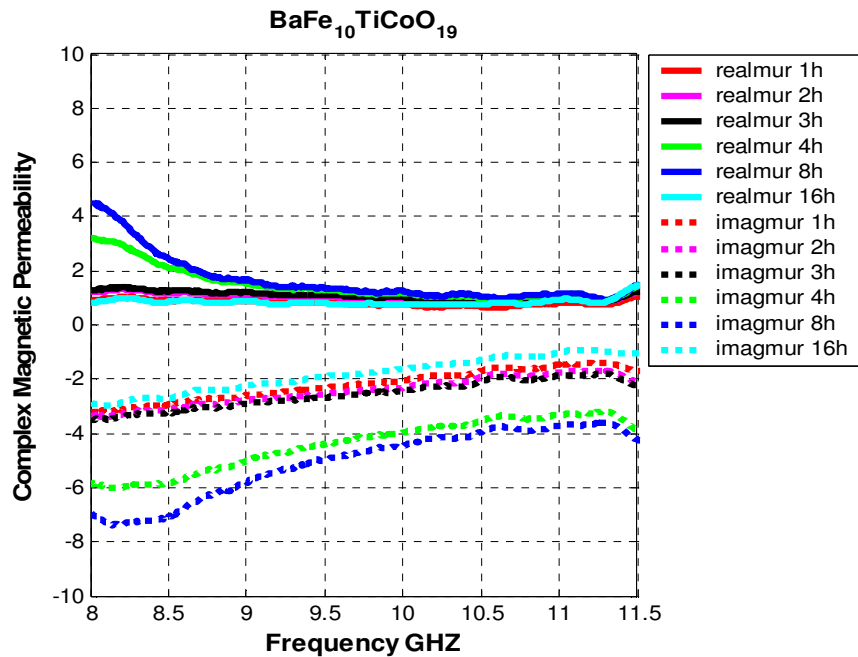
Figure 82 Variation of the real and imaginary parts of the complex permeability with respect to frequency for $BaFe_{10}TiCoO_{19}$ ceramics within the X-band.
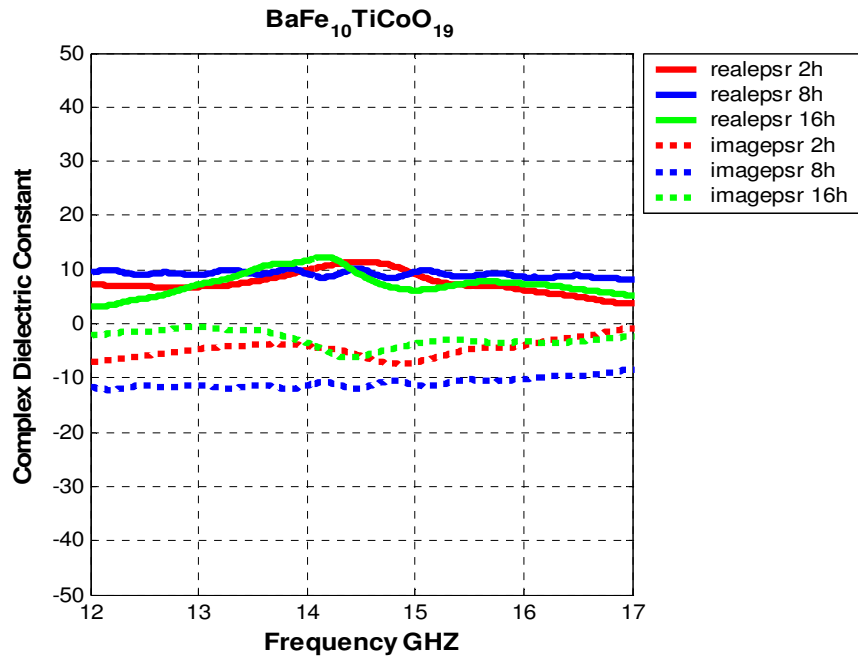
Figure 83 Variation of the real and imaginary parts of the complex permittivity with respect to frequency for $BaFe_{10}TiCoO_{19}$ ceramics within the Ku-band.
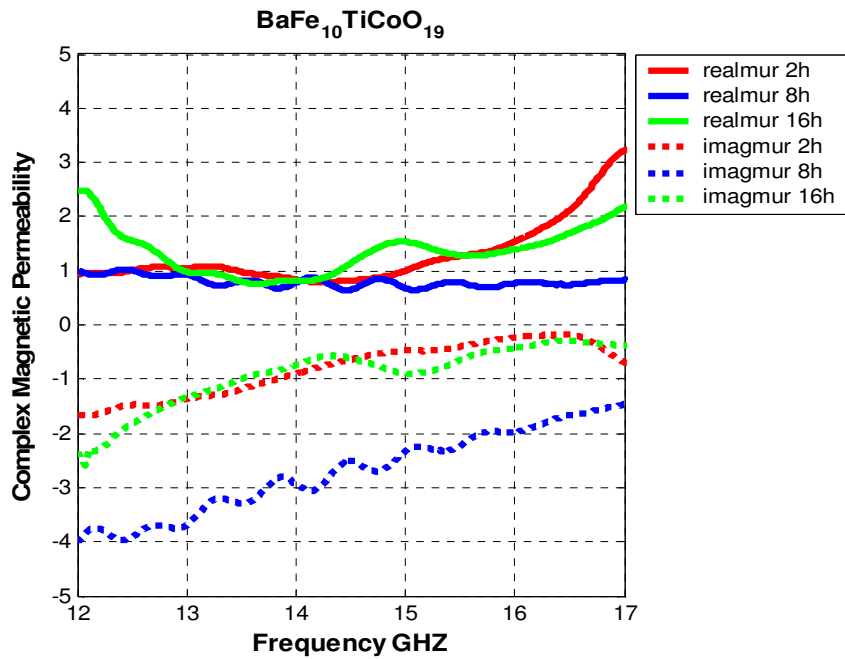

Figure 84 Variation of the real and imaginary parts of the complex permeability with respect to frequency for $BaFe_{10}TiCoO_{19}$ ceramics within the Ku-band.
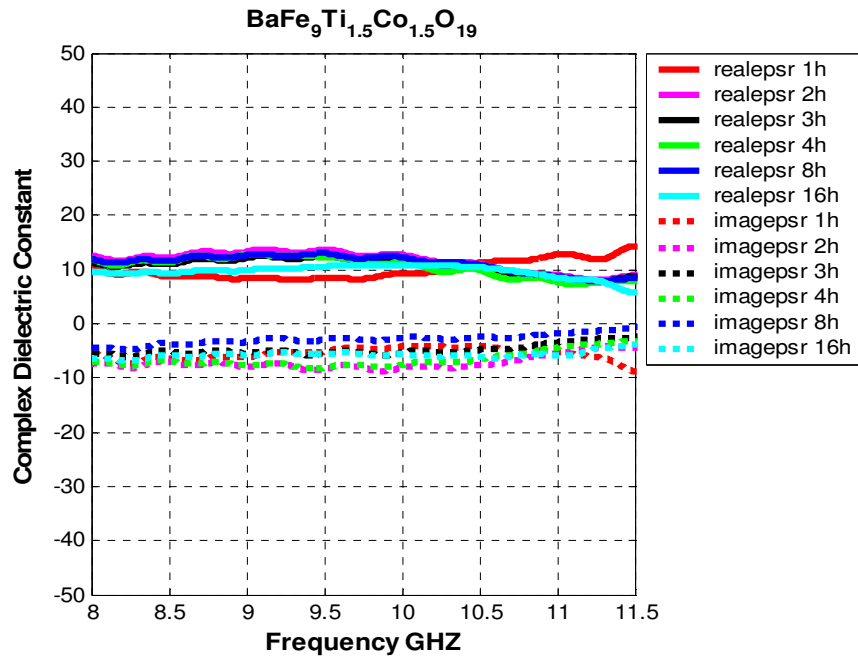
Figure 85 Variation of the real and imaginary parts of the complex permittivity with respect to frequency for BaFe$_9$Ti$_{1.5}$Co$_{1.5}$O$_{19}$ ceramics within the X-band.
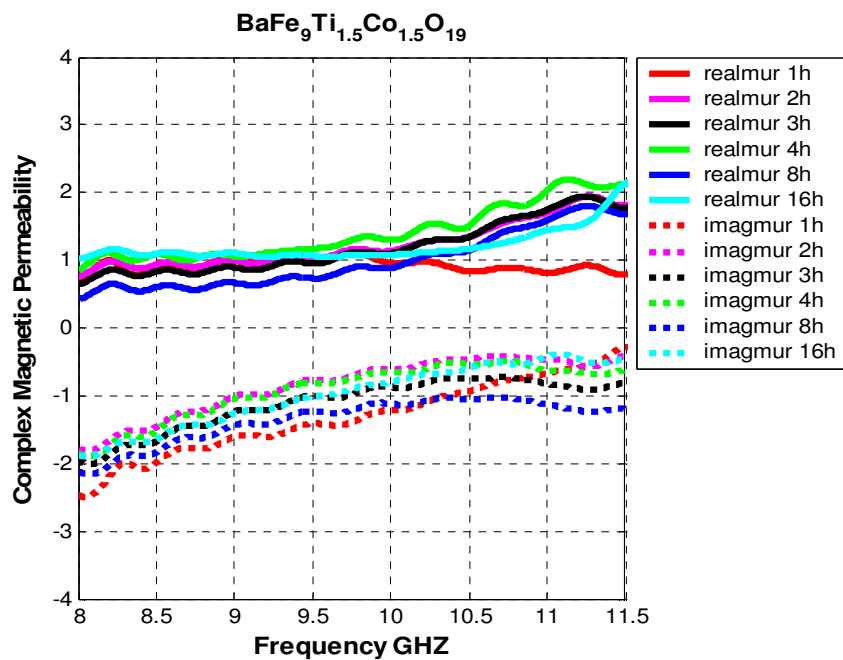
Figure 86 Variation of the real and imaginary parts of the complex permeability with respect to frequency for BaFe$_9$Ti$_{1.5}$Co$_{1.5}$O$_{19}$ ceramics within the X-band.
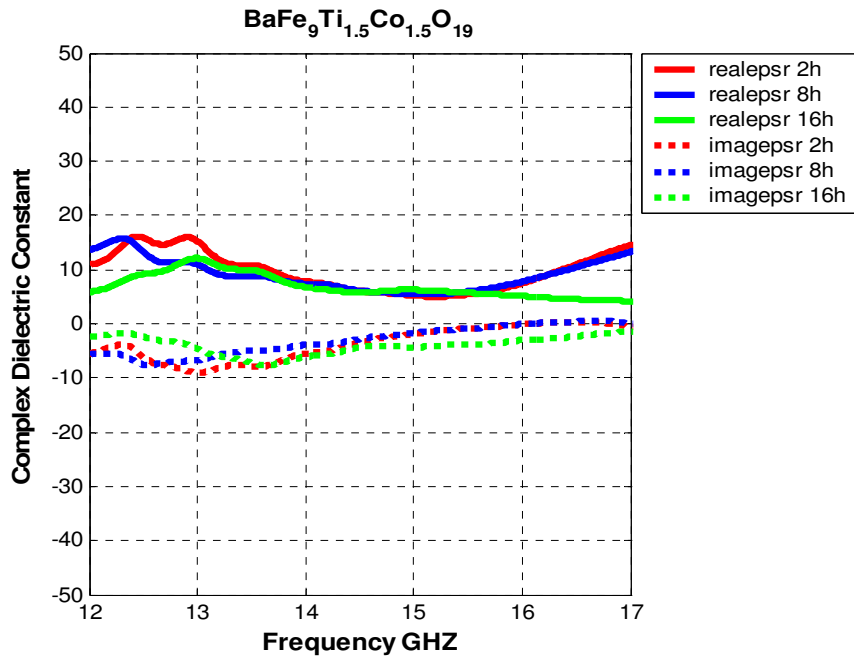
Figure 87 Variation of the real and imaginary parts of the complex permittivity with respect to frequency for BaFe$_9$Ti$_{1.5}$Co$_{1.5}$O$_{19}$ ceramics within the Ku-band.
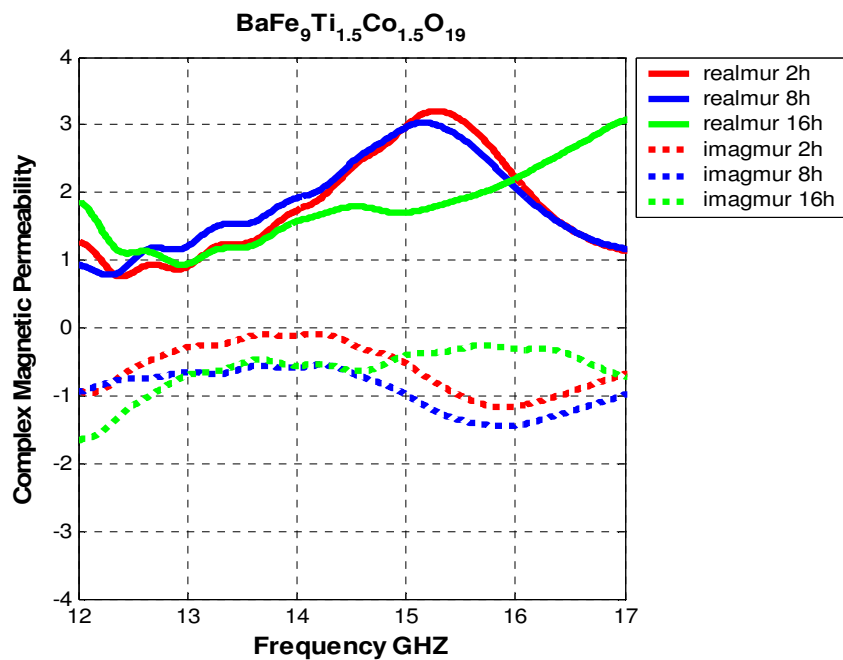

Figure 88 Variation of the real and imaginary parts of the complex permeability with respect to frequency for BaFe$_9$Ti$_{1.5}$Co$_{1.5}$O$_{19}$ ceramics within the Ku-band.

CHAPTER 5

DISCUSSION AND CONCLUSION

Among ceramic ferrites, barium hexaferrites are the commonly used materials for radar absorption purposes. These materials are preferred especially in high frequency applications (in GHz range) due to their high magnetic and dielectric losses at microwave frequencies [12]. Ferromagnetic resonance is the main channel for the BaHF to absorb microwave energy [17]. The resonant frequency of undoped BaHF is around 47.6 GHz. Substitutions of foreign cations at Ba^{2+} or Fe^{3+} sites in the BaHF crystal structure are known to generate resonance at lower frequencies. With proper selection of substituents and careful considerations with respect to dimensions and processing BaHF becomes an effective microwave absorber covering wider frequencies within the radar range.

BaHF has a strong anisotropy along its c axis. Previous studies on substituted BaHF established that incorporating small amounts of Co^{2+} and Ti^{4+} into BaHF changed the magnetic anisotropy from uniaxial to planar which gave rise to increase in its microwave absoption properties [22].

Previous studies on the determination of microwave absorption properties of BaHF were carried out generally on composites in which BaHF particles were disseminated in a thermoset plastic matrix. Volumetrically, the ratio of solids to the plastic has been maintained at around 50 percentage [12, 14]. Therefore, the microwave interactions defined in these studies were those of the composite rather than the BaHF itself. There is a single study caried out by Castelanos et al [37] in which BaHF was brought into the form of a sintered bulk ceramic. That study was confined to the measurement of magnetization of Ti substituted BaHF rather than elucidating its microwave absorption behavior.

The main objective of the present thesis work was to study the interaction of bulk BaHF ceramics with electromagnetic waves. For this purpose tiles of BaHF, in the

form of undoped barium ferrite or ferrites substituted with Ti and/or Co, were manufactured by conventional techniques of ceramic processing. X-ray diffraction patterns of undoped and modified BaHF powders, as well as those of the ceramic tiles, confirmed the formation of the magnetoplumbite structure in all compositions studies. The exception to this was BaHF produced by Co doping. In view of the uncertainities in the identification of foreign XRD peaks, these materials were left outside the scope of the thesis study.

Factors involved in ceramic processing, such as the type and level of doping together with firing conditions played important role on the density and microstructure of the sintered ceramic tiles. SEM studies revealed that in many ferrite ceramics produced with up to 8 hours of soak during sintering a 'duplex' microstructure was promoted. The duplex grain morphology disappeared with extended soak duration (16 hours) especially in the compositions $BaFe_{10.67}TiO_{19}$ and $BaFe_{10}Ti_{1.5}O_{19}$. It is known that the uniformity in the grain size and the average grain diameter can control properties such as magnetic permeability [33].

For the assessment of transmission and reflection parameters of ceramic tiles, a vector network analyzer available in the Electrical and Electronics Engineering Department of METU was used. The interaction of BaHF ceramics with microwaves were characterized within X and Ku bands in terms of reflection, transmission, and absorption. From the large volume of the interaction data a summary on absorption characteristics of the BaHF tiles manufactured under different processing conditions are presented in Figure 89 and Figure 90. On the average, within the frequency band of interest, undoped BaHF ceramic absorbed about 45 percentage of the incident EM wave. The absorption started from a low 30 percent at 8 GHz, rose to a high of 50 percent in the range 9.5 to 10.5 GHz and then leveled off in the remaining part of the frequency spectrum.
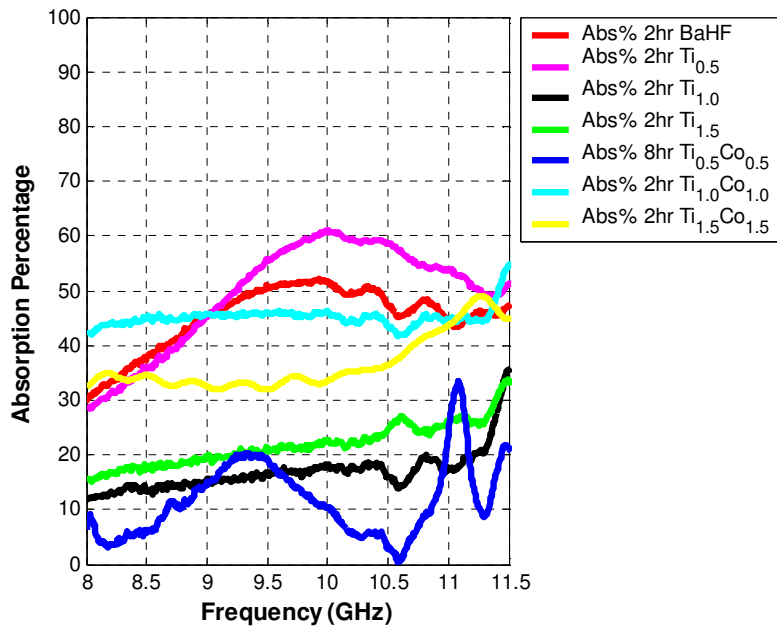
Figure 89 Microwave absorption percentage of various ferrites within the X-band.
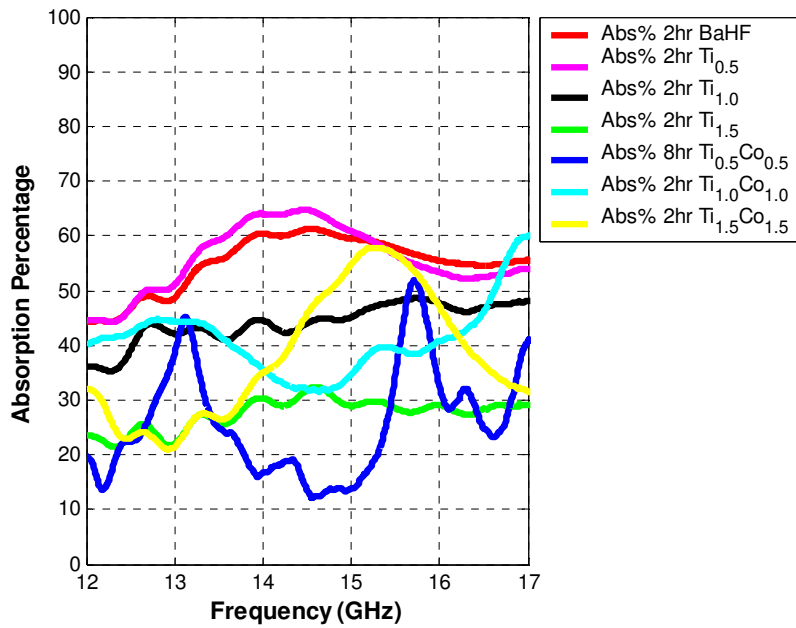
Figure 90 Microwave absorption percentage of various ferrites within the Ku-band.

Ceramics doped with 0.5 mole Ti exhibited improved absorption properties. The absorption was above 50 percent and remained substantially uniform throughout the frequency range 9.5 GHz to 17 GHz. Ghasemi et al. [12, 14] reported that microwave absorption of polycrystalline ferrite depends on the composition of ferrite, post sintering density, grain size and porosity. Accordingly, the higher proportion of porosity obtained for all soak durations may be responsible for higher absorption.

The ceramic manufactured by the dual additions of Ti and Co each at 0.5 mole level exhibited an interesting absorption pattern; the curve corresponding to this ceramic had peaks at certain frequencies indicating greater absorption as compared to the other parts of the spectrum. This fact may reveal that, the natural resonant frequency of BaHF was successfully reduced to X and Ku band ranges. Moreover, the permeability curves of these ceramics support the resonant frequency phenomenon by showing a maxima within the X and Ku bands.

Ghasemi and co-workers [12, 14] performed reflection loss measurements on so-called rubber ferrites manufactured from BaHF powders and PVC. Their samples had 2 mm thickness and were backed by aluminum metal plates. The EM interaction measurements on these composites within the frequency band 12 GHz to 20 GHz revealed that about 40 percent of the EM wave was absorbed. Similar measurements on a composite manufactured by using $BaFe_9Ti_{1.5}Co_{1.5}O_{19}$ powders revealed very little change in absorbance. The bulk ceramics produced in the present study had slightly better microwave absorbance (maximum 55 %) capability than the composites mentioned above.

The graphical data presented on complex dielectric permittivity ε and complex magnetic permeability μ were used to summarize the information related to the real and imaginary parts of these variables in Table 10. For sake of brevity, the table does not cover the entirety of the ceramics studied, but weight is given to those prepared by the 2 hours soak during sintering.

Table 10 Variation of microwave absorption parameters with frequency.

	f (GHz)	ε'	$|\varepsilon''|$	μ'	$|\mu''|$	tanδ	α (Nepers/m)
BaHF 2h	9.0	10.0	5.0	2.5	1.0	1.50	534
	10.0	12.0	5.0	2.5	1.0	1.40	620
	14.0	7.5	3.0	3.0	1.5	1.50	789
0.5 Ti 2h	9.0	11.0	5.0	2.5	1.0	1.18	467
	10.0	10.0	4.0	2.7	1.0	1.35	585
	14.0	10.0	4.0	2.8	1.5	1.55	893
	17.0	9.0	5.0	2.5	1.0	1.29	837
1.0 Ti 2h	9.0	35.0	72.0	0.4	1.0	1.54	1312
	10.0	32.0	64.0	0.5	1.0	1.67	1409
	14.0	15.0	15.0	2.8	1.5	3.31	1435
	17.0	12.0	13.0	2.4	1.3	3.84	1496
1.0 Ti 16h	10.0	10.0	3.0	2.7	1.3	1.33	582
	17.0	8.0	4.0	3.0	1.0	1.40	955
1.5 Ti 2h	9.0	15.0	63.0	0.7	1.4	1.27	922
	11.0	10.0	46.0	1.0	1.4	1.37	906
	14.0	26.0	20.0	1.6	1.2	3.73	1470
	17.0	27.0	18.0	1.0	1.0	5.00	1528
0.5Ti 0.5Co 2h	8.0	8.0	20.0	1.0	0.8	3.00	492
	9.5	5.0	0.0	6.0	0.2	1.00	495
	13.0	5.0	1.0	5.0	1.8	1.16	673
	17.0	12.0	0.0	2.3	0.8	1.00	873

Table 10 (cont'd)

	f (GHz)	ε'	$|\varepsilon''|$	μ'	$|\mu''|$	tanδ	α (Nepers/m)
1.0Ti 1.0Co 2h	9.0	12.0	8.0	1.2	2.7	5.00	723
	11.0	10.0	7.0	0.7	1.6	4.33	619
	14.0	10.0	4.5	0.8	1.0	3.57	638
	17.0	4.0	2.0	3.2	1.3	1.51	723
1.5Ti 1.5Co 2h	9.0	8.0	8.0	1.0	1.6	4.33	542
	11.0	12.0	6.0	0.8	0.6	2.20	475
	14.0	7.5	6.5	1.7	0.2	1.23	535
	17.0	13.0	0.0	1.2	0.7	1.00	640
	15.3	5.5	1.5	3.2	1.0	1.19	675

In the above table, the features which probably deserve more attention are as follows:

(1) The dielectric permittivities of all types of BaHF ceramics in the table are too high. As already mentioned, for good absorbance the magnitudes of the dielectric permittivity and magnetic permeability should be close, and that of the loss tangent should be high. The rather low absorbance may be attributed to the large differences between permeability and permittivity. One remedy to obtain matching conditions between these two terms may be the use of plastic composites.

(2) In the last column of the table microwave attenuation parameter "α" of the ceramics are listed. These are calculated with the help the Equation (1.6) given earlier on Page 5.

The BaHF ceramics display higher attenuation when they contain Ti as substituting species. Also, the extent of attenuation differs with frequency. This feature might be used as a tool in the design of layered composites.

Close correlations exist between the attenuation characteristics of BaHF ceramics and their magnetization behavior. The hysteresis curves of the ferrites obtained in the present study are shown in Figure 91. In the ferrites with Ti substitution the

coercivity is seen to be lowered greatly as compared to that of the undoped BaHF. Hence the Ti substitution causes substantial lowering in the magnetocrsytalline anisotropy energy. This was reflected in the grain morphology depicted by the SEM photographs in Figure 27 and Figure 28. Changes in the hysteresis behavior and in the attenuation characteristics indicate that the single titanium substitution at 1 mole level should be good in attaining adequate microwave absorbance.

Consequently, following conclusions have been drawn:

- Co and/or Ti substituted bulk BaHF ceramics were prepared by conventional ceramic manufacturing techniques.

- The substitution of Ti and Co for Fe site in the crystal structure permitted to manufacture highly densified ceramics with the exception of 0.5 mole Ti doped BaHF.

- The reflectance, transmittance and microwave absorption characteristics of the ferrite ceramics in bulk form were determined through the use of waveguide method. The studies revealed that, undoped BaHF and low Ti (0.5 mole) doped ceramics showed good absorption percentage amounting to 50 in average within X and Ku bands.

- Ti additions were quite effective in the attenuation of the microwave. Bulk BaHF ceramics containing 1.0 and 1.5 mole Ti exhibited higher attenuation.

- An additional and important outcome of Ti and/or Co substitution was the large reduction in the coercivity value and hence reduction in the magnetocrytalline anisotropy energy of BaHF.

- The poor microwave absorption characteristics of some ceramics were probably due to the lack of match between the air and ceramic.
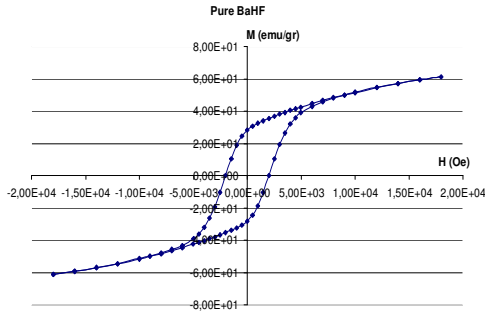
(a) BaFe$_{12}$O$_{19}$
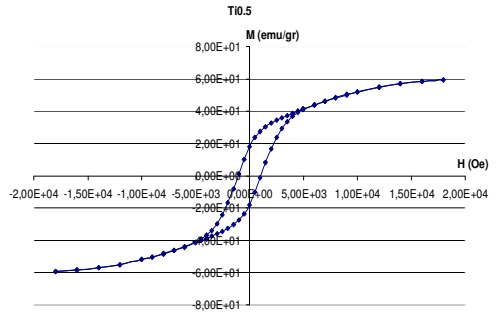
(b) Ti = 0.5
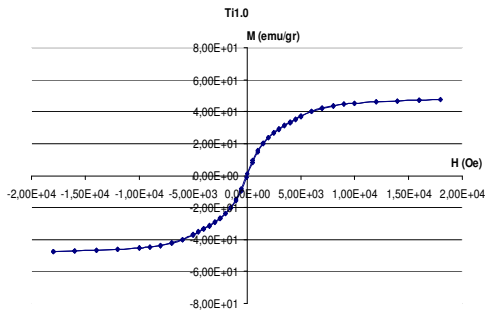
(c) Ti = 1.0
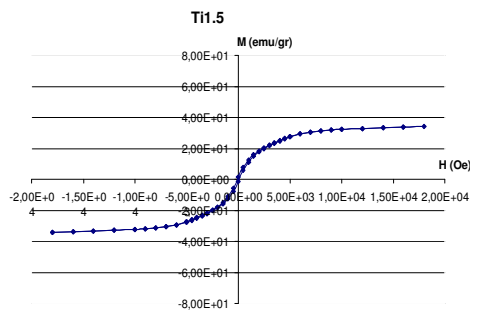
(d) Ti = 1.5
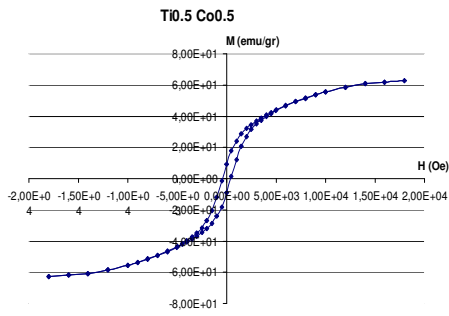
(e) Ti = 0.5 & Co = 0.5
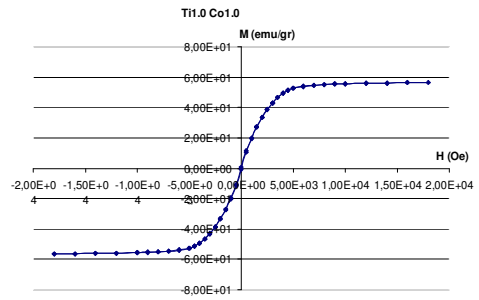
(f) Ti = 1.0 & Co = 1.0

Figure 91 Hysteresis curves of BaHF ceramics.

There are three suggestions for future work on the subject of this thesis study. The first one is the production of textured BaHF ceramics which was kept outside the scope of the present thesis study. Such ceramics may exhibit quite different modes of EM interaction. Secondly, plastic composites made by platelet BaHF particles containing Ti deserves attention. Thirdly, ternary substitutions may yield larger absorption characteristic.

REFERENCES

1. Cheng, D. K., *"Fundamentals of Engineering Electromagnetics".* Addison-Wesley Publishing Company, Inc., 1993.

2. Seo, I. S., Chin, W. S., Lee, D. G., *"Characterization of Electromagnetic Properties of Polymeric Composite Materials with Free Space Method".* Composite Structures, June 2004. **66**: p. 533-542.

3. Chin, W. S., Lee, D. G., *"Development of the Composite RAS (Radar Absorbing Structure) for the X-band Frequency Range".* Composite Structures, September 2005. **77**: p. 457-465.

4. Rezende, M. C., et al. *"Radar Cross Section Measurements (8-12 GHz) of Flat Plates Painted with Microwave Absorbing Materials".* in *Microwave and Optoelectronics Conference, 2001. IMOC 2001.Proceedings of the 2001 SBMO/IEEE MTT-S International.* 2001.

5. Bennett, J. C., Chambers, B., Crossley, G. E., *"Characterization of Microwave Four-Parameter Materials and Its Application in Wideband Radar Absorber Design".* IEE Proc.-Radar, Sonar Navig.,, 1994. **141**(6).

6. Amin, M. B., James, J. R., *"Techniques for Utilization of Hexagonal Ferrites in Radar Absorbers Part I".* The Radio and Electronic Engineer, 1981. **51**(5): p. 209-218.

7. Amin, M. B., James, J. R., *"Techniques for Utilization of Hexagonal Ferrites in Radar Absorbers Part II".* The Radio and Electronic Engineer, 1981. **51**(5): p. 219-225.

8.   Pitman, K. C., Lindley, M. W., Simkin, D., Cooper, J. F., *"Radar Absorbers: Better by Design".* IEE Proceedings-F, 1991. **138**(3): p. 223-228.

9.   Weir, W. B., "*Automatic Measurement of Complex Dielectric Constant and Permeability at Microwave Frequencies".* Proceedings of the IEEE, 1974. **62**(1): p. 33-36.

10.   Knott, E. F., *"The Thickness Criterian for Single-Layer Radar Absorbents".* IEEE Transactions on Antennas and Propagation, 1979. **AP-27**(5): p. 698-701.

11.   Cao, M., Qin, R., Qiu, C., Zhu, J., *"Matching Design and Mismatching Analysis towards Radar Absorbing Coatings Based on Conducting Plate".* Materials and Design, 2003. **24**: p. 391-396.

12.   Ghasemi, A., et al., "*Electromagnetic Properties and Microwave Absorbing Characteristics of Doped Barium Hexaferrite".* Journal of Magnetism and Magnetic Materials, 2006. **302**(2): p. 429-435.

13.   Qiu, J., Gu, M. and Shen, H. "*Microwave Absorption Properties of Al- and Cr-Substituted M-type Barium Hexaferrite".* Journal of Magnetism and Magnetic Materials, 2005. **295**(3): p. 263-268.

14.   Ghasemi, A., Saatchi, A., Salehi, M., Hossienpour, A., Morisako, A., Liu, X., *"Influence of Matching Thickness on the Absorption Properties of Doped Barium Ferrites at Microwave Frequencies".* physica status solidi (a), 2006. **203**(2): p. 358-365.

15.   Kawai, Y., et al., "*Ultrasonic Attenuation in a $BaTiFe_{11}O_{19}$ Single Crystal".* Journal of Magnetism and Magnetic Materials, 1999. **196-197**: p. 309-311.

16.   Qiu, J., Wang, Y. and Gu, M. "*Effect of Cr Substitution on Microwave Absorption of BaFe$_{12}$O$_{19}$"*. Materials Letters, 2006. **60**(21-22): p. 2728-2732.

17.   Qiu, J. X., et al., "*Effect of Aluminum Substitution on Microwave Absorption Properties of Barium Hexaferrite"*. Journal of Applied Physics, 2005. **98**(10).

18.   Wartewig, P., et al., "*Magnetic Properties of Zn- and Ti-substituted Barium Hexaferrite"*. Journal of Magnetism and Magnetic Materials, 1999. **192**(1): p. 83-99.

19.   Meshram, M. R., et al. "*Characterization of (Co-Mn-Ti) Substituted M type Barium Hexagonal Ferrite Based Microwave Absorber at X band"*. in *Antennas, Propagation and EM Theory, 2003. Proceedings. 2003 6th International Symposium on*. 2003.

20.   Meshram, M. R., et al. "*Development and Characterization of (Ba-Mn-Ti) Based Hexagonal Ferrite for Microwave Absorbing Paint"*. in *Antennas and Propagation Society International Symposium, 2002. IEEE*. 2002.

21.   Kreisel, J., et al., "*An Investigation of the Magnetic Anisotropy Change in BaFe$_{12-2x}$Ti$_x$Co$_x$O$_{19}$ single crystals"*. Journal of Magnetism and Magnetic Materials, 2001. **224**(1): p. 17-29.

22.   Wang, C., et al., *"Microstructures and High-frequency Magnetic Properties of Low-temperature Sintered Co-Ti Substituted Barium Ferrites"*. Journal of Magnetism and Magnetic Materials, 2003. **257**(1): p. 100-106.

23.   Kreisel, J., et al., "*The Magnetic Anisotropy Change of BaFe$_{12-2x}$Ir$_x$Co$_x$O$_{19}$: a Single-crystal Neutron Diffraction Study of the Accompanying Atomic and Magnetic Structures"*. Journal of Magnetism and Magnetic Materials, 2000. **213**(3): p. 262-270.

24. Lima, R. D. C., Pinho, M. S., Gregori, M. L., Nunes, R. C. R., Ogasawara, T., *"Effect of Double Substituted M-barium Hexaferrites on Microwave Absorption Properties".* Materials Science, 2004. **22**(3): p. 245-252.

25. Sugimoto, S., et al., *"M-type Ferrite Composite as a Microwave Absorber with Wide Bandwidth in the GHz Range".* Magnetics, IEEE Transactions on, 1999. **35**(5): p. 3154-3156.

26. Meshram, M. R., Bharoti Sinha, N.K.A., Misra, P. S., "*Empirical Relationship between (delta) and Ferromagnetic Resonance Frequency in Hexagonal Ferrite-based Microwave Absorbing Paint".* Microwave and Optical Technology Letters, 2003. **36**(5): p. 352-355.

27. Pinho, M. S., et al., "*Performance of Radar Absorbing Materials by Waveguide Measurements for X- and Ku-band Frequencies".* European Polymer Journal, 2002. **38**(11): p. 2321-2327.

28. Moulson, A. J., Herbert, J. M., *"Electroceramics: Materials, Properties, Applications", Second Edition, John Wiley & Sons Ltd.* 2003.

29. Hench, L. L., West, J. K., *"Principles of Electronic Ceramics".* John Wiley & Sons, 1990.

30. Callister, W. D., Jr., *"Materials Science and Engineering an Introduction", Sixth Edition.* John Wiley & Sons, Inc., 2003.

31. Neelekanta, P. S., *"Handbook of Electromagnetic Materials: Monolithic and Composite Versions and Their Applications".* CRC Press, Boca Raton, New York Washington, DC, 1995.

32. Kingery, W. D., Bowen, H. K., Uhlmann, D. R., *"Introduction to Ceramics", Second Edition.* John Wiley & Sons, Newyork, 1976.

33. Valenzuela, R., *"Magnetic Ceramics".* Cambridge University Press, 1994.

34. Louh, R., Reynolds III, T. G., Buchanan, R. C., *"Ferrite Ceramics" in 'Ceramic Materials for Electronics' edited by Buchanan, R. C., Third Edition.* Marcel Dekker Inc., Newyork, 2004.

35. Smit, J., Wijn, H. P. J., *"Ferrites: Physical Properties of Ferrimagnetic Oxides in Relation to Their Technical Applications", First Edition.* Philips' Technical Library, Eindhoven, 1959.

36. Braun, P. B., *"The Crystal Structure of a new Group of Ferromagnetic Compounds".* Philips Res. Rep., 1957. **12**: p. 491-548.

37. Marino-Castellanos, P. A., et al., "*Magnetic and Microstructural Properties of the Ti^{4+}-doped Barium Hexaferrite".* Journal of Magnetism and Magnetic Materials, 2004. **280**(2-3): p. 214-220.

38. Goldman, A., *"Magnetic Ceramics" in 'Electronic Ceramics Properties, Devices, and Applications' edited by Levinson, L. M.* Marcel Dekker Inc., Newyork and Basel, 1988.

39. Knott, E. F., Shaeffer, J. F., Tuley, M. T., *"Radar Cross Section", Second Edition.* Artech House, Inc., 1993.

40. *"IEEE Dictionary of Electrical and Electronics", Third Edition.* John Wiley & Sons, 1984.

41. Biscaro, R. S., et al. "*Performance Evaluation of Conducting Polymer Paints as Radar Absorbing Materials (RAM)".* in *Microwave and Optoelectronics Conference, 2003. IMOC 2003. Proceedings of the 2003 SBMO/IEEE MTT-S International.* 2003.

101

42.   Perini, J., Cohen, L. S., *"Design of Broad-Band Radar-Absorbing Materials for Large Angles of Incidence"*. IEEE Transactions on Electromagnetic Compatibility, 1993. **35**(2): p. 223-231.

43.   Baginski, M. E., Faircloth, D. L., and Deshpande, M. D., "*Comparison of two Optimization Techniques for the Estimation of Complex Permittivities of Multilayered Structures Using Waveguide Measurements"*. Microwave Theory and Techniques, IEEE Transactions on, 2005. **53**(10): p. 3251-3259.

44.   Ghodgaonkar, D. K., Varadan, V. V., and Varadan, V .K., "*A Free-space Method for Measurement of Dielectric Constants and Loss Tangents at Microwave Frequencies"*. Instrumentation and Measurement, IEEE Transactions on, 1989. **38**(3): p. 789-793.

45.   Babu, V., and Padaikathan, P., "*Structure and Hard Magnetic Properties of Barium Hexaferrite with and without La_2O_3 Prepared by Ball Milling"*. Journal of Magnetism and Magnetic Materials, 2002. **241**(1): p. 85-88.

46.   İyiel, A., *"Synthesis and Characterization of Barium Ferrite Powders as Radar Absorbing Material"*. Thesis Submitted to the Graduate School of Natural and Applied Sciences, Middle East Technical University, 1997.

47.   Cullity, B. D., Stock, S. R:, *"Elements of X-ray diffraction"*. 2001: Prentice Hall.

48.   *"Agilent Network Analysis Applying the 8510 TRL Calibration for Non-Coaxial Measurements"*. Agilent Technologies, USA, 2000.

49.   Nedkov, I., Petkov, A., *"Microwave Absorption in Sc- and CoTİ-Substituted Ba Hexaferrite Powders"*. IEEE Transactions on Magnetics, 1990. **26**(5): p. 1483-1484.

50.   Yongbao, F., Tai, Q., Chunying, S., Xiaoyun, L., *"Complex Permeability and Permittivity and Microwave Absorption Property of Barium Ferrite/ EPDM Rubber Radar Absorbing Materials in 2-18 GHz".* IEEE APMC2005 Proceedings, 2005.